Development of a finite element marine model

Sébastien Blaise

Novembre 2009

Thèse présentée en vue de l'obtention du grade
de docteur en sciences de l'ingénieur

École polytechnique de Louvain

Université catholique de Louvain

UNIVERSITÉ CATHOLIQUE DE LOUVAIN
FACULTÉ DES SCIENCES APPLIQUÉES
UNITÉ DE MÉCANIQUE APPLIQUÉE

DEVELOPMENT OF A FINITE ELEMENT MARINE MODEL

THÈSE PRÉSENTÉE PAR

SÉBASTIEN BLAISE

EN VUE DE L'OBTENTION DU GRADE DE
DOCTEUR EN SCIENCES DE L'INGÉNIEUR

THESIS COMMITTEE:

Pr Jean-Marie Beckers, Université de Liège
Pr Vincent Legat, Université catholique de Louvain
Pr Hans Burchard, Leibniz Institute for Baltic Sea Research
Pr Eric Deleersnijder, Université catholique de Louvain (Promoteur)
Pr Grégoire Winckelmans, Université catholique de Louvain (Président)
Pr Jean-François Remacle, Université catholique de Louvain (Promoteur)
Dr Sergey Danilov, Alfred Wegener Institute for Polar and Marine Research

Louvain-la-Neuve, Novembre 2009

Je remercie vivement mes promoteurs, les Professeurs Eric Deleersnijder, Jean-François Remacle et Vincent Legat. Chacun à leur manière, ils ont contribué à ce que chaque moment de ces quatre années de thèse se passe dans les meilleures conditions, le subtil mélange de trois promoteurs impliquant une grande richesse sur les plans humain et scientifique. Bien qu'il ne soit pas officiellement promoteur, Vincent en a plus qu'assuré la charge par une disponibilité et un appui constants, tant lors de banquets festifs que dans les moments les plus difficiles. Durant ma thèse, Eric n'a cessé de me proposer de nouveaux problèmes à étudier et m'a prodigué de nombreux conseils. Jean-François m'a orienté sur la voie du doctorat avec un enthousiasme perpétuel et m'a apporté une grande ouverture sur l'extérieur, notamment en m'encourageant à participer aux conférences et cours doctoraux, ou en m'introduisant auprès de mon futur labo de recherche. Pour une review plus complète, mais non exhaustive, des qualités respectives de ces trois professeurs, le lecteur s'en remettra à Hanert (2004); Legrand (2006); Marchandise (2006); White (2007) et Bernard (2008).

Je remercie également les autres membres du jury, les professeurs Hans Burchard, Jean-Marie Beckers, Sergey Danilov et Grégoire Winckelmans, pour leurs commentaires et remarques judicieuses.

Je tiens à remercier mes collègues GC et mema pour tous les bons moments passés ensemble, mais également pour les collaborations fructueuses que nous avons développées. Je remercie tout particulièrement Richard et Jonathan avec qui j'ai travaillé de nombreuses heures, et dont une partie de cette thèse leur revient tant leur contribution fut importante.

Je remercie du fond du cœur les quelques amis Néo-Louvanistes, Gaumais ou Liégeois dont le potentiel récréatif, pour ne pas dire festif, fût au-delà de mes espérances et m'a aidé, quand le besoin s'en faisait ressentir, à oublier quelque peu le travail de thèse.

Je terminerai par remercier profondément ma famille, mes parents pour leur soutien sans faille, ainsi que Julie, dont la patience et le dévouement lors des derniers mois de thèse furent exceptionnels, malgré mes nombreux accès de mauvaise humeur à l'approche des échéances.

Cette thèse a été réalisée avec le soutien du Fonds pour la formation à la Recherche dans l'Industrie et l'Agriculture (FRIA), de la Communauté Française de Belgique au travers du contrat d'Action de Recherche Concertées SLIM (ARC 04/09-316), ainsi que de la politique scientifique fédérale belge (BELSPO) par le biais du pôle d'attraction interuniversitaire TIMOTHY (PAI6.13).

Contents

Introduction

Marine waters cover 70% of the surface of the planet and represent 97% of all the water of the earth. About half of mankind living in coastal regions, marine systems are strongly linked with human activities. They are provider of resources (food, tourism,...) but are also used as waste disposal areas. Being the habitat of 99% of the life of the planet, they have a considerable effect over earth ecosystems. Water pollution is one of the main causes of their irreversible degradation (Ellis, 2000; Rajaram and Das, 2008; Camargo and lvaro Alonso, 2006), but hydrodynamics also plays a role in their evolution. Flow velocities and turbulence influence significantly the sediment structure, erosion and deposition. Wind and ocean currents allow nutrient-rich water from the sea bottom to rise to the surface, contributing to plankton blooms (Figure 1). These phenomena affect the local fauna and flora and their repartition (Asmus *et al.*, 2007). For example, Riisgård *et al.* (2007) showed that mixing in the Odense Fjord (Denmark), by resuspending phytoplankton and making it available to filter-feeding species, divided its lifetime by a factor of two. Larvae and eggs are also directly carried by local and large scale water circulation over distances up to hundreds of kilometers (Williams *et al.*, 1984; Wolanski, 1994). These modifications at the individual or species level can cause interactions with other physical parameters or species (Asmus *et al.*, 2007).

Even though natural processes have an effect over the physical properties of marine systems, the human influence is undeniable and varied. Industrial discharges, urbanization and agriculture contribute among others to water pollution (Ellis, 2000; Rajaram and Das, 2008; Tuncer *et al.*, 1998). Human-induced climate change has an influence on water properties such as temperature, circulation patterns and sea level (Lewsey *et al.*, 2004; Munday *et al.*, 2009). Human activities also affect directlty the hydrodynamics by modifying the topography with dredging (Liria *et al.*, 2009), reclaimed land (Gong *et al.*, 2008) or by constructing dams upstream estuaries (Kim *et al.*, 2006; lun Yang *et al.*, 2002).

At the current level of development, preventing human activities from influencing the marine hydrodynamics, morphology and ecosystems is impossible. However, a good knowledge of the marine system would allow to reduce this influence, or limit its harmful consequences by different means:

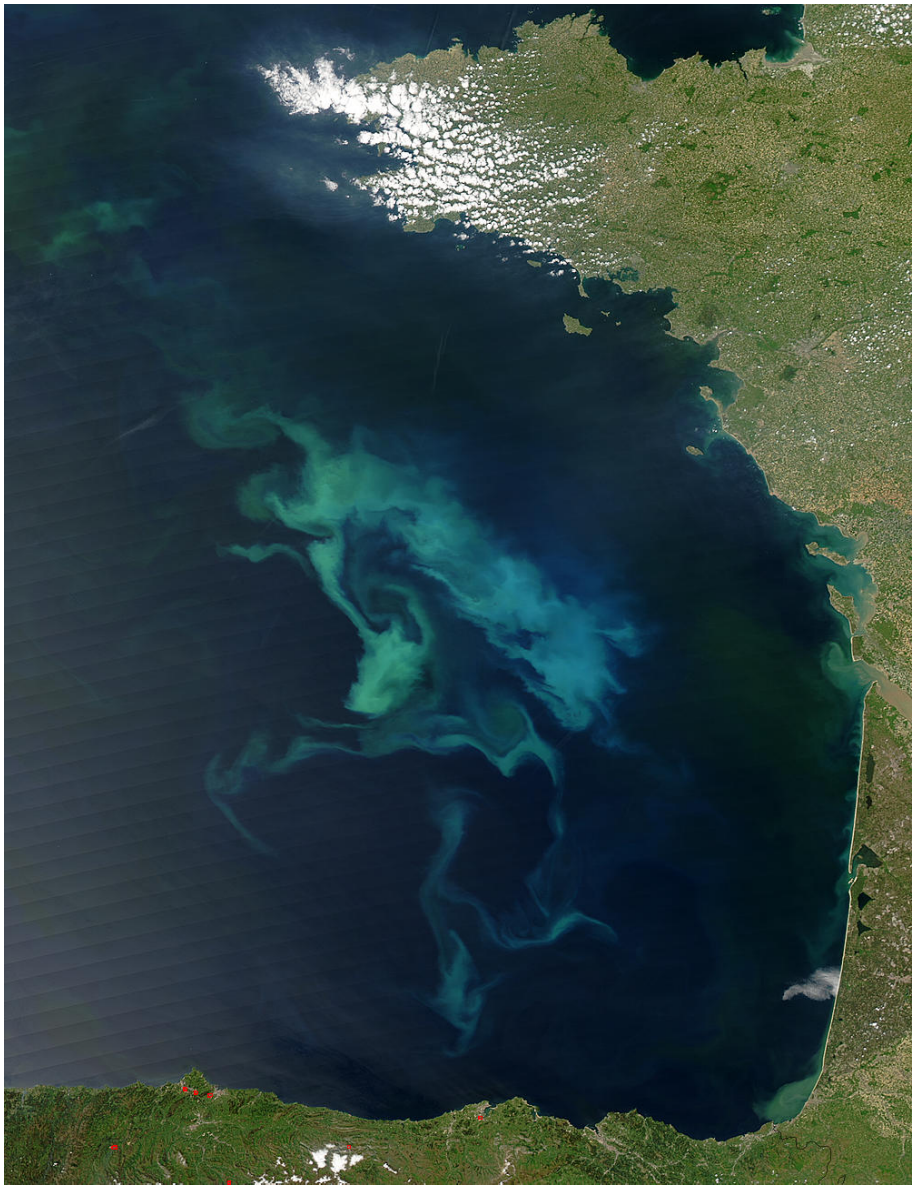

Figure 1: Phytoplankton bloom in the Bay of Biscay (France). Phytoplankton are sensitive to available sunlight and local environmental variations such as nutrient levels, temperature, currents and winds. Source: NASA

- Predicting the impact of development projects (discharges, coastal engineering,...) to choose the safest alternative.
- Identifying some factors having a harmful influence on the ecosystems, and developing remediation techniques.
- Helping to quantify the economical value of ecosystems services to influence policy decisions (Chee, 2004).

Although the knowledge of a marine system can be acquired from observations, the latter are generally expensive and may require an alteration of water properties (e.g. discharge of tracers to be followed). Furthermore, these observations do not allow to predict the consequences of modifying the configuration on water properties (adding pollutants, changing the topography,...). Reduced scale models can provide informations about the influence of different configurations, but they are long and complex to build. The principles of physical similitude must be respected, leading sometimes to distorted model ratios (Hughes, 1993). They can be too simple to take into account the complexity of the flow and the results can be difficult to observe and interpret. Another solution is to use a numerical model to simulate the marine system. Once the model is calibrated, many different simulations can be performed, only limited by the computational cost. These models allow sensitivity studies or estimations of the influence of different configurations over the marine system (e.g. human works, tracer discharge, remediation,...). A model is an interactive way to learn about the response of the system to any perturbation. Furthermore, models output are defined over the whole domain, which makes their interpretation or the computation of diagnostic variables easier. They need datasets (e.g. forcings, salinity, temperature, bathymetry...), which can be obtained from field surveys (Wolanski *et al.*, 1996), satellite data (Egbert *et al.*, 1994) or other models.

Numerical models are used to simulate domains of interest either restricted to a specific region (local or regional models) or covering the whole world ocean (global models). Limited by the computing time, the resolution of models is not able to represent the whole spectrum of phenomena occuring in the considered domain, as their characteristic sizes vary from $1\ mm$ to more than $10\ 000\ km$ in the world ocean (Figure 2). Regional models present various resolutions, starting from dozens of meters. Global ocean models are generally too coarse to explicitly represent mesoscale eddies. High resolution models (with grid sizes of order $10\ km$) are able to represent those eddies, but no computer is able to run them for a few hundreds to a few thousands of years, as is necessary to study the earth climate. In the last decade, coupled atmosphere-ocean climate models had their horizontal resolution in the ocean increased from about $300\ km$ in 1998 to $25\ km$ nowadays using the UK Research Council's new supercomputer HECTOR (Slingo *et al.*, 2009). Although small in comparison with the computational domain, unresolved processes may have a critical impact over the structure of larger scales which are ex-

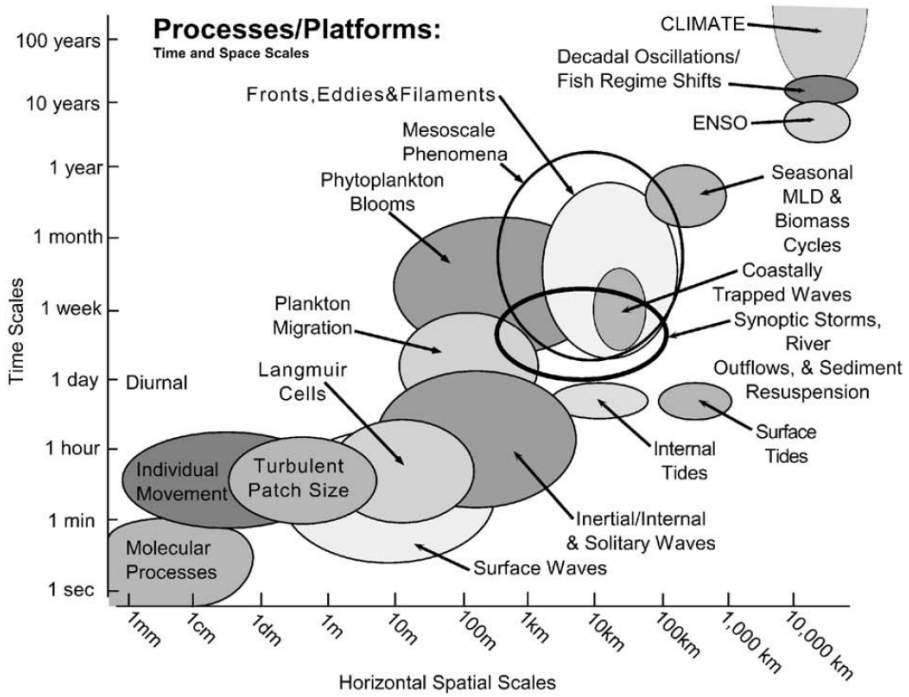

Figure 2: Time and horizontal space scales of several physical and biological marine processes, from Dickey (2003).

plicitely represented (Griffies, 2004). Some parameterisations, designed from physical considerations, need to be developed to take this effect into account (e.g. turbulence can be parameterised by the means of a diffusion operator (Burchard, 2002a)). A different parameterisation must be developed for each of the many unresolved physical processes, as these processes impact differently the larger scale properties. A major part of the present thesis is related to the treatment of unresolved physics. Unresolved phenomena can be related to the whole domain, or specifically located near some boundaries. In the latter case, they are referred to as "boundary layers" in which the variation of some physical variables is much steeper than their variation in the mean flow. When related to boundary layers, the numerical representation may also be improved to handle the steep variation of the variables without refinement of the mesh (Hanert *et al.*, 2007). In that case, no parameterisation is needed. Another type of unresolved physics is related to phenomena that cannot be represented due to a dimensional restriction of the model, e.g. a two-dimensional phenomena in a one-dimensional model. In some cases, it can be justified to parameterise these phenomena to obtain useful results in a simple model.

Numerical marine models have been extensively developed in the recent years. Their range increased from single discipline studies such as hydrodynamics to coupled physical-chemical-biological ecosystems modelling. However, many of these models still use the same underlying numerical scheme: the finite difference method. Being simple to implement, this method is limited to be used on structured grids. This implies several restrictions of such models. The coastlines can only be defined using a staircase representation, which induces spurious vorticity and mixing (Dupont *et al.*, 2003). The grid resolution does not vary over the computational domain. The global grid resolution must then be chosen smaller than the charachteristic length of the smallest phenomena in which we are interested. However, these phenomena generally occur (or are of interest for the modeller) in a limited area of the domain, and a variable grid resolution is more efficient. Nested grids provide a flexible variable resolution. It consists of a high resolution grid incorporated within a lower resolution grid. However the transfer of information between the different grids is problematic. The interpolation between grids must ensure mass conservation and should not generate numerical noise or reflection of waves, which is far from easy (Debreu and Blayo, 2008). Unstructured grids are an alternative to nested grid models. No interpolation is required to transfer information from one region of the domain to another. Furthermore, they avoid wave reflection issues if the transition from fine to coarse resolution is sufficiently smooth. An example of the potential of unstructured grids is the Great Barrier Reef, a group of over 2500 coral reefs located on the Australian northeast continental shelf. Local data and simulations showed that small scale phenomena mainly appear in the neighbourhood of small reefs, islands and passages (Lambrechts *et al.*, 2008b). A powerful approach to simulate the flow is to refine the resolution near these topographic features, while

the main resolution is coarser. Such an approach has been used, relying on unstructured grids (Figure 3), by Lambrechts *et al.* (2008b) who computed the hydrodynamics over the whole Barrier Reef. In this perspective, several efforts were done to build unstructured grids for plane or spherical geophysical simulations (Lambrechts *et al.*, 2008a). In a global scale model, unstructured grids are useful to represent mesoscale eddies that are present in a relative small fraction of the global ocean, but contains a significant part of the kinetic energy of the world ocean.

Different metods can handle unstructured grids, both for coastal and global scale applications. Finite volume methods are now widely used, and models like FVCOM (Chen *et al.*, 2003a) have a large community of users. Many other finite volume models are developed for coastal and estuarine studies (Fringer *et al.*, 2006; Ham *et al.*, 2005; Casulli and Walters, 2000) or large scale simulations (Stuhne and Peltier, 2006). Another popular approach is the finite element method. Since the first attempts to build finite element marine models, different formulations were considered. The first models were developed using linear continuous elements for both velocity and elevation (Lynch *et al.*, 1996). Spurious oscillations were avoided by solving a wave equation for the elevation, losing in this way mass conservation. The mixed formulation RT_0 was then considered (Miglio *et al.*, 1999; Walters and Casulli, 1998). However this formulation allows the existence of spurious velocity modes having to be filtered. The $P_1^{NC}P_1$ pair, linear non-conforming for the velocity and linear conforming for the elevation was shown to be free of spurious velocity and elevation modes (Hanert *et al.*, 2005); and was successfully used in a three-dimensional shallow-water model (White *et al.*, 2008a). Recent studies presented the potential interest of the $P_1^{DG} - P2$ (Cotter *et al.*, 2009) and $P_1^{NC} - P_1^{NC}$ (Comblen *et al.*, 2009b) pairs that should be further studied. Discontinuous Galerkin methods are focusing growing interest for coastal and estuarine modelling (Aizinger and Dawson, 2002; Dawson and Aizinger, 2005; Kubatko *et al.*, 2006; Aizinger and Dawson, 2007; Bernard *et al.*, 2008b). For large scale ocean modelling, continuous finite element methods are used in FEOM (Wang *et al.*, 2008a,b; Timmermann *et al.*, 2009), and ICOM relies on mesh adaptivity to capture the multiscale aspects of the flow (Piggott *et al.*, 2008). The Spectral Element method was considered for marine modelling (Iskandarani *et al.*, 1995), but produces oscillations in the numerical solution when the boundaries are irregular.

While the finite volume method is well suited for convection dominated flows, it is restricted to a low order representation of the solution. In contrast, the finite element method benefits from the functional flexibility, allowing a high order representation of the solution field; but it is designed for diffusion problems and needs stabilisation when advection becomes significant. Discontinuous Galerkin methods are a kind of hybrid between finite elements and finite volumes. They allow to keep most of the qualities of both schemes while avoiding their drawbacks: the expression of the fluxes between elements allows to use stable upstream-biased schemes, as for finite volumes

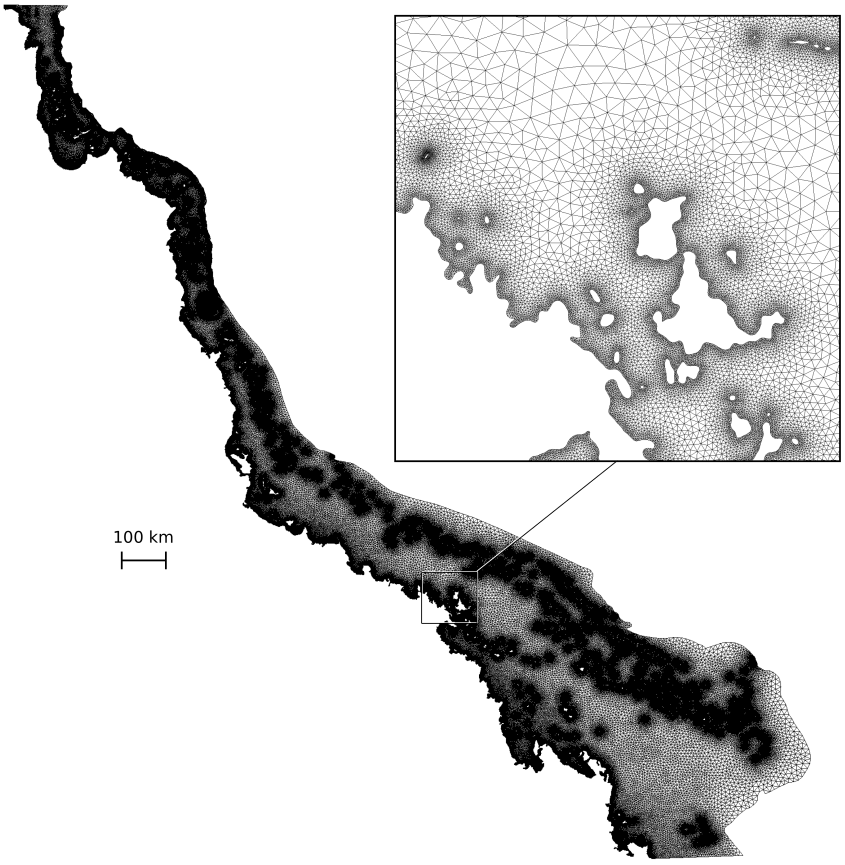

Figure 3: Unstructured mesh of the Great Barier Reef (northeast Australia), from (Lambrechts *et al.*, 2008b). The mesh contains 850 843 triangles of characteristic sizes between $150\ m$ and $10\ km$.

methods, and the polynomial interpolation used inside each element allows a high order representation of the solution. Further, no degree of freedom is shared between two geometric entities, and this high level of locality considerably simplifies the parallel implementation of the method.

The **first chapter** of this thesis describes the three-dimensional Discontinuous Galerkin marine model developed in the framework of the present work. Some results of baroclinic simulation are then shown and discussed. The rest of the thesis is devoted to different types of unresolved physics in marine models. The **second chapter** introduces two different boundary layers appearing in marine modelling: the bottom velocity boundary layer related to the hydrodynamics, and the boundary layer of the residence time which is a diagnostic variable. Both parameterisation and representation using the extended finite element method will be discussed and compared. The parameterisation of the density gradient in one-dimensional baroclinic models is introduced in **Chapter 3**. The point is to parameterise phenomena which are not in the dimensional space of the model. The attention is paid to the stability of the parameterisation under different physical conditions. **Chapter 4** is related to subgrid scale turbulence modelling in three-dimensional models, and compares the effect of different parameterisations on a realistic simulation of the flow around a shallow-water island.

This work was undertaken within the scope of the SLIM[1] project that aims at building a three-dimensional unstructured-mesh, finite-element ice-ocean model. In the framework of the development of this model, this thesis provides practical solutions related to various numerical issues appearing in marine modelling. As different alternative methods exist, we try to identify the advantages and drawbacks of those alternatives to help with the choice of the appropriate method for a specific configuration. Marine modelling is the subject of an active research, particularly since new models have appeared, relying on unstructured grids. The work presented here fits into this evolution and tries to help improving the representation and understanding of marine processes. Some developments were carried out under the auspices of the TIMOTHY[2] project. Its main objective is to develop, validate and apply tools to describe and evaluate the changes in quality of surface, ground and marine waters. In this perspective, the developed tools are applied to realistic domains, which confirms their applicability to real configurations.

[1] Second-generation Louvain-la-Neuve Ice-ocean model (`http://www.climate.be/SLIM`)

[2] Tracing and Integrated Modeling of Natural and Anthropogenic Effects on Hydrosystems : The Scheldt River basin and adjacent coastal North Sea (`http://www.climate.be/TIMOTHY`)

Supporting publications

Hanert, E., Deleersnijder, E., Blaise, S., and Remacle, J.-F. 2007. Capturing the bottom boundary layer in finite element ocean models. Ocean Modelling, 17:153–162.

Blaise, S., Deleersnijder, E., White, L., and Remacle, J.-F. 2007. Influence of the turbulence closure scheme on the finite-element simulation of the upwelling in the wake of a shallow-water island. Continental Shelf Research, 27:2329–2345.

Blaise, S. and Deleersnijder, E. 2008. Improving the parameterisation of horizontal density gradient in one-dimensional water column models for estuarine circulation. Ocean Science, 4:239–246.

Blaise, S., de Brye, B., de Brauwere, A., Deleersnijder, E., Delhez, E. J., and Comblen, R. 2009b. Capturing the residence time boundary layer - Application to the Scheldt Estuary. Ocean Dynamics, *submitted*.

Blaise, S., Comblen, R., Lambrechts, J., Legat, V., Remacle, J.-F., and Deleersnijder, E. 2009a. A discontinuous finite element baroclinic model for marine modeling. Part I: model description. *In preparation*.

Comblen, R., Blaise, S., Lambrechts, J., Legat, V., Remacle, J.-F., and Deleersnijder, E. 2009a. A discontinuous finite element baroclinic model for marine modeling. Part II: model validation. *In preparation*.

Chapter 1

A three-dimensional Discontinuous Galerkin baroclinic marine model

This chapter focuses on the development of a marine model that should be able to deal with problems ranging from local and regional scales to global scales. The hydrostatic Boussinesq equations are considered. A novel mode splitting procedure is described to treat implicitly fast surface gravity waves. We focus on Discontinuous Galerkin methods because of their intrinsic qualities for advection dominated processes, and the possible decoupling of horizontal and vertical dynamics, thanks to the block-diagonal mass matrix.

1.1 Governing equations

Large scale ocean models usually solve the hydrostatic Boussinesq equations. The conservation of mass degenerates into a conservation of volume, and the density variations are taken into account in the pressure gradient term only. The hydrostatic hypothesis assumes that the vertical momentum equation is reduced to a balance between pressure gradient and gravitational forcing. This Section describes in details this set of equations, and highlight the key points that need to be dealt with.

Spatial operators	
x, y	Horizontal coordinates
z	Vertical coordinate, pointing upwards with its origin at the sea surface at rest
∇_h	Horizontal gradient operator
$\boldsymbol{e}_z$	Upward unit normal
$\wedge$	Cross product symbol
$< x >$	Integral of x over the whole volume
$\ll x \gg$	Integral of x over the boundary of the whole volume
$< x >_{\Omega_e}$	Integral of x over the the element Ω_e
$\ll x \gg_{\partial\Omega_e}$	Integral of x over the boundary of the element Ω_e
$\ll x \gg_{\Delta_c}$	Integral of x over the horizontal surface corresponding to the triangle Δ_c
$\int_V x \, \mathrm{d}z$	Integral of x over the water depth
n_z	Vertical component of the outgoing normal of the boundary of the element
$\boldsymbol{n}_h$	Horizontal components of the outgoing normal of the boundary of the element
n_x	First component of $\boldsymbol{n}_h$
n_y	Second component of $\boldsymbol{n}_h$
Variables, datasets and parameters	
t	Time
η	Free-surface elevation
$\boldsymbol{U}$	Two-dimensional horizontal mean velocity vector
$\mathbf{u}$	Three-dimensional horizontal velocity vector
w	Three-dimensional vertical velocity
c	Three-dimensional tracer, can be S or T
S	Salinity field
T	Temperature field
g	Gravitational acceleration
ρ_0	Reference density
ρ'	Density deviation field
ρ	Density field, $\rho = \rho_0 + \rho'$
p	Baroclinic pressure field
f	Coriolis parameter
h	Depth at rest
H	Total water depth, $H = h + \eta$
ν_h	Horizontal turbulent viscosity parameter
ν_v	Vertical turbulent viscosity parameter
κ_h	Horizontal turbulent diffusivity parameter
κ_v	Vertical turbulent diffusivity parameter

Table 1.1: Details of the mathematical notations used.

The Boussinesq equations are the following (details of notations are found in Table 1.1) :

- Horizontal momentum equation:

$$\frac{\partial \mathbf{u}}{\partial t} + \nabla_h \cdot (\mathbf{u}\mathbf{u}) + \frac{\partial (w\mathbf{u})}{\partial z} + f\mathbf{e}_z \wedge \mathbf{u} + \frac{1}{\rho_0}\nabla_h p + g\nabla_h \eta = \nabla_h \cdot (\nu_h \nabla_h \mathbf{u}) + \frac{\partial}{\partial z}\left(\nu_v \frac{\partial \mathbf{u}}{\partial z}\right), \quad (1.1)$$

- Continuity equation:

$$\nabla_h \cdot \mathbf{u} + \frac{\partial w}{\partial z} = 0, \quad (1.2)$$

- Free-surface equation:

$$\frac{\partial \eta}{\partial t} + \nabla_h \cdot \int_{-h}^{\eta} \mathbf{u} dz = 0, \quad (1.3)$$

- Tracer equation:

$$\frac{\partial c}{\partial t} + \nabla_h \cdot (\mathbf{u}c) + \frac{\partial (wc)}{\partial z} = \nabla_h \cdot (\kappa_h \nabla_h c) + \frac{\partial}{\partial z}\left(\kappa_v \frac{\partial c}{\partial z}\right), \quad (1.4)$$

- Baroclinic pressure equation:

$$\frac{\partial p}{\partial z} = -g\rho(T,S) \qquad \text{with} \qquad \rho = \rho_0 + \rho'(T,S). \quad (1.5)$$

The baroclinic pressure equation is derived from the vertical momentum equation using the hydrostatic approximation. This system of equation is of mixed type. Depth-integrated, it reduces to the shallow water equations, that are hyperbolic and parabolic, but with an hyperbolic component that dominates. The hyperbolic character of these equations is taken into account in finite volume or Discontinuous Galerkin formulations using a Riemann solver to deduce the value of the fields at the interelement interfaces (LeVeque, 2002; Toro, 1997). It enables upwinding on the characteristic variables.

The momentum system can be seen as stacked shallow water systems. The coupling between those layers is ensured only by the vertical advection and diffusion. In the inviscid limit, impermeability cannot be imposed on lateral boundary conditions, as the momentum equation becomes hyperbolic, and only incoming characteristics can be prescribed (Rousseau *et al.*, 2004).

The vertical velocity is not deduced from a momentum equation, but rather from the incompressibility equation integrated from bottom to top. The density deviation ρ' is deduced from temperature and salinity using an appropriate equation of state.

Viscosity and diffusivity coefficients are chosen to represent the different effects of each of the many unresolved physical processes. Some dissipation is also generated by the numerical scheme. The total mixing is then the sum of the numerical mixing and the dissipation which is explicitely added. However, this numerically induced mixing should be the smallest possible, and should be only present when and where it is needed in order to keep the model stable. It is important that the level of numerical mixing do not overwhelms the level of mixing induced by the physically based parameterisation. Unfortunately, the latter requirement is not fulfilled in many ocean models. It is possible to quantify the numerical mixing induced by the model (Burchard and Rennau, 2008), and such a technique should be applied to the SLIM model in a later study to confirm that additional diffusion must be added to represent the effect of unresolved phenomena.

The viscosity and diffusivity are strongly anisotropic (Griffies, 2004). If we consider a fluid stratified only in the vertical direction, stratification tends to anihilate any motion along the vertical. As a consequence, many transport processes tend to spread properties more efficiently along isopycnal surfaces (horizontal direction) rather than across (vertical direction). Measurements of the tracer diffusivity in the ocean by Ledwell *et al.* (1993) showed that, at the larger scales (order of hundreds of kilometers), the ratio between horizontal and vertical mixing can be up to eight orders of magnitude. Particular attention must be paid to ensure the stability and accuracy of the anisotropic diffusion scheme, as discussed in Section 1.6. The subgrid scale phenomena are completely different whether they are related to the horizontal or the vertical direction. Vertical processes consist of small scale (from some millimeters to some meters) turbulence, mainly generated by shear instabilities and gravitational instabilities. Due to their very small scales, these processes are never resolved in ocean models. Horizontal dominant subgrid scale processes correspond to larger scales of motions such as the mesoscale eddies (tens to hundreds of kilometers). In that case, larger phenomena can be resolved by the model, depending of the resolution, and the eddy diffusivity must increase with the mesh size.

1.2 Time discretization

1.2.1 Mode splitting procedure

Explicit methods have stability constraint on the time step related to the fastest propagation phenomenon. In the hydrostatic Boussinesq system, the surface gravity waves are the fastest phenomenon, and the related stable time-step is so small that long term completely explicit simulations require by far too many iterations. However, we cannot afford to solve implicitly the whole coupled equations. The size of the resulting system is so large that the memory requirements are unaffordable.

An efficient strategy to solve implicit free-surface is to solve a smaller system corresponding to the Schur complement of the global system. If the linear discrete system corresponding to equations (1.1) and (1.3) reads:

$$\begin{bmatrix} M_{\mathbf{u}} & G \\ D & M_\eta \end{bmatrix} \begin{bmatrix} X_{\mathbf{u}} \\ X_\eta \end{bmatrix} = \begin{bmatrix} f_{\mathbf{u}} \\ f_\eta \end{bmatrix}, \tag{1.6}$$

where $M_{\mathbf{u}}$, M_η and $X_{\mathbf{u}}$, X_η are respectively the mass matrices and vectors of degrees of freedom for velocities and elevation. G and D correspond respectively to the elevation gradient term of (1.1) and the velocity divergence term of (1.3), while $f_{\mathbf{u}}$ and f_η are their righ-hand-sides. An equivalent smaller system for the elevation is obtained substituting $X_{\mathbf{u}}$ in the last line of the system:

$$\left[M_\eta - DM_{\mathbf{u}}^{-1}G\right] X_\eta = f_\eta - DM_{\mathbf{u}}^{-1} f_{\mathbf{u}} \tag{1.7}$$

Such a methodology is found in Dukowicz and Smith (1994) as well as in Marshall *et al.* (1997) for global-scale models, but also in Giraldo *et al.* (2003) for shallow water problems on the sphere. For this methodology to be efficient, the mass matrix for velocities $M_{\mathbf{u}}$ must be easily invertible, hence diagonal or block-diagonal. For continuous finite elements, mass lumping must be performed for such a methodology to apply. If some differential implicit operators are added to $M_{\mathbf{u}}$, its inversion may become difficult.

The finite element ocean model FEOM uses a similar approach (Wang, 2007). The semi-discrete implicit form of the free-surface equation (1.3) is

$$\frac{\eta^{n+1} - \eta^n}{\Delta t} + \nabla_h \cdot \int_{-h}^{0} u^{n+1} \mathrm{d}z = 0, \tag{1.8}$$

where Δt is the time step while n and $n+1$ correspond respectively to the old and new times of the temporal discretisation. If we consider that only the elevation gradient is implicit in equation (1.1), the new velocity u^{n+1} is determined using

$$\frac{u^{n+1} - u^n}{\Delta t} = -g\nabla_h \eta^{n+1} + F^{\text{explicit}}, \tag{1.9}$$

where F^{explicit} includes explicit terms. This expression can be substituted in (1.8) to obtain an implicit free-surface:

$$\frac{\eta^{n+1} - \eta^n}{\Delta t} + \nabla_h \cdot \int_{-h}^{0} \left[u^n + \Delta t \left(-g\nabla_h \eta^{n+1} + F^{\text{explicit}}\right)\right] \mathrm{d}z = 0. \tag{1.10}$$

If an implicit vertical diffusion is used to reduce time step limitations, an intermediate velocity must be introduced to allow the substitution:

$$\frac{u^* - u^n}{\Delta t} - \frac{\partial}{\partial z} \cdot \nu_v \frac{\partial u^*}{\partial z} = -g\nabla_h(\eta^n) + F^{\text{explicit}}. \tag{1.11}$$

The new velocity u^{n+1}, determined using a correction step

$$\frac{u^{n+1} - u^*}{\Delta t} = -g\nabla_h(\eta^{n+1} - \eta^n), \tag{1.12}$$

can be substituted into the free-surface equation (1.8):

$$\frac{\eta^{n+1} - \eta^n}{\Delta t} + \nabla_h \cdot \int_{-h}^{0} \left[u^* - \Delta t\, g\nabla_h \left(\eta^{n+1} - \eta^n\right)\right] \mathrm{d}z = 0. \tag{1.13}$$

Equation (1.11) is first solved to obtain u^*. Then, the implicit free-surface can be deduced by solving equation (1.13). Finally, the velocity is obtained from equation (1.12). Implicit vertical viscosity is neglected in the correction step. That is needed to be able to perform the subtitution and obtain (1.13). Then, velocity can be obtained by solving equation (1.9). The method of substitution is similar to the Schur complement approach used by Dukowicz and Smith (1994), but the substitution is performed in the continuous space rather than at the discrete level. Reasoning in the continuous world is so that the inverse of the mass matrix $M_{\mathbf{u}}^{-1}$ disappears in what corresponds to the Schur complement; and the discrete operator is not the same.

Another method usually performed by ocean models is mode splitting. Indeed, the free-surface evolution only depends on the depth-integrated velocities, but not on the details of the three-dimensional field. Therefore, the vertically averaged equations are used to deduce the sea surface elevation evolution using a small time step, while the three-dimensional baroclinic mode is evolved using a larger time-step. Three-dimensional velocities are generally a posteriori corrected so that their mean matches the velocities of the barotropic mode (Blumberg and Mellor, 1987; Gadd, 1978). The barotropic mode can also be time-stepped implicitly, using the same time-step as the baroclinic mode. The advantage of the mode splitting approach is that the barotropic mode corresponds to the well known shallow water equations. Its discretisation and the expression of interface fluxes ares stable and validated (Comblen *et al.*, 2009b). We chose to use this approach, with the same time step for the baroclinic mode (explicit) and the barotropic mode (implicit).

The two-dimensional shallow water momentum equation is the result of the depth-integration of Equation 1.1. It is shown in Appendix A that this depth-integration can be obtained by summing the lines and columns of the three-dimensional discrete system matrix and vector whose corresponding nodes share the same vertical. We then derive the barotropic equations by discretely adding all three-dimensional contributions onto the corresponding two-dimensional degree of freedom. We neglect implicit vertical advection and vertical diffusion of momentum in the barotropic mode, that introduce a small horizontal coupling due to the nondiagonal mass matrix. It is also possible to treat these terms explicitely in the barotropic mode, and obtain an approximation similar to what is done by Wang (2007). Identity between depth-averaged three-dimensional velocity and two-dimensional velocity is

enforced using Lagrange multipliers in the three-dimensional system. It is better to use Lagrange multipliers than a posteriori correct the velocities as this correction is taken into account in the terms treated implicitly, such as Coriolis. The effect of these Lagrange multipliers is to correct the discrepancy due to the different treatment of vertical terms in the baroclinic and barotropic modes. The correction is not optimal, because the finite element space used for the Lagrange multipliers correction (surface term; constant over the vertical) is smaller than the space used for vertical dynamics terms (volume term with interface terms on horizontal faces; variable along the vertical). However, the baroclinic mode is consistent with the barotropic mode, and mass conservation is ensured.

1.2.2 Overall time discretization

We use implicit/explicit Runge-Kutta time stepping schemes (Ascher *et al.*, 1997), where stiff linear terms are treated implicitly while nonlinear terms are treated explicitly. For the momentum and free-surface equations, the terms related to surface gravity waves, vertical advection, vertical diffusion, and Coriolis are treated implicitly, while horizontal advection and diffusion are explicit. The resulting linear system to solve is block, each block corresponding to a column of prisms. It is then not necessary to build a three-dimensional global matrix, and the memory usage is highly reduced. The parallel scaling is strong as each block system is solved independently. Tracers are fully implicit to avoid a restriction on the time step due to a large tracer diffusivity. Different equations are solved at each Runge-Kutta sub-time step in an order defined by the following sequence:

1. Compute the terms common to two and three-dimensional modes
2. Solve the two-dimensional mode to obtain $\boldsymbol{U}$ and η
3. For each column of prisms
   (a) Compute the implicit terms for the three-dimensional momentum
   (b) Compute the constraint matching $\mathbf{u}$ mean with $\boldsymbol{U}$
   (c) Solve the related local linear system, using a direct sparse solver to obtain $\mathbf{u}$
4. Solve the incompressibility equation to obtain w
5. For each tracer
   (a) Compute the terms
   (b) Solve the linear system
6. Compute the density field ρ
7. Compute the baroclinic pressure gradient field to obtain $\nabla_h p$

1.3 Weak formulation and spatial discretization

Equations (1.1) to (1.5) are discretized in space using the finite element method. As already mentioned, linear Discontinuous Galerkin elements are used except for density deviation and baroclinic pressure gradient (Table 1.2). The justifications of this choice will be given in the corresponding paragraphs. Prismatic elements obtained from the extrusion of triangular two-dimensional elements are used, taking into account the high anisotropy found in marine waters.

1.3.1 Riemann solver at the interfaces

The two-dimensional barotropic equations are deduced from the depth-integration of the three-dimensional set of equations. These two-dimensional equations are similar to the shallow water equations. Therefore, depth-integration of the three-dimensional terms should be close to usual discretization of the shallow water equations. Indeed, the lateral interface terms must be chosen in a way that warrants a robust two-dimensional discretization. Comblen *et al.* (2009b) describe in details a finite element formu-

Field		Finite element space
Free surface elevation	η	P_1^{DG}
2d horizontal mean velocity vector	$\boldsymbol{U}$	P_1^{DG}
Horizontal three-dimensional velocity vector	$\mathbf{u}$	$P_1^{DG} \times L_1^{DG}$
Vertical three-dimensional velocity	w	$P_1^{DG} \times L_1^{DG}$
Three-dimensional tracer	c	$P_1^{DG} \times L_1^{DG}$
Density deviation	ρ'	$P_1 \times L_1$
Baroclinic pressure gradient	$\boldsymbol{F}_p$	$P_1 \times L_1$

Table 1.2: Summary of the finite element spaces used for each field. Triangular linear elements are noted P_1 while vertical linear elements are noted L_1. The superscript DG stands for Discontinuous Galerkin.

lation for the shallow water equations, where stabilizing terms appear in the interface terms only. Our Discontinuous Galerkin formulation falls within this framework.

Due to the discontinuous representation of the variables, they are double-valued at the interface between elements, and must be defined in a way to ensure stability and accuracy. Riemann solvers are used to deduce proper values of the variables at the interface. For the boundary integrals corresponding to linear terms, we use the values from the Riemann solver of the linearized two-dimensional equations, i.e. the linear shallow water equations, that are a wave equation. If we define respectively $\{a\} = \frac{a^{\text{in}}+a^{\text{ext}}}{2}$ and $[a] = \frac{a^{\text{in}}-a^{\text{ext}}}{2}$ the mean and the jump of a at the interface, those values read:

$$\mathbf{u}^{\text{Riemann}} = \mathbf{u} + \sqrt{\frac{g}{h}}[\eta]\,, \quad \eta^{\text{Riemann}} = \eta + \sqrt{\frac{h}{g}}[\mathbf{u}], \tag{1.14}$$

For the boundary integrals corresponding to nonlinear terms, we use the values from the Roe approximate Riemann solver of the nonlinear two-dimensional equations, i.e. the nonlinear shallow water equations. Those values are deduced from the conservative variables as (Comblen *et al.*, 2009b):

$$
\begin{aligned}
H^{\text{Roe}} &= \{H\} + \frac{1}{\sqrt{g\bar{H}}}\left([Hu] - \bar{u}\,[H]\right), && (1.15)\\
(Hu)^{\text{Roe}} &= \{Hu\} + \frac{1}{\sqrt{g\bar{H}}}\left(\bar{u}\,[Hu] - \bar{u}^2\,[H]\right), && (1.16)\\
(Hv)^{\text{Roe}} &= (Hv)_{\text{upwind}} + \bar{v}(\{H\} - H_{\text{upwind}}) && (1.17)\\
&\quad + \frac{1}{\sqrt{g\bar{H}}}\left(\bar{v}\,[Hu] - \bar{u}\bar{v}\,[H]\right), && (1.18)\\
\eta^{\text{Roe}} &= H^{\text{Roe}} - h, && (1.19)\\
u^{\text{Roe}} &= \frac{(Hu)^{\text{Roe}}}{H^{\text{Roe}}}, && (1.20)\\
v^{\text{Roe}} &= \frac{(Hv)^{\text{Roe}}}{H^{\text{Roe}}}. && (1.21)
\end{aligned}
$$

where the Roe means are:

$$
\begin{aligned}
\bar{H} &= \{H\}, && (1.22)\\
\bar{u} &= \frac{u_L\sqrt{H_L} + u_R\sqrt{H_R}}{\sqrt{H_L} + \sqrt{H_R}}, && (1.23)\\
\bar{v} &= \frac{v_L\sqrt{H_L} + v_R\sqrt{H_R}}{\sqrt{H_L} + \sqrt{H_R}}. && (1.24)
\end{aligned}
$$

1.3.2 Momentum equation

The weak continuous formulation of the horizontal momentum equation is obtained by multiplying equation (1.1) by a test function $\widehat{\mathbf{u}}$ and integrating over the whole domain Ω:

$$
\begin{aligned}
&< \widehat{\mathbf{u}} \cdot \frac{\partial \mathbf{u}}{\partial t} > + < \widehat{\mathbf{u}} \cdot (\nabla_h \cdot (\mathbf{u}\mathbf{u})) > + < \widehat{\mathbf{u}} \cdot \frac{\partial w\mathbf{u}}{\partial z} >\\
&\qquad + < \widehat{\mathbf{u}} \cdot f\mathbf{e}_z \wedge \mathbf{u} > + < \widehat{\mathbf{u}} \cdot \frac{1}{\rho_0}\nabla_h p > + < \widehat{\mathbf{u}} \cdot g\nabla_h \eta >\\
&\qquad - < \widehat{\mathbf{u}} \cdot (\nabla_h \cdot (\nu_h \nabla_h \mathbf{u})) > - < \widehat{\mathbf{u}} \cdot \frac{\partial}{\partial z}\left(\nu_v \frac{\partial \mathbf{u}}{\partial z}\right) >= 0, \quad (1.25)
\end{aligned}
$$

where $< \cdot >$ denotes the volume integral over Ω. The latter is then split into N_e elements Ω_e to allow the spatial discretization:

$$\sum_{e=1}^{N_e} \Bigg[\underbrace{< \widehat{\mathbf{u}} \cdot \frac{\partial \mathbf{u}}{\partial t} >_{\Omega_e}}_{1} + \underbrace{< \widehat{\mathbf{u}} \cdot (\nabla_h \cdot (\mathbf{u}\mathbf{u})) >_{\Omega_e}}_{2} + \underbrace{\widehat{\mathbf{u}} \cdot \frac{\partial w \mathbf{u}}{\partial z}}_{3} + \underbrace{< \widehat{\mathbf{u}} \cdot f \mathbf{e}_z \wedge \mathbf{u} >_{\Omega_e}}_{4} + \underbrace{< \widehat{\mathbf{u}} \cdot \frac{1}{\rho_0} \boldsymbol{F}_p >_{\Omega_e}}_{5} + \underbrace{< \widehat{\mathbf{u}} \cdot g \nabla_h \eta >_{\Omega_e}}_{6} - \underbrace{< \widehat{\mathbf{u}} \cdot (\nabla_h \cdot (\nu_h \nabla_h \mathbf{u})) >_{\Omega_e}}_{7} - \underbrace{< \widehat{\mathbf{u}} \cdot \frac{\partial}{\partial z} \left(\nu_v \frac{\partial \mathbf{u}}{\partial z} \right) >_{\Omega_e}}_{8} \Bigg] = 0. \quad (1.26)$$

The latter formulation is still a continuous weak formulation. We now consider a discontinuous representation of the variables. The terms containing spatial derivatives of discontinuous quantities (i.e. all apart from the baroclinic pressure term) are integrated by part in order for the Neumann boundary fluxes to appear. Those terms then read:

$$2 \quad \sum_{e=1}^{N_e} \left[- < \nabla_h \widehat{\mathbf{u}} : \mathbf{u}\mathbf{u} >_{\Omega_e} + \ll \left(\mathbf{u}^{\text{Roe}} \mathbf{u}^{\text{Roe}} \cdot \widehat{\mathbf{u}} \right) \cdot \boldsymbol{n}_h \gg_{\partial \Omega_e} \right]$$

$$3 \quad \sum_{e=1}^{N_e} \left[- < \frac{\partial \widehat{\mathbf{u}}}{\partial z} \cdot w \mathbf{u} >_{\Omega_e} + \ll \left(\widehat{\mathbf{u}} \cdot w^{\text{down}} \mathbf{u}^{\text{upwind}} \right) n_z \gg_{\partial \Omega_e} \right]$$

$$6 \quad \sum_{e=1}^{N_e} \left[- < \nabla_h \cdot \widehat{\mathbf{u}} g \eta >_{\Omega_e} + \ll g \eta^{\text{Riemann}} \widehat{\mathbf{u}} \cdot \boldsymbol{n}_h \gg_{\partial \Omega_e} \right]$$

$$7 \quad \sum_{e=1}^{N_e} \left[\ll \text{interface term} \gg_{\partial \Omega_e} - < \nu_h \left(\nabla_h \widehat{\mathbf{u}} \right) : \left(\nabla_h \mathbf{u} \right)^T >_{\Omega_e} \right]$$

$$8 \quad \sum_{e=1}^{N_e} \left[\ll \text{interface term} \gg_{\partial \Omega_e} - < \frac{\partial \widehat{\mathbf{u}}}{\partial z} \cdot \nu_v \frac{\partial \mathbf{u}}{\partial z} >_{\Omega_e} \right]$$

The interface terms for the diffusion operators 7 and 8 are detailed in Section 1.6 dealing with the treatment of anisotropic diffusion in DG.

Lagrange multiplier to ensure compatibility between 2d and 3d velocities

As described in Section 1.2, we first solve the equation for the two-dimensional elevation and mean velocities, and then we solve the equation for three-dimensional velocities. To ensure that 2d and 3d velocities have the same mean, we use Lagrange multipliers, that act as fictitious forces to project

the three-dimensional velocities onto a space with the right averages. We define the two-dimensional Lagrange multiplier vector field $\boldsymbol{\lambda}$ lying in the same finite element space as the two-dimensional velocities.

Then we add to the linear system for the degrees of freedom of a column of prisms, derived from (1.26), six lines and columns corresponding to the two Lagrange multipliers for each of the three surface nodes. The lines correspond to the compatibility constraint:

$$\sum_{e=1}^{N_e} < \widehat{\lambda}(\mathbf{u} - \boldsymbol{U}) >_{\Omega_e} = 0, \tag{1.27}$$

while the columns corresponds to the fictitious force:

$$\sum_{e=1}^{N_e} \left[< \widehat{\mathbf{u}} \frac{\partial \mathbf{u}}{\partial t} >_{\Omega_e} + \cdots + < \widehat{\mathbf{u}} \lambda >_{\Omega_e} \right] = 0 \tag{1.28}$$

1.3.3 Incompressibility equation

The incompressibility equation is used to deduce the vertical velocity by integrating the horizontal velocity divergence from bottom to top. The weak form of this equation reads:

$$< \hat{w} \frac{\partial w}{\partial z} > + < \hat{w} \nabla_h \cdot \mathbf{u} > = 0. \tag{1.29}$$

This can be split onto a sum on all elements (continuous form):

$$\sum_{e=1}^{N_e} \left[< \hat{w} \frac{\partial w}{\partial z} >_{\Omega_e} + < \hat{w} \nabla_h \cdot \mathbf{u} >_{\Omega_e} \right] = 0. \tag{1.30}$$

Considering a discontinuous representation, we integrate each term by part to get:

$$\sum_{e=1}^{N_e} \Bigg[\ll \hat{w} w^{\text{down}} n_z \gg_{\partial\Omega_e} - < \frac{\partial \hat{w}}{\partial z} w >_{\Omega_e} + \underbrace{\ll \hat{w} \mathbf{u}^{\text{Riemann}} \cdot \boldsymbol{n}_h \gg_{\partial\Omega_e}}_{a} - < \nabla_h \hat{w} \cdot \mathbf{u} >_{\Omega_e} \Bigg] = 0. \tag{1.31}$$

This equation can be viewed as a steady vertical transport equation, with unit velocity, where the divergence of the horizontal velocity is a source term. This expresses that it is a hyperbolic equation, where the information goes from bottom to top. A single boundary condition must be prescribed, at the bottom boundary, where the vertical velocity is nil. This boundary condition

is imposed weakly, by suppressing the boundary integral on the bottom. Further, at the interfaces between layers of prisms, w^{down} must be upwinded.

It can be seen from equation (1.31) that the only term that could prevent horizontal jumps is the term labeled a. However, this term does not contain the jumps of w and, in fact, it appears that it is sufficient only for barotropic applications. To ensure smoothness of the vertical velocity, we add to the left-hand side of (1.31) a penalty term as:

$$- \ll \gamma \hat{w}(w_{\text{in}} - w_{\text{out}}) \gg_{\partial\Omega_e}, \tag{1.32}$$

where γ is a non-dimensional penalty parameter taken as:

$$\gamma = \frac{\text{maximum horizontal edge length}}{h}$$

1.3.4 Free-surface equation

The free-surface equation can be seen as the two-dimensional counterpart of the incompressibility equation. By working on a fixed mesh (see Section 1.3.7) and commuting the divergence operator with the integral, the free-surface equation (1.3) reads

$$\frac{\partial \eta}{\partial t} - \mathbf{u}|_{z=-h} \nabla_h(-h) + \int_{-h}^{0} \nabla_h \cdot \mathbf{u} \, \mathrm{d}z = 0. \tag{1.33}$$

A bottom term appears, which vanishes because the bottom velocity $\mathbf{u}|_{z=-h}$ is imposed at zero (see Section 1.4). The last term of (1.33) is exactly the depth-integration of the velocity divergence term corresponding to the incompressibility equation (1.2). Rather than computing this term twice at the risk of introducing inconsistencies which would break mass conservation, the velocity divergence operator is computed only once for the incompressibility equation. Then, it is discretely depth-integrated by aggregating the lines and columns of the three-dimensional discrete matrix whose corresponding nodes share the same veritcal. It is shown in Appendix A that this aggregation correspond to a depth-integration of the continuous equation. The free-surface discrete equation is then

$$\sum_{e=1}^{N_e} \ll \hat{\eta} \frac{\partial \eta}{\partial t} \gg_{\Delta_e} + \text{aggregated 3d velocity divergence} = 0. \tag{1.34}$$

The penalty term used for the vertical velocity must also be included in the free-surface equation to ensure consistency between equations.

1.3.5 Tracer equation & consistency

The weak formulation for the tracer equation reads:

$$< \hat{c}\frac{\partial c}{\partial t} > + < \hat{c}\nabla_h \cdot (\mathbf{u}c) > + < \hat{c}\frac{\partial wc}{\partial z} > \\ =< \hat{c}\nabla_h \cdot (\kappa_h \nabla_h c) > + < \hat{c}\frac{\partial}{\partial z}\left(\kappa_v \frac{\partial c}{\partial z}\right) > . \quad (1.35)$$

As a sum on each elements, one gets (continuous form):

$$\sum_{e=1}^{N_e}\left[< \hat{c}\frac{\partial c}{\partial t} >_{\Omega_e} + < \hat{c}\nabla_h \cdot (\mathbf{u}c) >_{\Omega_e} + < \hat{c}\frac{\partial wc}{\partial z} >_{\Omega_e} \right] \\ = \sum_{e=1}^{N_e}\left[< \hat{c}\nabla_h \cdot (\kappa_h \nabla_h c) >_{\Omega_e} + < \hat{c}\frac{\partial}{\partial z}\left(\kappa_v \frac{\partial c}{\partial z}\right) >_{\Omega_e} \right]. \quad (1.36)$$

Considering a discontinuous representation, we integrate by part the transport and diffusion terms to obtain:

$$\sum_{e=1}^{N_e}\Bigg[< \hat{c}\frac{\partial c}{\partial t} >_{\Omega_e} + \ll \hat{c}c^{\text{upwind}}\mathbf{u}^{\text{Riemann}} \cdot \boldsymbol{n}_h \gg_{\partial\Omega_e} - < \nabla_h \hat{c} \cdot \mathbf{u}c >_{\Omega_e} \\ + \ll \hat{c}w^{\text{down}}c^{\text{upwind}}n_z \gg_{\partial\Omega_e} - < \frac{\partial \hat{c}}{\partial z}wc >_{\Omega_e} - \ll \gamma\hat{c}(w_{\text{in}} - w_{\text{out}})c \gg_{\partial\Omega_e} \Bigg] \\ = \sum_{e=1}^{N_e}\Bigg[\ll \text{interface term} \gg_{\partial\Omega_e} - < \nabla_h \hat{c} \cdot (\kappa_h \nabla_h c) >_{\Omega_e} \\ - < \frac{\partial \hat{c}}{\partial z}\left(\kappa_v \frac{\partial c}{\partial z}\right) >_{\Omega_e} \Bigg]. \quad (1.37)$$

The interface terms for diffusion are detailed in Section 1.6.

As this is a transport equation, the interface fluxes need to be upwinded to ensure a stable discretization.

To ensure consistency, it is mandatory that the advection term degenerates to the incompressibility equation when a unit constant tracer is evolved (White *et al.*, 2008b). Therefore, one must use the same interpolation for both c and w. Indeed, u and w must follow the same definition as in the incompressibility equation. Further, the additionnal penalty term on w must be included.

1.3.6 Density & baroclinic pressure

It is well known that using some vertical coordinates (e.g. sigma coordinates) lead to an error in the computation of the baroclinic pressure gradient term in

the momentum equation (Haney, 1991). To partly circumvent this trouble, following Wang *et al.* (2008b), we compute the pressure gradient by integrating the density gradient:

$$\frac{\partial p}{\partial z} = -g\rho(T,S) \qquad \text{with} \qquad \rho = \rho_0 + \rho'(T,S) \tag{1.38}$$

becomes

$$\frac{\partial \nabla_h p}{\partial z} = -g\nabla_h \rho'(T,S) \tag{1.39}$$

as ρ_0 is constant. In the finite element discretization, we define a discrete vector field $\boldsymbol{F}_p$ that stands for the numerically computed baroclinic pressure gradient. The discrete formulation of the pressure gradient equation follows:

$$\sum_{e=1}^{N_e} \left[< \widehat{\boldsymbol{F}_p} \frac{\partial \boldsymbol{F}_p}{\partial z} >_{\Omega_e} \right] = \sum_{e=1}^{N_e} \left[- < g\widehat{\boldsymbol{F}_p} \nabla_h \rho'(T,S) >_{\Omega_e} \right]. \tag{1.40}$$

The tracer fields use discontinuous interpolation. Therefore, a component of their gradient is contained in the inter-element jumps. To take this jumps into account within the computation of the pressure gradient, we define the density deviation field ρ' as the L_2 projection of the function $EOS(T,S)$ onto a continuous finite element field. According to Table 1.2, the density deviation is then represented by continuous elements. The horizontal pressure gradient is also continuous, so that the pressure forcing term of the momentum equation (1.26) is continuous. Figure 1.1, with a simulation of a light water column inside denser water, shows that a continuous baroclinic pressure gradient avoids the apparition of noise in the velocity field. The pressure gradient equation must be integrated from top to bottom. To obtain a stable discretization of this equation, we must introduce some kind of upwinding. As we use for this equation a continuous interpolation, we resort to a Petrov-Galerkin approach, with upwinded test functions, that are the Cartesian product of usual triangular P_1 continuous test function and vertical linear upwinded L_1 shape function whose value is equal to one in the element above the corresponding node and zero elsewhere.

1.3.7 Moving mesh & ALE methods

The variation of the sea surface elevation modify the domain of integration. To ensure consistency, this volume modification must be taken into account (White *et al.*, 2008b). By working on a fixed mesh, three kind of errors appears:

- Conservation and consistency errors
- Biased weighting as the volume of the cells is modified
- Biased spatial operators

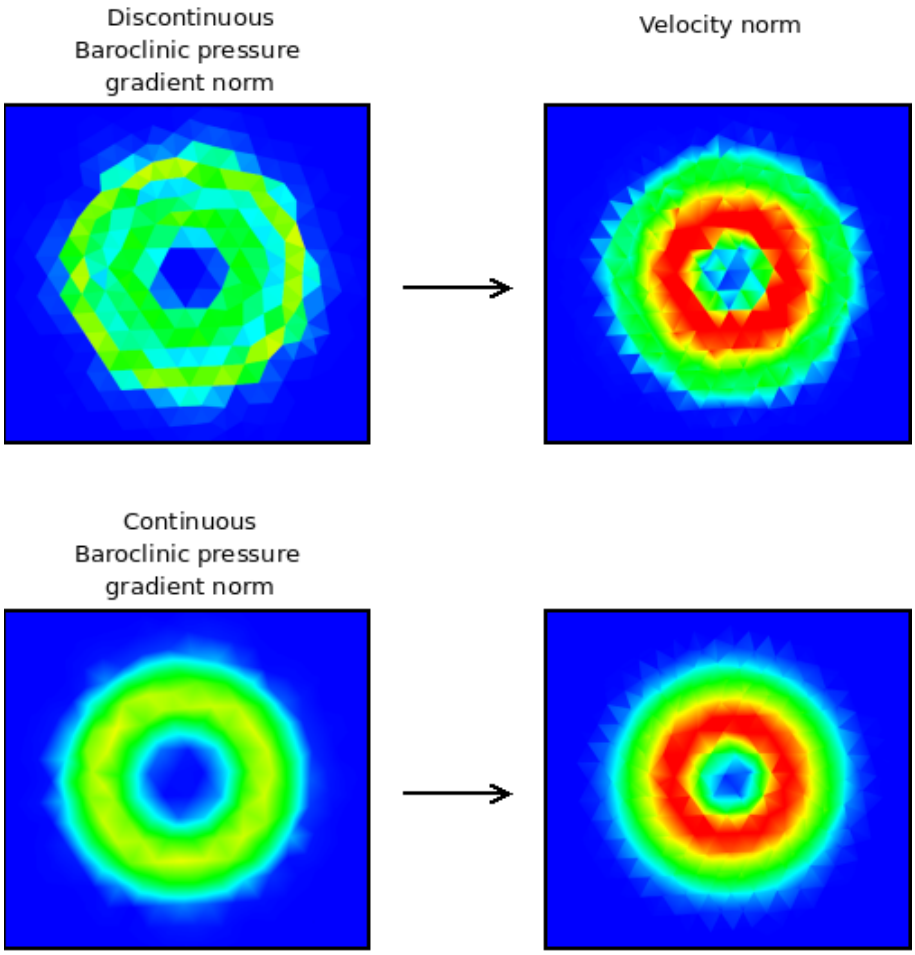

Figure 1.1: Effect of a continuous horizontal baroclinic pressure gradient on the velocity field. Column of light water in denser water.

For ocean modelling, where a wide spectrum of scales is parameterized, and where the free-surface oscillations are small compared to the depth, the two latter errors can be accepted. However, consistency errors must be avoided. Consistency can be ensured by extracting in the right way the temporal derivative of the mass term from the spatial integral on the moving domain which, in a conservative form, leads to the modified mass term:

$$< \hat{c}\frac{\partial c}{\partial t} >_{\Omega_e(t)} = \frac{\partial}{\partial t} < \hat{c}c >_{\Omega_e^{\text{fixed}}} + < \hat{c}c\frac{w_{\text{mesh}}^{\text{surface}}}{h} >_{\Omega_e^{\text{fixed}}} - < \hat{c}\frac{\partial (cw_{\text{mesh}})}{\partial z'} >_{\Omega_e^{\text{fixed}}}, \quad (1.41)$$

where w_{mesh} and $w_{\text{mesh}}^{\text{surface}}$ are respectively the vertical velocity of the computational domain, and its value at the sea surface. This relation is obtained by neglecting the bias on weighting and spatial operators. The last term of (1.41) is acting as an advection term, which correspond to substract the mesh velocity from the vertical advection term of (1.36). The other term can be viewed as a correction to the volume modification introduced by the movement of the moving mesh.

1.4 Boundary conditions

As explained in Section 1.1, the momentum equation degenerates to an hyperbolic equation when the horizontal viscosity disappears. Rousseau (2005) and Oliger and Sundstrm (1978) demonstrated with a modal analysis that, if no viscosity is considered, the hydrostatic equations are not well-posed for any set of boundary conditions of local type. For usual viscosity values, if impermeability is imposed at the boundary, a viscous boundary layer is generated, which is generally much smaller than the element size. This boundary layer for the horizontal velocity generates a strong vertical velocity to recover the incompressibility. This high vertical velocity induces stability problems, that are usually alleviated using limiting. However, we propose an alternative approach, that circumvent completely this problem. We only impose impermeability for the two-dimensional mean problem (i.e. for $\boldsymbol{U}$). We allow a vertical profile of horizontal velocity whose mean is nil at the boundaries. We let the momentum go out of the domain, mimicking the dissipation in the boundary layer, as in the hydrostatic equations, no momentum can be transfered to the vertical component of the velocity. For tracer equations, in order to ensure conservation and consistency, we define a two-dimensional mean value of the tracer at the external side of the boundary, so that the mean advection flux cancels out. This models an infinite vertical diffusivity in the boundary layer, which takes into account upwelling or downwelling that appears due to the boundary layer.

The bottom boundary needs a specific treatment. Physically, a no-slip boundary condition should be enforced ($\mathbf{u} = w = 0$). As the bottom veloc-

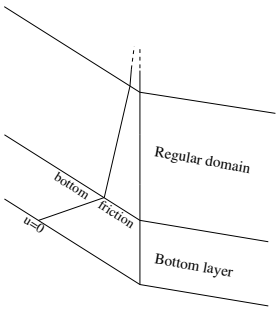

Figure 1.2: Additional layer of elements to handle the bottom boundary layer. The bold line shows a typical velocity profile. Note that, in a real application, the height of the bottom layer is much smaller than the mean elements height.

ity presents a logarithmic boundary layer whose characteristic length is often much smaller than the mesh size (Hanert *et al.*, 2007), it is often parameterised using a bottom stress τ derived from the law of the wall (Black and Gay, 1987):

$$\frac{\tau}{\rho_0} = \left[\nu_v \frac{\partial \mathbf{u}}{\partial z}\right]_{z=-h} = \left[\frac{\kappa}{\ln\left(\frac{z_b+h}{z_0}\right)}\right]^2 \|\mathbf{u}_b\|\mathbf{u}_b \tag{1.42}$$

where z_0 is the bottom roughness length and $\kappa = 0.4$ is the von Karman constant. The bottom velocity $\mathbf{u}_b$ is computed at a chosen distance from the sea bed $d = z_b + h$, which should be in the logarithmic boundary layer, typically the mid-height of the bottommost cell. The continuity equation being upwinded from the bottom to the top to obtain the vertical velocity, one needs to upwind w from the bottom boundary. Its value is choosen to avoid the flow to cross the bottom boundary:

$$[w]_{z=-h} = -\left[\mathbf{u} \cdot \nabla h\right]_{z=-h}. \tag{1.43}$$

However, (1.43) is imposed by specifying an exterior value for the upwinding of w. It is then only weakly enforced. This allows flows through the bottom boundary, which break tracers consistency and conservation. On the other hand, imposing strongly the bottom vertical velocity generates, according to (1.43), jumps between each elements whose bottom slopes are different. These jumps can be important and alter the solution.

A solution to overcome this issue is to impose strictly the no-slip condition at the bottom. Extended finite elements could be used to represent the boundary layer (Hanert *et al.*, 2007), but it would be complex to handle. Another method is to add an additionnal layer of elements at the bottom, much smaller than the mean elements height (Figure 1.2). We enforce the no-slip condition on the lower side of this layer, while the classical bottom friction

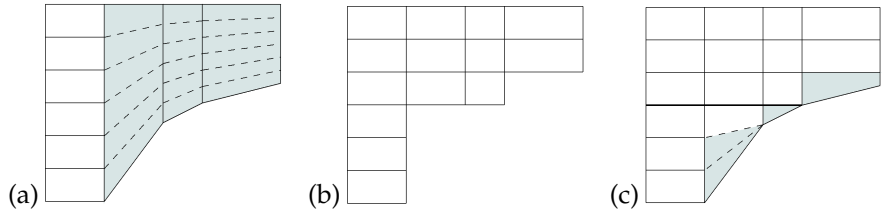

Figure 1.3: Different vertical coordinates systems implemented in the code: classical σ cordinates (a), classical z coordinates (b) and shaved cells (c)

(1.42) is applied on the lower side of the bottommost element above the additionnal layer. In this layer, a linear profile connects the no-slip bottom condition with the velocity in the upper element. This layer has no influence on the velocity in the above layers and, as the momentum equation is not computed in it, it doesn't add any limitation on the time step. Vertical velocity is then computed on the whole domain, even in the bottom layer, to ensure incompressibility. The Dirichlet boundary condition for vertical velocity is imposed weakly, i.e. the boundary term is omitted.

1.5 Vertical coordinates and their impact

Three different vertical coordinates systems are implemented in the model (Figure 1.3). Sigma coordinates offer an accurate representation of the bathymetry, which prevents the apparition of excessive vorticity and mixing, compared to z coordinates. However, in the presence of highly anisotropic operators whose orientation is mainly horizontal (diffusion, baroclinic pressure forcing), little errors in the computation of horizontal gradients, generated by the inclination of the cells, can alter significantly the solution. Two main problems are the pressure gradient error (Haney, 1991), and the spurious vertical diffusion (Huang and Spaulding, 1996). While the first issue is partially avoided for a linear density (Section 1.3.6), the spurious vertical diffusion remains a problem. Under certain conditions developed below, shaved cells introduced by Adcroft *et al.* (1997), offer the combined advantages of σ and z coordinates (i.e. they do not generate vorticity and, except in the bottommost cells, the horizontal gradients are exactly computed for a fluid stratified in the z direction).

A simulation of a flow over a seamount was run to compare the additional vorticity generated by the choice of vertical coordinates (Figure 1.4). The domain is $1000\ km$ long (x-direction) and its depth varies from $100\ m$ to $1000\ m$. It is infinitely long (periodic) in the y-direction.

The steady velocity of maximum $0.5\ m/s$ is induced by different elevations imposed at the left and right boundaries of the domain. The vorticity,

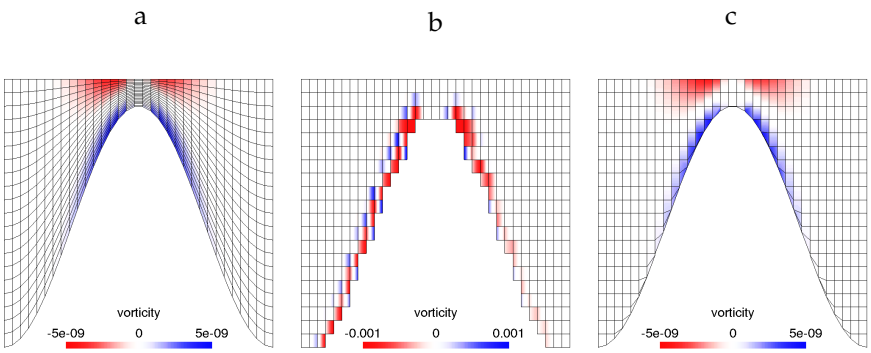

Figure 1.4: Vorticity of a steady state flow over a seamount, computed using classical σ cordinates (a), classical z coordinates (b) and shaved cells (c).

computed in the $x - z$ plane, is defined by

$$\zeta = \frac{\partial w}{\partial x} - \frac{\partial u}{\partial z}. \tag{1.44}$$

Figure 1.4 shows that σ coordinates and shaved cells generate a small vorticity, due to the deviation of the flow around the seamount, while z coordinates induce a strong vorticity. Generated by the staircase representation of the bottom, this strong vorticity is clearly not physical.

The same domain was used with a new setup to emphasize the spurious diffusion generated by the vertical discretization. A stratified tracer is initially set over the left slope of the seamount (Figure 1.5). Its concentration is zero for a depth under $400\ m$, has no horizontal structure, and is a quadratic function of depth. The fluid is at rest. A horizontal diffusion coefficient of $\kappa_h = 100\ m^2/s$ is used, while there is no vertical diffusion. Once a steady state is reached, the tracer concentration using σ coordinates is highly diffused in the vertical direction (Figure 1.5a). The remaining tracer concentration over the left slope of the seamount is less than half of its initial value, and some tracer has climbed the mount to reach the right part of the domain. The quadratic structure of the tracer concentration induced errors in the computation of horizontal gradients in inclinated cells (grey elements in Figure 1.3a) and interfaces (dashed lines in Figure 1.3a), generating spurious vertical diffusion. This diffusion is active until a linear vertical profile of tracer concentration is obtained. Then, the gradient computation errors disappear. With z coordinates, the horizontal gradient is exactly zero, and the steady state solution is the same as its initial concentration (Figure 1.5b). When shaved cells are used, the steady state solution is linear by part (Figure 1.5c). The spurious diffusion propagates along the bottommost cells and interfaces, which are the

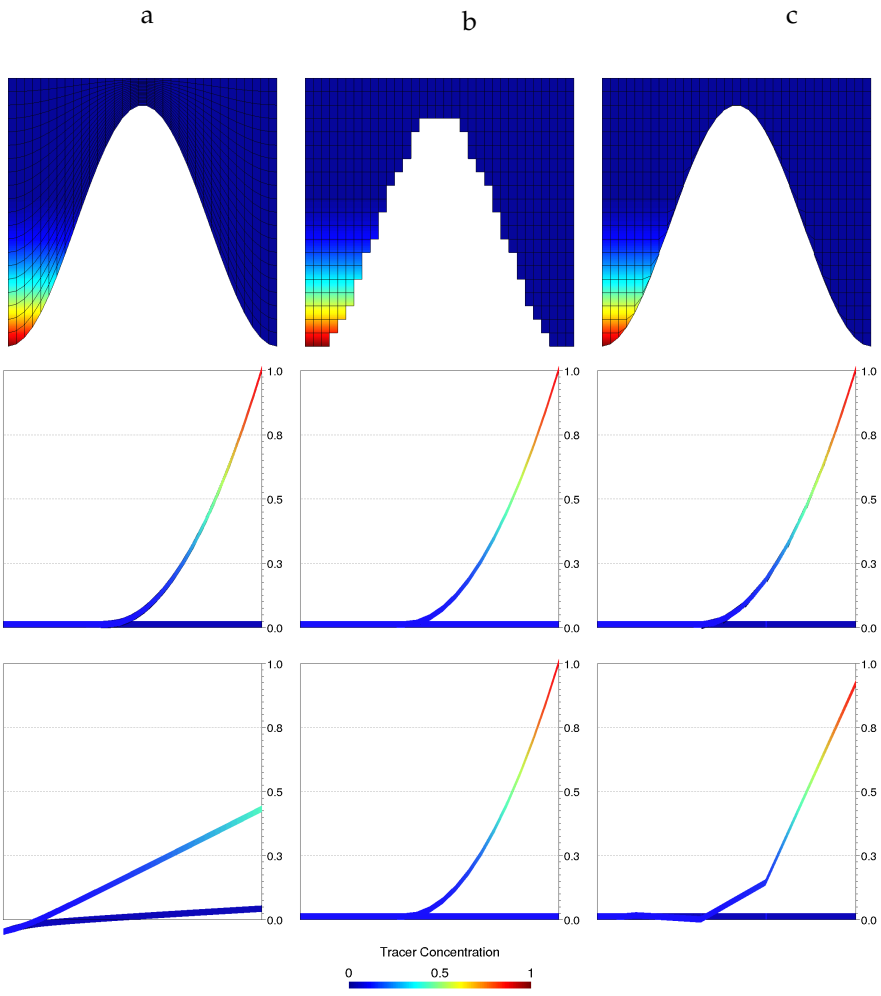

Figure 1.5: Stratified tracer in a fluid at rest, computed using classical σ cordinates (a), classical z coordinates (b) and shaved cells (c). Initial condition (up and middle) and steady state solution when applying horizontal diffusion (down). The last two rows of graphs show the tracer concentration at each side of the slope.

only elements subject to errors of the horizontal gradient. This propagation is stopped when discrete levels and horizontal elements boundaries intersect exactly at the sea bottom (e.g. the bold line in Figure 1.3c). However, this configuration is unlikely to appear in a realistic three-dimensional domain, and the same drawbacks as those associated with σ coordinates may appear (with a higher characteristic time however). This problem can be avoided by vanishing the horizontal diffusion flux through inclinated interfaces (dashed lines in Figure 1.3c). Doing that, diffusion can not propagates through different levels, and the steady state concentration is very close to its initial state.

Shaved cells seem to be an appropriate choice for ocean simulations. However, the choice of the vertical coordinates depends on the applications and must be studied for each different configuration.

1.6 Treatment of anisotropic diffusion with interior penalty method

1.6.1 Interior penalty methods

Using Discontinuous Galerkin methods, there are mainly two ways to treat the Laplacian operator. The local-DG approach (Cockburn and Shu, 1998a), that introduces a mixed formulation for the field and its gradient and can be difficult to handle with an implicit time-stepping, and the interior penalty family of methods (Arnold *et al.*, 2002a; Riviere, 2008).

It can easily be seen that the intuitive treatment of the Laplacian operator lacks convergence. Integrating by part, one gets:

$$< \hat{c}\nabla^2 c >_{\Omega_e} = \ll \hat{c}(\nabla c)^* \cdot \boldsymbol{n} \gg_{\partial\Omega_e} - < \nabla\hat{c} \cdot \nabla c >_{\Omega_e}, \tag{1.45}$$

where $(\nabla c)^*$ is the mean of the gradients at the two sides of the interface.

This formulation does not take into account the component of the gradient embedded in the inter-elements jumps. If the values in a whole element are shifted, the residual remains the same. Further, even if the Laplacian operator is symmetric, this formulation is not. To solve the problem, we use the symmetric interior penalty method (SIPG). It alleviates both of these troubles and can be written as follows:

$$\begin{aligned} \ll \hat{c}\frac{\nabla c_{\text{in}} + \nabla c_{\text{out}}}{2} \cdot \boldsymbol{n} \gg_{\partial\Omega_e} + \ll \nabla\hat{c}\frac{c_{\text{in}} - c_{\text{out}}}{2} \cdot \boldsymbol{n} \gg_{\partial\Omega_e} \\ + \ll \sigma\hat{c}(c_{\text{in}} - c_{\text{out}}) \gg_{\partial\Omega_e} - < \nabla\hat{c} \cdot \nabla c >_{\Omega_e} . \end{aligned} \tag{1.46}$$

Notice the penalty term, with the associated parameter σ. It allows the formulation to take into account the component of the gradient embedded in the jumps. There is a lower bound on σ that ensures optimal convergence, and this bound must be as tight as possible, as the higher σ, the worser the

conditioning of the operator. Shahbazi (2005) provides good values of σ as:

$$\sigma = \max_e \left[\frac{(k+1)(k+d)}{d} \frac{A(\text{interface})}{V(\Omega_e)} \right], \tag{1.47}$$

where d is the spatial dimension, and k the order of the interpolation.

1.6.2 Anisotropy of the operator

Solving anisotropic diffusion is not an easy problem. Indeed, it is really difficult to ensure that the discrete anisotropic diffusion satisfy a discrete maximum principle (Kuzmin *et al.*, 2009). However, in ocean modelling, both the diffusion operator and the mesh are anisotropic. We propose to mentally stretch the mesh in the vertical direction so that we recover an isotropic diffusion on the stretched mesh. The mesh is not really stretched, but interior penalty coefficients are chosen is such a way that they correspond to an isotropic diffusion on a stretched mesh.

Let us consider a general large scale tracer problem, on a mesh whose typical horizontal and vertical elements sizes are 100 km and 10 m. Considering unresolved phenomena for this mesh scale, typical values of turbulent diffusivity in the ocean interior are of the order $\kappa_h = 10^4\ m^2 s^{-1}$ and $\kappa_v = 10^{-4}\ m^2 s^{-1}$ (Griffies, 2004; Ledwell *et al.*, 1993; Mellor and Blumberg, 1985). The dimensionless equivalent problem with a vertical diffusivity $\kappa_v = 10^4\ m^2 s^{-1}$ corresponds to a mesh stretched by a factor 10^4 in the vertical direction. In such a mesh, the typical vertical mesh size would be $100\ km$. So we recover isotropic diffusion on an isotropic mesh. The values taken here are more or less representative of the order of magnitude found in an ocean model, and illustrate that the anisotropy of the problem is rather small.

However, this is strongly related to the hydrostatic consistency of Haney (1991), as if the elements are too shallow, the stretched grid is highly distorted, as illustrated in Figure 1.6.

1.7 Density driven flow

The model is now applied to different typical ocean modelling benchmarks to check that it reproduces a correct physical behaviour of the fluid. These simulations do not validate the model, as we focus mainly on the qualitative behaviour. The model is still in validation and some quantitative comparisons need to be done.

The first testcase is a baroclinic and rotational benchmark developed by Avlesen *et al.* (2001). It was designed to be "a test problem complex enough to measure fundamental qualities of numerical schemes in ocean models, but otherwise as simple as possible". The domain is a box of $200\ km \times 200\ km$, with closed boundaries. The horizontal coordinates x and y are equal to zero

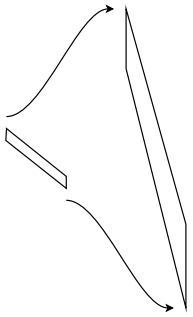

Figure 1.6: Dimensionless equivalent problem on stretched mesh leads to isotropic diffusion. The mesh is highly distorted as it does not respect the hydrostatic consistency principle.

at the center of the box. The mean water depth is $200\ m$. If we define the two metrics

$$r_h = \sqrt{(x-10^5)^2 + (y-10^5)^2} \qquad \text{and} \qquad r_v = 1000z, \tag{1.48}$$

where x and y are the horizontal coordinates in metres, the initial density is given by

$$\rho_h(x,y) = \rho_c - \Delta\rho \tanh(r_h/\Delta r) \tag{1.49}$$

$$\rho(x,y,z) = \rho_h(x,y)(1 - \tanh(r_v/\Delta r)) + \rho_0 \tanh(r_v/\Delta r) \tag{1.50}$$

with $\rho_c = 1024\ kg/m^3$, $\Delta\rho = 4\ kg/m^3$ and $\Delta r = \sqrt{3}\cdot 5\cdot 10^4\ m$. The reference density is $\rho_0 = 1025\ kg/m^3$. The initial density deviation field is shown in Figure 1.7a. The initial free-surface is determined from (Avlesen *et al.*, 2001)

$$\frac{\partial \eta}{\partial x} = \frac{1}{\rho_0}\int_{-h}^{0} \frac{\partial \rho}{\partial x}\mathrm{d}z \qquad \text{and} \qquad \frac{\partial \eta}{\partial y} = \frac{1}{\rho_0}\int_{-h}^{0} \frac{\partial \rho}{\partial y}\mathrm{d}z, \tag{1.51}$$

assuming that the average of the elevation η over the domain is nil. The initial velocity obeys

$$f\frac{\partial u}{\partial z} = \frac{g}{\rho_0}\frac{\partial \rho}{\partial y} \qquad \text{and} \qquad f\frac{\partial v}{\partial z} = -\frac{g}{\rho_0}\frac{\partial \rho}{\partial x}. \tag{1.52}$$

with a bottom velocity $u_{\mathrm{btootm}} = v_{\mathrm{bottom}} = 0$.

Following Avlesen *et al.* (2001), the coriolis parameter is set to $f = 1.3\cdot 10^{-4}\ s^{-1}$. The bottom friction follows the relation (1.42) with a bottom roughness length $z_0 = 0.01\ m$. The vertical viscosity and diffusivity are $\nu_v = \kappa_v = 0.01\ m^2/s$, while the horizontal ones are $\nu_h = \kappa_h = 1\cdot 10^4\ m^2/s$. This test case is highly viscous. Avlesen *et al.* (2001) justified these high values of viscosity

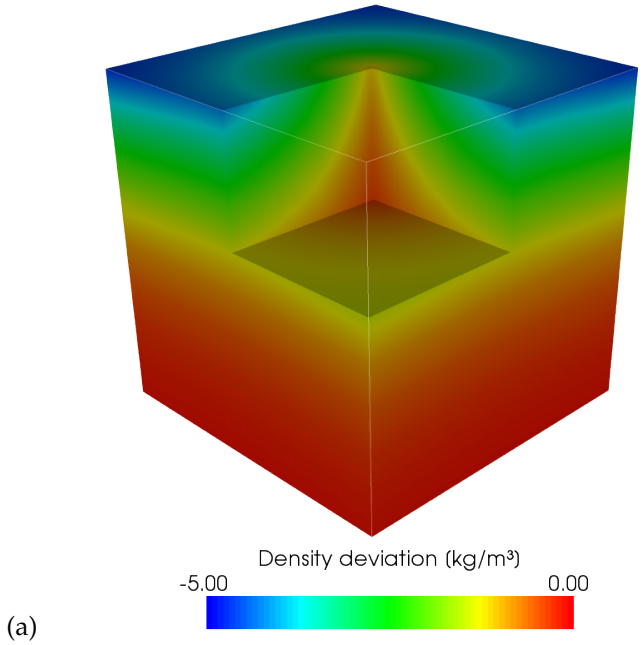

(a)

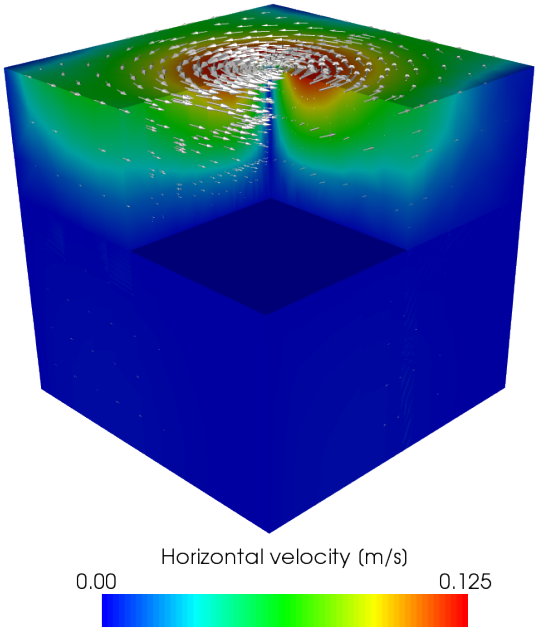

(b)

Figure 1.7: Initial density deviation (a) and steady-state horizontal velocity norm and direction obtained from the model on the diagnostic run (b).

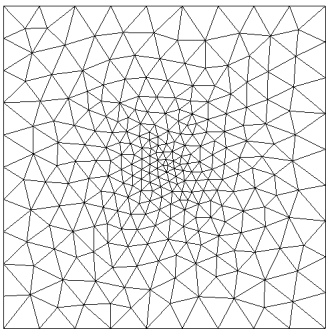

Figure 1.8: Two-dimensional mesh to be extruded for the simulation. It contains 531 triangles.

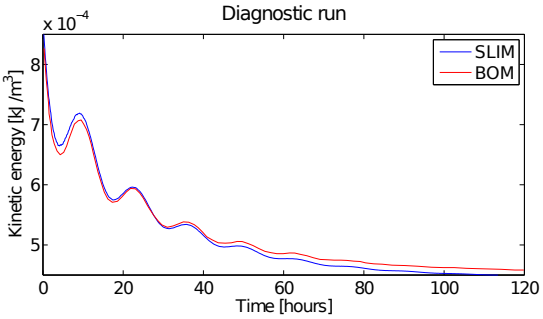

Figure 1.9: Evolution of the kinetic energy for the diagnostic run. SLIM results compared to a high-resolution finite-difference reference solution.

and diffusivity by the need to obtain a diagnostic in a short time on a modest computer. The norm of the acceleration due to the gravity is $g = 9.806\ m/s^2$.

The mesh is made of 531 triangles extruded over 8 layers to obtain 4248 prisms. Its two-dimensional part is refined near the center where the spatial variations of the variables are stronger (Figure 1.8). The model uses a time-step of 180 seconds. A first run is performed in diagnostic mode. The density is constant in time, and will act as a forcing term on the momentum equation. An equilibrium between pressure forcing and coriolis acceleration will develop to reach a stead-state regime. The norm and direction of the velocity in this steady-state regime are visible on Figure 1.7b. Figure 1.9 shows the

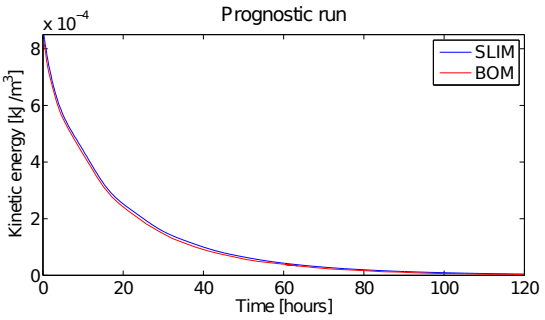

Figure 1.10: Evolution of the kinetic energy for the prognostic run. SLIM results compared to a high-resolution finite-difference reference solution.

evolution of the kinetic energy, computed using

$$\text{Kinetic energy} = \int \frac{1}{2}\rho(u^2 + v^2)d\Omega. \tag{1.53}$$

Oscillations of a period of approximately 15 hours are generated by an adjustement around an equilibrium state dictated by the constant density field (Avlesen *et al.*, 2001). A comparison is made with a reference finite-difference model (i.e. the Bergen Ocean Model (BOM)). The latter uses a higher resolution (345.600 cells). As it was designed without mode splitting, the time step, constraint by the surface gravity waves celerity, is set to 15 seconds. This comparison shows that the kinetic energy oscillations are obtained with correct amplitude and period, as well as the evolution towards the steady-state regime.

The second run is fully prognostic: the density is advected by the flow and subject to diffusion. Both density and velocity interact mutually. The kinetic energy is exponentially damped to be finally anihilated when no density gradient subsists due to the high dissipation (Figure 1.10). The comparison with BOM results also shows that this exponential decrease occurs at a correct rate.

1.8 The DOME test-case

In this section, the model is applied to the simulation of a density driven flow inspired by the common DOME test-case. DOME stands for Dynamics of Overflow Mixing and Entrainment. It is a benchmark setup designed to assess the qualities and drawbacks of ocean models in terms of deep water formation by gravity currents. The DOME test-case was the subject of many studies to understand the influence of vertical coordinates (Ezer and Mellor, 2004; Wang

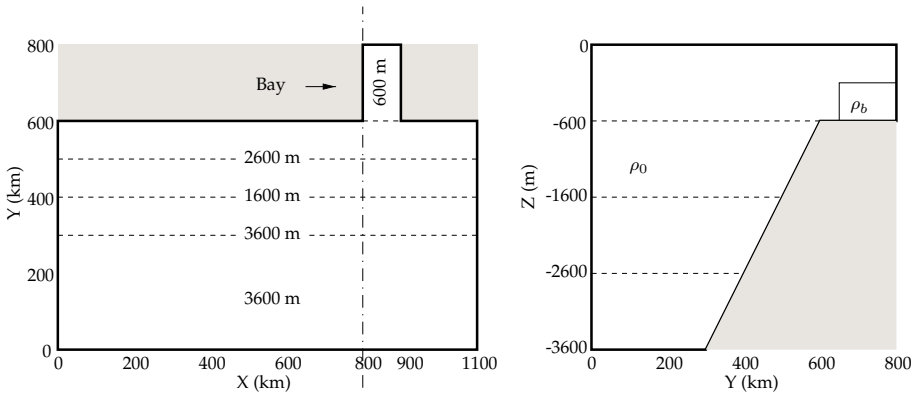

Figure 1.11: The computational domain for the DOME benchmark.

et al., 2008a), resolution and physical parameters (Legg *et al.*, 2006; Tseng and Dietrich, 2006; Jiang and Garwood, 1996), geometry (Ezer, 2006) or parameterisations (Ezer, 2005). In this section, we try to reproduce the qualitative behaviour observed in previous models or observations. The computational domain and initial setup is provided in Figure 1.11: dense water (density ρ_b) is initially set into the half lower part of the embayment of depth $600\ m$. Different values of the density are obtained by using a temperature field T that impacts on the density by the means of a linear equation of state (Cushman-Roisin, 1994):

$$\rho = \rho_0 \left(1 - \alpha(T - T_0)\right), \tag{1.54}$$

where $\alpha = 1.945525291 \cdot 10^{-4}\ (^\circ C)^{-1}$ and $\rho_0 = 1025\ kg/m^3$. As a simplification, the effect of salinity is neglected and the density is only a function of temperature. The reference temperature is not defined, but temperature deviation $T' = T - T_0$ is initially imposed at $T' = 0$ in the whole domain and $T' = -10\ ^\circ C$ in the embayment, leading respectively to densities of $1025\ kg/m^3$ and $1027 kg/m^3$.

Lateral boundaries are closed except the northern one (e.g. the end of the bay) where geostrophically balanced inflow conditions are imposed (Harig, 2004) with an incoming velocity of $v_{in} = 0.5\ m/s$ in the lower part and an opposed velocity in the upper part. The interface between the lower and upper parts of the boundary as well as the sea surface elevation are derived from the geostrophic equilibrium (Harig, 2004). Water enters in the domain with a temperature deviation of $T' = -10\ ^\circ C$, corresponding to its initial value in the lower part of the embayment.

The experiment is used here to check stability and good physical behaviour of the model with little explicit viscosity and little explicit diffusion on a relatively coarse mesh. The latter contains 53.244 prismatic elements distributed

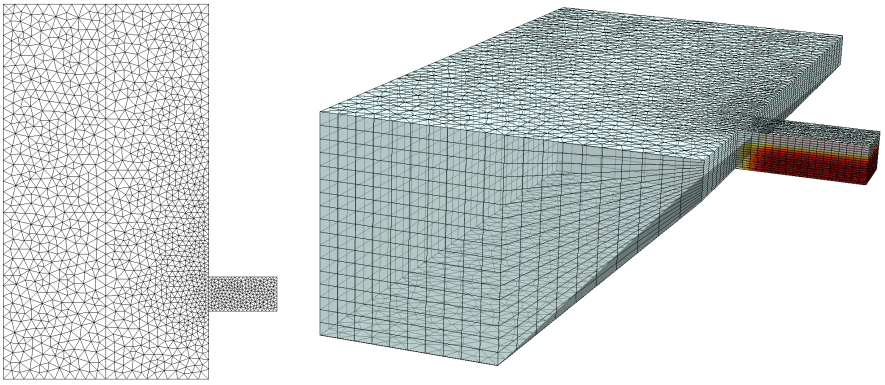

Figure 1.12: Unstructured grid used for the simulations, containing 53.244 prismatic elements generated with the extrusion of 2958 triangles to form 18 layers. Its horizontal resolution varies from $11\ km$ to $30\ km$. Initially dense water is placed in the red area for the experiment.

among 18 layers. Its horizontal resolution varies from $11\ km$ to $30\ km$ (Figure 1.12).

The horizontal turbulent viscosity ν_h is computed via a Smagorinsky scheme (Smagorinsky, 1963a):

$$\nu_h = c_s \Delta^2 \left[\left(\frac{\partial u}{\partial x} \right)^2 + 0.5 \left(\frac{\partial u}{\partial y} + \frac{\partial v}{\partial x} \right)^2 + \left(\frac{\partial v}{\partial y} \right)^2 \right]^{1/2} \tag{1.55}$$

where Δ^2 is the surface area of the local triangle (Akin *et al.*, 2003). The Smagorinsky constant c_s is set to 0.01 and the horizontal viscosity is constrained by a maximum value of $\nu_h \leq 50\ m^2/s$. A Pacanowski and Philander model (Pacanowski and Philander, 1981a) prescribes vertical viscosity in terms of a function of the Richardson number:

$$\nu_v = \frac{\nu_0}{(1 + \alpha Ri)^n} + \nu_b, \tag{1.56}$$

where n and $\alpha > 0$ are adjustable parameters, respectively set to 2 and 10 in the present study following Wang *et al.* (2008a). The neutral and background values of vertical viscosity are set to $\nu_0 = 5 \cdot 10^{-2}\ m^2/s$ and $\nu_b = 2 \cdot 10^{-5}\ m^2/s$. The Richardson number is defined by

$$Ri = \frac{N^2}{M^2}, \tag{1.57}$$

in which M and N are respectively the Prandtl and Brunt-Väisälä frequencies

$$M = \left|\frac{\partial \mathbf{u}}{\partial z}\right| \qquad \text{and} \qquad N = \sqrt{\frac{\partial b}{\partial z}}, \tag{1.58}$$

where $b = -g(\rho - \rho_0)/\rho_0$ is the buoyancy. If the Richardson number is negative, its value is taken to be zero. The horizontal diffusion coefficient is set to $\kappa_h = 10\ m^2/s$ while vertical diffusion coefficient is prescribed to $\kappa_v = 1 \cdot 10^{-4}\ m^2/s$. The choice of these viscosity/diffusion coefficients is somewhat artificial, and was made to obtain values comparables to previous studies using constant coefficients such as Wang *et al.* (2008a). As the flow is largely unresolved, a considerable numerical diffusion is generated by the model, and the effect of the turbulence parameterisations may not be dominant. Further studies should be performed to estimate the effect of the numerical diffusion versus the turbulence parameterisations, as proposed by Burchard and Rennau (2008).

Results of simulation are shown in Figure 1.13. A large plume develops along the slope and splits into several smaller subplumes, well defined after 10 days of simulation. Surface depressions and mean velocity show counter-rotating eddies whose genesis is clearly related to these subplumes. As the simulation evolves, the subplumes interact with each other to finally merge. Eddies propagate along the isobath with the shallow side on the right, corresponding to topographic Rossby waves (Cushman-Roisin, 1994). This behaviour was described in detail by (Jiang and Garwood, 1996) who performed similar simulations in a non-stratified domain.

To provide a comparison with previous models, Figure 1.14a shows the profile of temperature along a vertical line of coordinates $(x, y) = (700, 560)\ km$ after 40 days, obtained with the SLIM model. Figures 1.14b shows the profile of a tracer initially at 0 with a unitary value at the inflow boundary, obtained at the same location and same time by (Wang *et al.*, 2008a). The profile of density from Ezer and Mellor (2004) along the same line at the same time is visible on Figure 1.14c. The different variables (temperature, tracer concentration and density) are not of the same scale, but their profiles are characteristic of the shape of the plume and can be compared. According to (Ezer and Mellor, 2004; Wang *et al.*, 2008a), the thickness of the bottom plume is approximately $50 - 100\ m$. The shape of the plume is better described with the models of Wang *et al.* (2008a) and Ezer and Mellor (2004), particularly close to the bottom. This is a consequence of the lack of vertical resolution of the SLIM simulation, using 18 layers, while the others studies used respectively 36 and 50 layers. The thin bottom plume (the last $55\ m$ near the sea bottom) is represented with only one layer of prisms in the SLIM simulation, explaining that its profile is linear.

This simulations shows that the SLIM model is able to represent some physical processes encountered in the ocean. Such a coarse resolution does not allow to represent the complete structure of the flow, but its general behaviour is in accordance with the previous model studies.

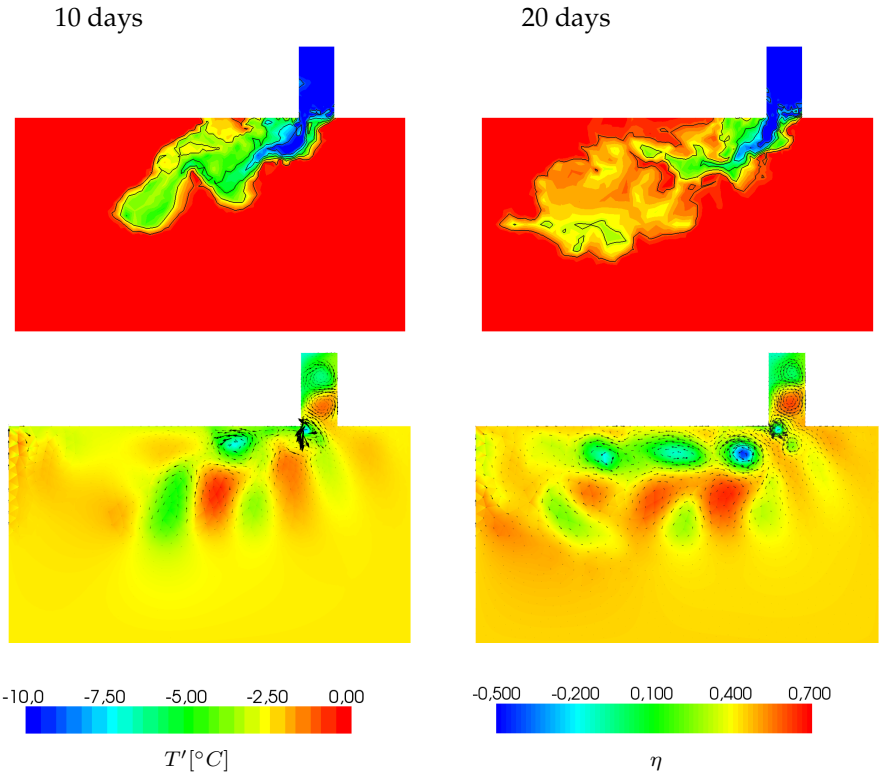
10 days
20 days
-10,0
-7,50
-5,00
-2,50
0,00
$T'[°C]$
-0,500
-0,200
0,100
0,400
0,700
η

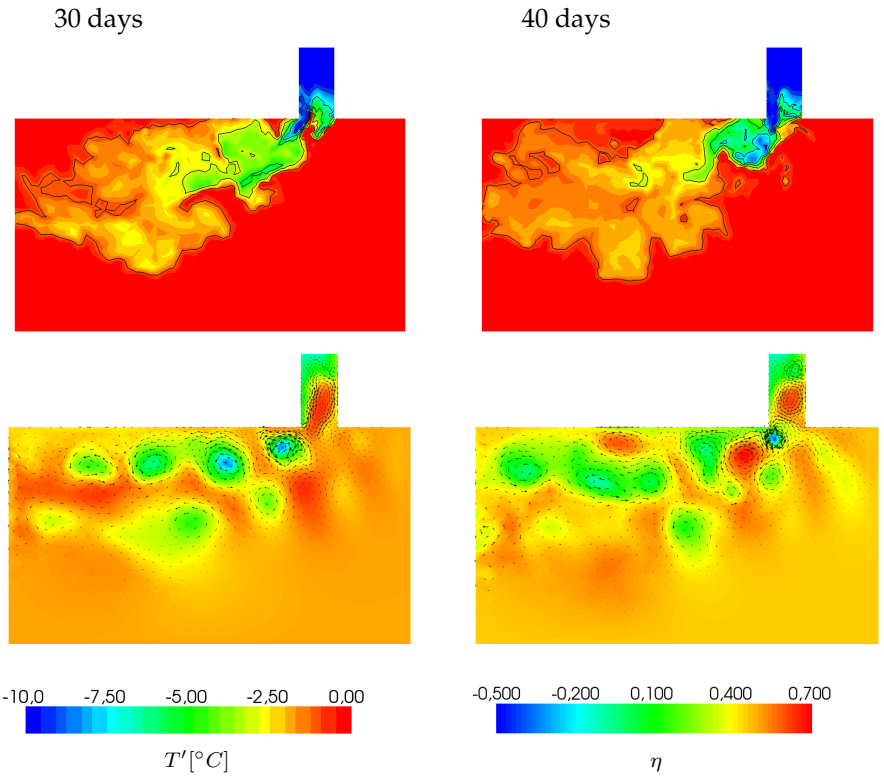

Figure 1.13: (UP) Temperature deviation just above the bottom. Isolines every $2^\circ C$. (DOWN) Free-surface elevation and direction of depth-averaged velocity.

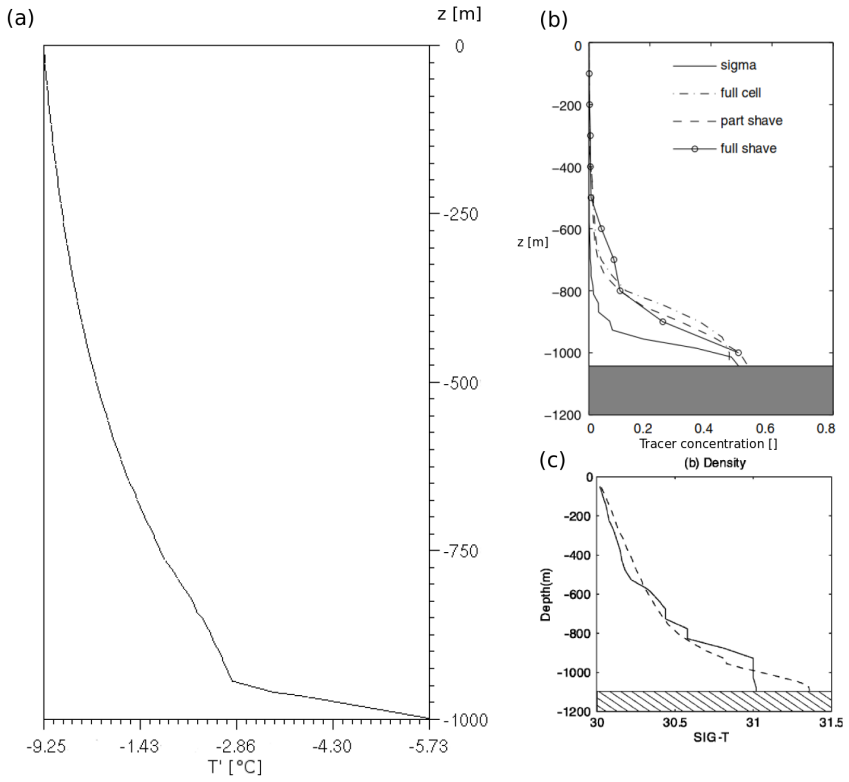

Figure 1.14: Profiles along a vertical line of coordinates $(x, y) = (700, 560)\ km$, after 40 days. (a) Temperature profile with the SLIM model. (b) Tracer concentration profile from Wang *et al.* (2008a) (horizontal resolution $10\ km$, 36 layers). (c) Density profile from (Ezer and Mellor, 2004) (horizontal resolution $10\ km$, 50 layers), in sigma-t units.

1.9 Baroclinic instability

The last benchmark is a baroclinic instability, modelled in laboratory by Griffiths and Linden (1981) and simulated with three-dimensional models by James (1996) and Tartinville *et al.* (1998). It consists of an initial cylinder of water of lower salinity than the ambient sea water. This cylinder extends on the half upper layer of the domain. An eddy forms which, after an adjustment period, develops a second order instability and splits into two smaller eddies (Griffiths and Linden, 1981). The domain of interest is a square box of depth $20\ m$ and length $30\ km$ with open boundaries. Tartinville *et al.* (1998) and James (1996) used sponge regions to approximate open boundaries. In this study, the mesh flexibility of the finite element method is used to move the boundaries far enough from the region of interest to limit their influence. The resulting two-dimensional mesh of 3742 triangles has a resolution varying from $1\ km$ to $100\ km$ (Figure 1.15). This mesh is extruded in the vertical direction to obtain 18 layers.

The initial salinity is a function of the distance to the center d, given by

$$S = \min\left[1.1\left(\frac{d}{3000}\right)^8 + 33.75\ ,\ 34.85\right]. \tag{1.59}$$

The equation of state is linearised following

$$\rho = 1025 + 0.78(S - 33.75). \tag{1.60}$$

The coriolis parameter is set to $f = 1.15 \cdot 10^{-4}\ s^{-1}$. Initial velocity and elevation are set to zero. No bottom or surface stress is considered. Constant diffusivities are used, respectively $1\ m^2/s$ in the horizontal direction, and $5 \cdot 10^{-5}\ m^2/s$ in the vertical direction. The horizontal viscosity is computed via a Smagorinsky scheme (Equation 1.55) using a coefficient $c_s = 0.06$ while the vertical viscosity is set to $1 \cdot 10^{-4}\ m^2/s$. The values of horizontal viscosity are modified to respect the constraint $0.5\ m^2/s \leq \nu_h \leq 5\ m^2/s$. These values were chosen the smallest possible but high enough to provide a stable discretization.

The evolution of density, mean velocity and sea surface elevation is shown in Figure 1.16. Gravity waves are quickly generated, propagating radially out of the domain of interest. Then, the eddy oscillates around a geostrophic equilibrium. Finally, the mode 2 instability develops as expected, and the vortex breaks into two smaller vortices.

The evolution of kinetic energy (Equation 1.53) and enstrophy, defined as the square of the horizontal vorticity

$$\text{Enstrophy} = \int \left(\frac{\partial v}{\partial x} - \frac{\partial u}{\partial y}\right)^2 d\Omega \tag{1.61}$$

is sketch in figure 1.17. We observe inertial oscillations of a period of approximately 15 hours, linked to the eddy oscillations visible in the three first shots

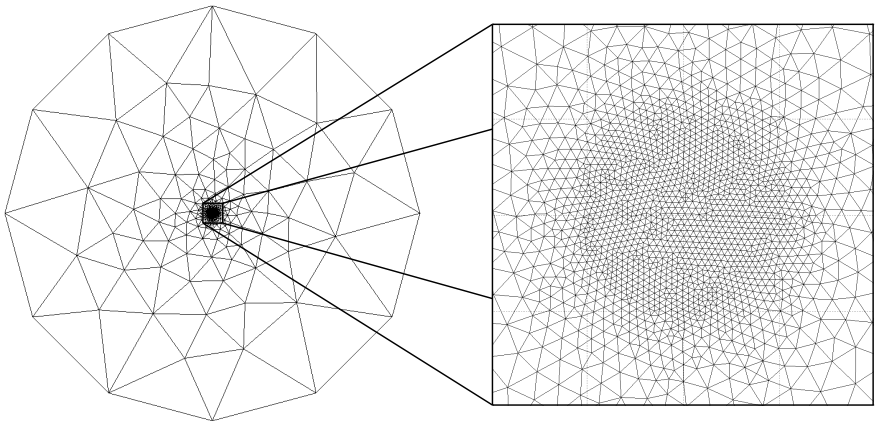

Figure 1.15: Unstructured two-dimensional mesh used for the benchmark simulations. It contains 3742 triangles and its resolution varies from $1\ km$ to $100\ km$. The size of the box on the right panel is $60\ \times\ 60\ km$.

of Figure 1.16, corresponding to simulation times of $30\ min$, $8\ h$ and $15\ h$. Both kinetic energy and enstrophy starts to increase after about 150 hours, when the vortex break up in two smaller vortices. The values of the diagnostics evolve in the same range as the results obtained by Tartinville *et al.* (1998) using different finite-difference models.

As some models were unable to obtain a mode 2 instability, it should be interesting to perform a mathematical analysis to ensure that this mode 2 instability is really the lowest energy mode. However, such a study is not in the framework of the present work. Laboratoty experiments observed a mode 2 instability, and it it seems that the apparition of this mode is not very sensible to small perturbations of the initial conditions. According to Griffiths and Linden (1981), the order of the instability depends on the initial characteristics of the cylinder. After several laboratory experiments, Griffiths and Linden (1981) were able to provide a map of the mode of the instability as a function of two initial parameters: the relative height of the light water cylinder δ and a Richardson number

$$\theta = \frac{g\frac{(\rho-\rho_{\text{ref}})}{\rho_{\text{ref}}}20\delta}{f^2R^2} \tag{1.62}$$

where ρ_{ref} is the density at 34.85 PSU and R is the radius of the cylinder of light water. On this map (Figure 1.18), the simulation performed with the SLIM model (X mark on the plot) should clearly produce a second order instability, even if the parameters change slightly. Futhermore, by decreasing the height of the light water cylinder δ, the order of the unstable mode produced by the SLIM model increased as expected in Figure 1.18 (not shown).

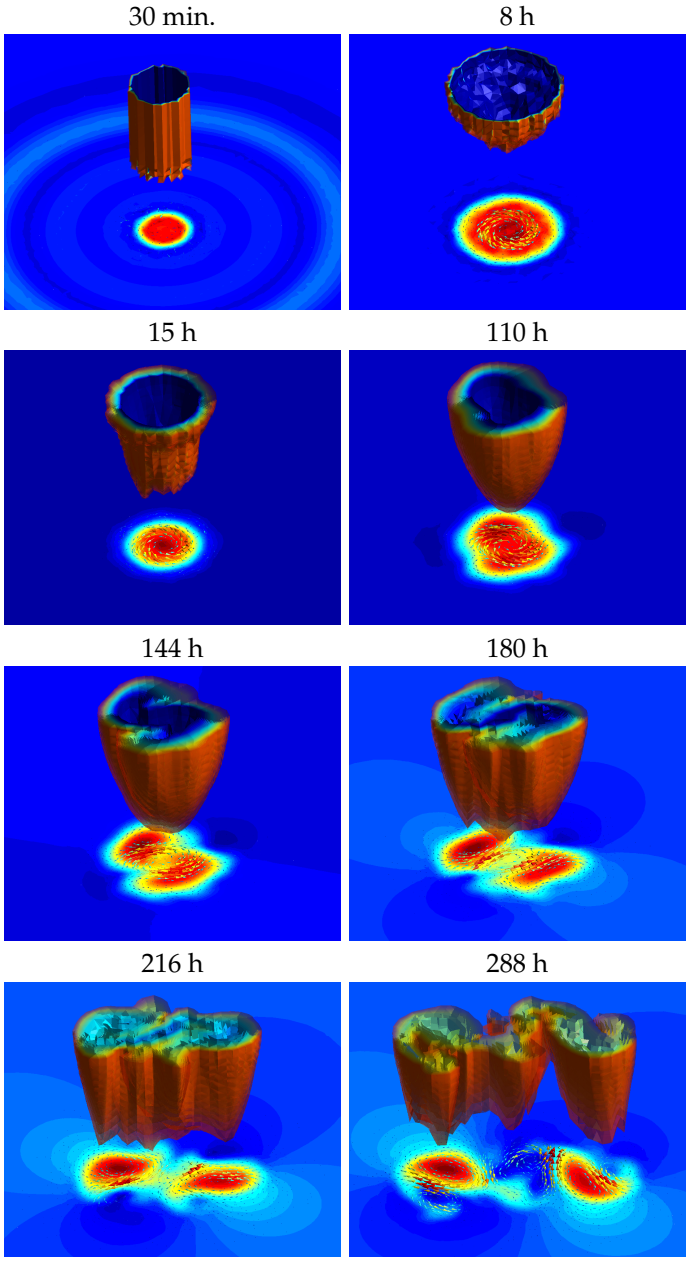

Figure 1.16: Illustration of the baroclinic instability testcase. At the bottom of the domain, we show the sea-surface elevation, the arrows representing the two dimensional mean velocities. Isocontours of the salinity are given, ranging in $[34.5, 34.7875]$ PSU and separated by 0.0125 PSU.

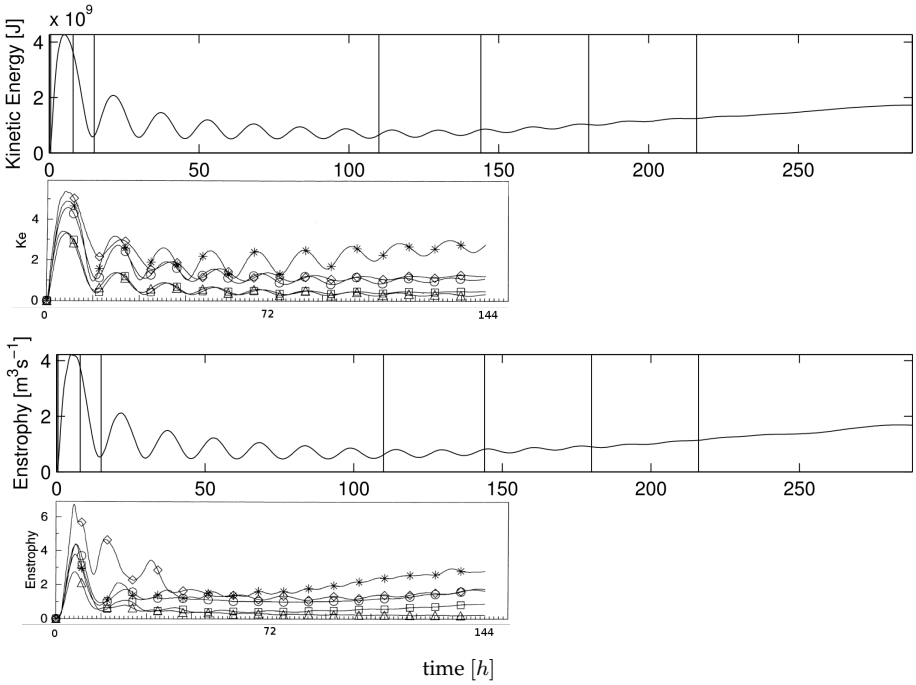

Figure 1.17: Evolution of the kinetic energy and enstrophy. SLIM results (UP) versus results from Tartinville *et al.* (1998) obtained with different models (DOWN). The vertical lines denote times where the snapshots of Figure 1.16 were taken.

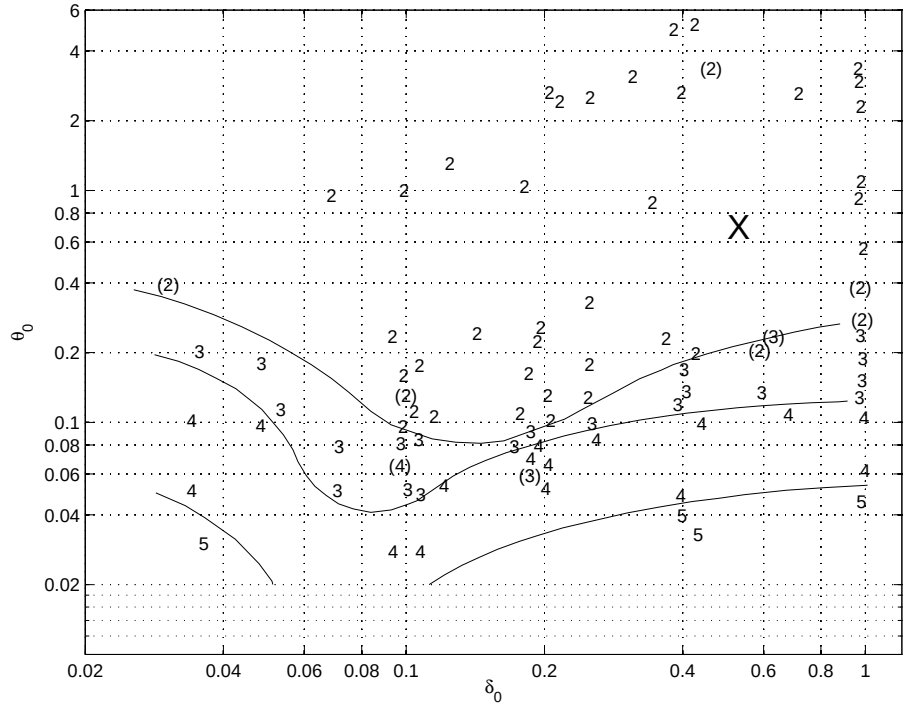

Figure 1.18: Map of order of the unstable mode, depending on the initial δ and θ, from Griffiths and Linden (1981). The value of the parameters corresponding to the current experiment with the SLIM model is represented with the X mark.

Following laboratory experiments from Griffiths and Linden (1981), the mode 2 instability should appear in numerical simulations. In his model intercomparison, Tartinville *et al.* (1998) interpreted that a too high numerical viscosity related to the advection scheme had the effect of producing an order 4 instability rather than the expected mode 2, explaining the discrepancy between models.

1.10 Discussion

These testcases show that the model is able to represent the expected physical behaviour in different configurations, specifically designed to evaluate ocean models. More analysis and sensitivity studies should be performed to complete the validation and have a better understanding of the model behaviour. Then, simulations have to be made on realistical configurations. The model is

still in developments stage, and should be optimized when its core characteristics will be definitively decided.

Our Discontinuous Galerkin advection scheme is little diffusive; but it has the drawback of producing over- and under-shoots when the advected field is too sharp. They are not a problem for some applications, but can become critical when reaction terms influe on the considered variables and do not have a specific treatment taking into account these overshoots (e.g. biological variables,...). Slope limiters can be used to prevent overshoots to appear (Cockburn and Shu, 1998b) but will inevitably introduce additional diffusion.

Chapter 2

Boundary layers: representation or parameterisation?

This chapter is devoted to the treatment of some boundary layers. Several types of boundary layers exist in marine systems. They can be related to lateral boundaries, sea bottom or surface. The characteristic lengths corresponding to these boundary layers are generally much smaller than the ones corresponding to the mean flow. Due to that, the computational mesh is often too coarse to be able to represent the boundary layers with classical numerical methods. Even though their exact representation can be not important for the modeller, their effect on the mean flow must be taken into account. Three solutions are then possible to handle these boundary layers:

- Refine the mesh in the proximity of the boundary layer to be able to represent it
- Use specific representation methods adapted to the type of boundary layer
- Parameterise the boundary layer

The first solution requires a very fine mesh near the boundary. While it is used in engineering (Sahni *et al.*, 2008), this method remains expensive for geophysical simulations. The second solution tries to represent the boundary layer without increasing significantly the computational cost. Although impossible to perform in finite differences, this solution is easier to implement using finite elements due to their functional flexibility, i.e. the ability to use different types of shape functions to represent the model variables (Hanert *et al.*, 2007). However, its use is subject to the knowledge of the behaviour of the boundary layer and cannot always be applied. The last solution does not represent

the boundary layer but takes its effect into account, usually by imposing specific boundary conditions derived from an idealised analytical solution. This method does not involve significant additional computational cost, but the parameterisation must reflect the behaviour of the boundary layer. Furthermore, it is not possible to know the state of the variables inside the boundary layer. In the next sections, the two last solutions (specific representation method and parameterisation) will be used and developed for the treatment of two specific boundary layers: the ocean logarithmic bottom boundary layer and the residence time inflow boundary layer. The advantages and inconvenients of each solution will be discussed.

2.1 Ocean bottom logarithmic boundary layer

The ocean bottom logarithmic boundary layer is a well known phenomenon, parameterised in most marine models (Blumberg and Mellor, 1987; Deleersnijder *et al.*, 1992; Davies *et al.*, 1995b; White and Deleersnijder, 2007). This section shows the possibility to represent this boundary layer using the extended finite elements method.

In non-rotating marine waters, the velocity of the fluid near the bottom is described by a logarithmic law which can be written as (Burchard, 2002a)

$$u(z) = \frac{u_*}{\kappa}\ln(\frac{z_b + z_0}{z_0}), \tag{2.1}$$

where u, κ, z and z_0 are respectively the horizontal velocity of the fluid, the von Karman constant ($\kappa = 0.4$), the vertical coordinate pointing upwards with its origin at the sea surface and the bottom roughness length. $u_* = \sqrt{\tau/\rho}$ is the bottom friction velocity where τ is the bottom stress, and $z_b = z + h$ is the distance from the bottom. A scalar velocity and a constant water depth h are considered for simplicity. Classical numerical methods are not able to represent such a logarithmic profile without increasing significantly the mesh resolution. Parameterisations were developed, derived from the law of the wall whose most popular consists in estimating a bottom stress as a quadratic function of the bottom velocity (Equation 1.42).

If one needs to know the behaviour of the model variables near the bottom, the boundary layer must be represented. Starting from (2.1), the extended finite element method can be used to handle the bottom boundary layer, because (2.1) is constant in time up to a multiplicative factor u_*. The idea is to use additional shape functions in the functional basis used for the representation of the solution (Figure 2.1). Using this method, the velocity can be approximated by

$$u^h = \sum_{j=1}^{N} u_j \Phi_j(z) + \sum_{j=1}^{N_X} b_j \Phi_j(z) F(z), \tag{2.2}$$

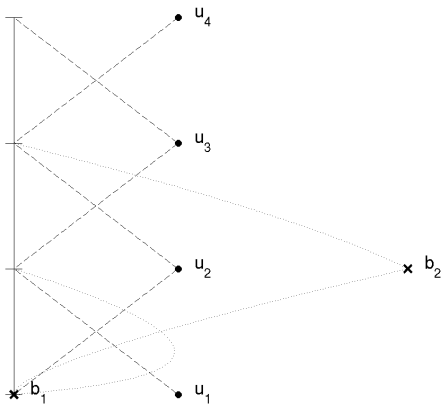

Figure 2.1: Shape functions used to represent the solution, and associated degrees of freedom (plain circles and crosses for respectively classical and extended finite elements). Classical linear finite elements use only the linear shape functions (dashed lines). Two enrichement shape functions are added near the bottom for the extended finite element method (dotted lines), here corresponding to $F(z)$ of equation 2.3.

where the total number of nodes is N and the number of extended nodes is N_X. Φ_j are the classical linear shape functions used to represent the field. $F(z)$ is the enrichement function representing the idealised analytical solution near the bottom up to a multiplicative factor

$$F(z) = ln\left(\frac{z+h+z_0}{z_0}\right). \tag{2.3}$$

Using (2.2), the logarithmic boundary layer can be exactly described by the extended shape functions. To save computational time, only the nodes located near the bottom should use extended functions, as they are not needed far from the boundary when the velocity field is smooth.

To derive the discrete extended finite element equations, we consider for simplicity a one-dimensional water column model subject to diffusion only. The velocity is then driven by

$$\frac{\partial u}{\partial t} = \frac{\partial}{\partial z}\left(\nu_v \frac{\partial u}{\partial z}\right). \tag{2.4}$$

The eddy viscosity is computed using a turbulence closure model. Using continuous finite elements, this equation has the following discrete formulation:

$$\int_{-h}^{0} \frac{\partial u}{\partial t}\widehat{u}\mathrm{d}z = \int_{-h}^{0} \frac{\partial}{\partial z}\left(\nu_v \frac{\partial u}{\partial z}\right)\widehat{u}\mathrm{d}z, \tag{2.5}$$

where $\widehat{u}$ is the Galerkin test function. We then integrate by part to obtain

$$\int_{-h}^{0} \frac{\partial u}{\partial t}\widehat{u}\mathrm{d}z = \left[\nu_v \frac{\partial u}{\partial z}\widehat{u}\right]_{-h}^{0} - \int_{-h}^{0} \nu_v \frac{\partial u}{\partial z}\frac{\partial \widehat{u}}{\partial z}\mathrm{d}z. \tag{2.6}$$

The term to evaluate at the sea bed and surface represent the Neuman boundary condition. An implicit euler temporal discreatization leads to

$$\int_{-h}^{0} \frac{u^{\mathbf{(n+1)}}}{\Delta t}\widehat{u}\mathrm{d}z = -\int_{-h}^{0} \nu_v \frac{\partial u^{\mathbf{(n+1)}}}{\partial z}\frac{\partial \widehat{u}}{\partial z}\mathrm{d}z + \int_{-h}^{0} \frac{u^{\mathbf{(n)}}}{\Delta t}\widehat{u}\mathrm{d}z, \tag{2.7}$$

where **(n)** and **(n+1)** are the considered old and new time steps. Introducing (2.2) in the discretization, we obtain

$$\begin{aligned}
&\int_{-h}^{0} \frac{\sum_{j=1}^{N} u_j^{\mathbf{(n+1)}}\Phi_j + \sum_{j=1}^{N_X} b_j^{\mathbf{(n+1)}}\left(\Phi_j F\right)}{\Delta t}\widehat{u}\mathrm{d}z \\
&\quad + \int_{-h}^{0} \nu_v \left(\sum_{j=1}^{N} u_j^{\mathbf{(n+1)}}\frac{\partial \Phi_j}{\partial z} + \sum_{j=1}^{N_X} b_j^{\mathbf{(n+1)}}\frac{\partial\left(\Phi_j F\right)}{\partial z}\right)\frac{\partial \widehat{u}}{\partial z}\mathrm{d}z \\
&\quad = \int_{-h}^{0} \frac{\sum_{j=1}^{N} u_j^{\mathbf{(n)}}\Phi_j + \sum_{j=1}^{N_X} b_j^{\mathbf{(n)}}\left(\Phi_j F\right)}{\Delta t}\widehat{u}\mathrm{d}z.
\end{aligned} \tag{2.8}$$

Following the Galerkin discretisation we replace for each node the test function by Φ_i and $\Phi_i F(z)$ to consider the extended functions. The linear system

of equations of size $(N + N_X)$ reads:

- for $0 < i < N$:

$$\begin{aligned}
&\sum_{j=1}^{N} u_j^{\mathbf{(n+1)}} \left[\int_{-h}^{0} \frac{\Phi_j \Phi_i}{\Delta t} \mathrm{d}z + \int_{-h}^{0} \nu_v \frac{\partial \Phi_j}{\partial z} \frac{\partial \Phi_i}{\partial z} dz \right] \\
&+ \sum_{j=1}^{N_X} b_j^{\mathbf{(n+1)}} \left[\int_{-h}^{0} \frac{(F\Phi_j)\, \Phi_i}{\Delta t} \mathrm{d}z + \int_{-h}^{0} \nu_v \frac{\partial (F\Phi_j)}{\partial z} \frac{\partial \Phi_i}{\partial z} dz \right] \\
&= \int_{-h}^{0} \frac{\sum_{j=1}^{N} u_j^{\mathbf{(n)}} \Phi_j \Phi_i}{\Delta t} dz + \int_{-h}^{0} \frac{\sum_{j=1}^{N_X} b_j^{\mathbf{(n)}} F\Phi_j \Phi_i}{\Delta t} dz,
\end{aligned} \tag{2.9}$$

- for $0 < i < N_X$:

$$\begin{aligned}
&\sum_{j=1}^{N} u_j^{\mathbf{(n+1)}} \left[\int_{-h}^{0} \frac{F\Phi_j \Phi_i}{\Delta t} \mathrm{d}z + \int_{-h}^{0} \nu_v \frac{\partial \Phi_j}{\partial z} \frac{\partial (F\Phi_i)}{\partial z} dz \right] \\
&+ \sum_{j=1}^{N_X} b_j^{\mathbf{(n+1)}} \left[\int_{-h}^{0} \frac{F^2\Phi_j \Phi_i}{\Delta t} \mathrm{d}z + \int_{-h}^{0} \nu_v \frac{\partial (F\Phi_j)}{\partial z} \frac{\partial (F\Phi_i)}{\partial z} dz \right] \\
&= \int_{-h}^{0} \frac{\sum_{j=1}^{N} u_j^{\mathbf{(n)}} F\Phi_j \Phi_i}{\Delta t} dz + \int_{-h}^{0} \frac{\sum_{j=1}^{N_X} b_j^{\mathbf{(n)}} F^2\Phi_j \Phi_i}{\Delta t} dz.
\end{aligned} \tag{2.10}$$

This system must be solved to obtain the new nodal values for the velocity u_j and b_j that allow a description of the velocity field over the whole domain using relation 2.2.

Using the extended finite element method for the bottom boundary layer allows to impose the no-slip condition at the sea bed, which is the real physical condition to impose:

$$u = 0|_{z=-h} \tag{2.11}$$

As the extended shape functions vanish at the sea bottom, this condition is only to be imposed to the degree of freedom associated with the classical shape function of the bottom node.

It is then possible to represent the theoretical profile of the bottom boundary layer described by relation (2.1) with the model. For these simulations, the surface velocity is enforced to its analytical value. The bottom friction velocity and roughness length are respectively set to $u_* = 0.01\ [m/s]$ and $z_0 = 0.001\ [m]$. Figure 2.2a shows the results from a simulation of the bottom boundary layers using two elements, with two enriched nodes. With few elements, the method is able to compute a solution which is very similar to the analytical one. The remaining error is due to the fact that the linear functions are not able to represent the upper part of the domain where the function is not enriched. When the number of elements is increased to nine (Figure 2.2b), the model solution cannot be distinguished from the analytical solution.

Due to the existence of linear shape functions, the extended finite element method is still able to represent the solution when it differs from the analyt-

a)

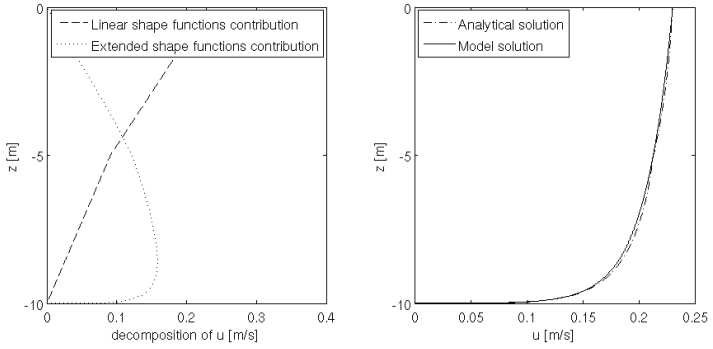

b)

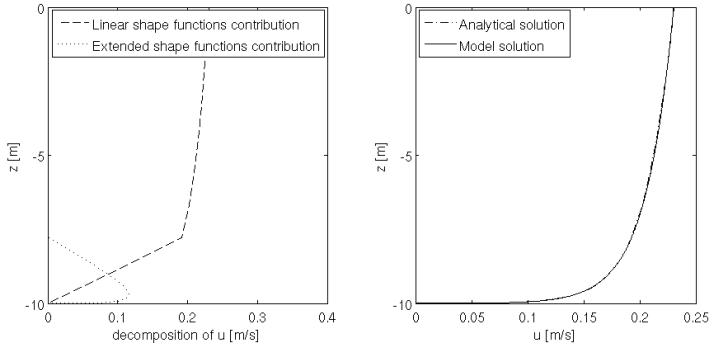

Figure 2.2: Representation of the bottom velocity using the extended finite element method with two elements (a) and nine elements (b). Only the two bottommost nodes are enriched.

ical one. Hanert *et al.* (2007), used four different methods to represent the bottom boundary layer and compared them. These methods are the classical linear finite element method with a no-slip condition at the bottom, the same method with a free-slip condition and a bottom stress as parameterisation, the extended finite elements method and the use of logarithmic shape functions near the bottom instead of the linear shape functions. While the logarithmic shape functions are good at representing the exact bottom boundary layer, the results differ from the solution when other phenomena affect the logarithmic profile of velocity (e.g. the coriolis effect). If then, the solution is no longer in the functional space used for its representation and cannot be represented by the model. Figure 2.3 shows the computation of the rotating boundary layer using the four different methods. The coriolis factor is set to $f = 10^{-4}\ s$. Figure 2.3 confirms that the use of classical finite elements with a no-slip bottom generates high discretization errors, while the parameterisation produces acceptable results. However, the latter are less precise near the bottom where the gradient of velocity is very large. The use of logarithmic shape functions is not optimal due to the coriolis effect which induces an inconsistency between the shape functions and the solution. The extended finite elements bypass this inconsistency by using simultaneously logarithmic and linear shape functions for the bottommost elements. This method is then able to compute the solution with a high precision, even in the bottom of the boundary layer.

If the extended finite element method produces very good results, it however requires a very high order integration rule in the enriched elements to obtain a good approximation of the product of logarithmic shape functions and test functions or their derivatives. It is possible to use analytical integration, but the expression of the integrals can become complex and unaffordable in a three-dimensional model. However, if the number of layers is important, the use of a high order integration rule in the bottom layers may not increase too significantly the computational time.

2.2 Residence time boundary layer

The extended finite element method is powerful to represent some types of boundary layers. However, its implementation increases significantly the level of complexity of the model to obtain results which are not always useful. The sparsity of the system matrix is also modified with the use of enriched shape functions, which can make the linear system harder and slower to be solved. If one needs to obtain a simple treatment of the boundary layer, parameterisations are often sufficient in the domains of interests covered by a marine model.

In the following article (Blaise *et al.*, 2009b), both parameterisation and extended finite element method will be developed and used to treat the boundary layer of the residence time at inflow boundaries. The residence time will then be computed on idealised and realistic problems. While the the logarith-

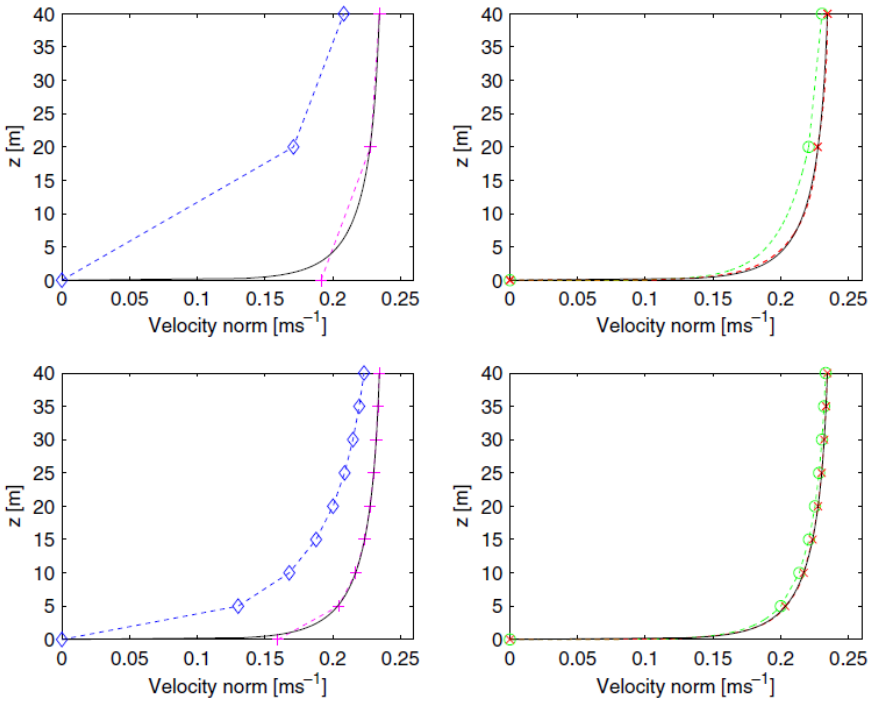

Figure 2.3: Comparison of different representation of the rotating bottom boundary layer from Hanert *et al.* (2007). Analytical solution (solid line) versus results obtained using classical linear finite elements with no-slip condition ($\diamond$) and parameterised bottom ($+$), extended finite elements ($\times$) and logarithmic bottom shape functions ($\circ$). The mesh is made of two elements (up) and height elements (down).

mic boundary layer is linked with the hydrodynamic part of the model, the residence time is a diagnostic variable, used by the modeller to have better understanding of the physical phenomena occuring. The residence time is useful to quantify the time during which a tracer will stay in a pre-defined domain. In addition to the treatment of the boundary layer, an interest of this paper is that it is associated with a recent method, developed by Delhez *et al.* (2004), that allows to compute the residence time at any time anywhere in the computational domain by using an adjoint model. This method is implemented successfully in finite elements, and a discussion explains how to maintain the consistency between residence time and hydrodynamics discrete equations. This consistency is mandatory to avoid the apparition of spurious extrema in the solution. This article shows a description of the residence time in the Scheldt estuary which has never been obtained before with such details.

Capturing the residence time boundary layer - Application to the Scheldt Estuary.

Sébastien Blaise[1], Benjamin de Brye[1], Anouk de Brauwere[2], Eric Deleersnijder[1], Eric J.M. Delhez[3] and Richard Comblen[1]

[1]Université catholique de Louvain,
Centre for Systems Engineering and Applied Mechanics (CESAME)
B-1348 Louvain-la-Neuve, Belgium

[2]Vrije Universiteit Brussel,
Analytical and Environmental Chemistry,
B-1050 Brussels, Belgium

[3]Université de Liège,
MARE, Modélisation et Méthodes Mathématiques,
B-4000 Liège, Belgium

E-mail: sebastien.blaise@uclouvain.be

Submitted to Ocean Dynamics (September 2009)

Abstract

At high Peclet number, the residence time exhibits a boundary layer adjacent to incoming open boundaries. Resolving this boundary layer would require an unacceptably high spatial resolution. Therefore, alternative methods are needed in which no grid refinement is required to capture the key aspects of the physics of the residence time boundary layer. An X-FEM representation and a boundary layer parameterisation are presented and tested herein. It is also explained how to preserve local consistency in reversed time simulations so as to avoid the generation of spurious residence time extrema. Finally, the boundary layer parameterisation is applied to the computation of the residence time in the Scheldt Estuary (Belgium/Netherlands). This timescale is simulated by means of a depth-integrated, finite element, unstructured mesh model, with a high space-time resolution. It is seen that the residence time temporal variations are mainly affected by the semidiurnal tides. However, the spring-neap variability also impacts the residence time, particularly in the sandbank and shallow areas. Seasonal variability is also observed, which is induced by the fluctuations over the year of the upstream flows. In general, the residence time is an increasing function of the distance to the mouth of the

estuary. However, smaller-scale fluctuations are also present: they are caused by local bathymetric features and their impact on the hydrodynamics.

Keywords: Residence time, Boundary layer, Parameterisation, X-FEM, Finite elements, Diagnostic, Adjoint modelling, Local Consistency

1 Introduction

The output files of most marine models are so huge that interpreting them is far from trivial, calling for the design and implementation of simple estimators of the state of the system under consideration (e.g. Deleersnijder and Delhez 2007). Several efforts have been made to introduce such estimators; among them it is worth mentioning timescales such as the age, flushing time, exposure time and residence time (Deleersnijder *et al.*, 2001; Monsen *et al.*, 2002; Delhez *et al.*, 2004a,b; Delhez and Deleersnijder, 2006; Delhez, 2006). The latter is the time taken by a particle of water to touch an open boundary of a control domain for the first time (Bolin and Rhode, 1973; Zimmerman, 1976; Takeoka, 1984; Delhez and Deleersnijder, 2006). The exposure time is an analogous concept, defined to be the accumulated time during which water parcels stay in a control domain (Delhez, 2006). Both diagnostics can be used; and the choice of the method depends on the context. The present study focuses on the residence time.

The definition of the residence time suggests a Lagrangian representation (Tartinville *et al.*, 1997; Luther and Haitjema, 1998; Miller and Luther, 2008). Then, random walks are necessary to represent diffusive processes (Nauman, 1981; Allen, 1982). The stochastic nature of Lagrangian approaches requires the computation of statistical quantities which are relevant only if the number of particles is large (e.g. Tartinville *et al.* 1997; Spivakovskaya *et al.* 2007). The direct Eulerian computation of the residence time is also possible (Wang *et al.*, 2004; Soetaert and Herman, 1995; Gourgue *et al.*, 2007; Arega *et al.*, 2008; Liu *et al.*, 2008). However, a specific tracer model run is required for the computation of the residence time at each location and at each time where and when the information is sought. Therefore, many tracer runs may be needed to estimate the residence time with a significant time-space resolution. The computing cost can be reduced by having recourse to the adjoint method recently developed by Delhez *et al.* (2004b). The latter allows one to obtain the residence time at any time and location in the whole domain by resolving an adjoint advection-diffusion problem in a backward time integration mode.

At high Peclet number, the residence time exhibits a boundary layer adjacent to incoming boundaries (Delhez and Deleersnijder, 2006). This boundary layer, induced by the homogeneous Dirichlet condition imposed at open boundaries, makes the residence time difficult to compute with common numerical methods. In a Eulerian model, spurious oscillations are likely to be

generated. This issue does not occur when the exposure time is computed, as we do not prescribe boundary conditions at the boundary of the control domain.

Although the description of the boundary layer itself may not be that important for the interpretation of the results, its effect on the neighbouring field must be taken into account. Refining the grid so as to resolve the steep gradient of the residence time can overcome this issue, but the needed resolution would lead to an unacceptably large computing time. In this study, we present solutions to treat the boundary layer without increasing significantly the computing cost.

A first possible solution is based on X-FEM, the extended finite element method (Moës *et al.*, 1999). X-FEM consists of a classical finite element method enriched by a set of test and shape functions especially designed to represent the solution whose analytical behaviour is a priori known. The method can represent exactly a solution that is known up to a multiplicative factor. The classical polynomial test and shape functions allow for a good approximation of the solution when it differs from the assumed behaviour (Hanert *et al.*, 2007). Initially designed for fracture mechanics (Moës *et al.*, 1999; Combescure *et al.*, 2005; Wyart *et al.*, 2008), this method was successfully applied to marine simulations for the representation of the logarithmic bottom boundary layer (Hanert *et al.*, 2007).

The second method consists in parameterising the boundary layer. The latter is not explicitly resolved but appropriate boundary conditions, derived from the analytical solution of an idealised problem, are enforced. This kind of parameterisation is also often used to treat the logarithmic bottom boundary layer. In this case, the bottom stress (i.e. the momentum flux) is parameterised as a quadratic function of the velocity, a formulation that is in agreement with the logarithmic nature of the velocity profile (Blumberg and Mellor, 1987; Black and Gay, 1987; Burchard, 2002).

The present article is organized as follows. Section 2 introduces the adjoint method for a depth-integrated model, along with the boundary conditions to enforce. The issue of the boundary layer of the residence time is introduced in Section 3. Two solutions to handle this boundary layer, one derived from the extended finite element method and a parameterisation are developed and validated by means of a one-dimensional test case. Section 4 introduces the concept of local consistency and explains how to ensure it for multidimensional tracer simulations backward in time. In Section 5, the residence time is computed in a realistic problem, the flow in the Scheldt Estuary. Finally, conclusions are drawn in Section 6.

2 Residence time

The two-dimensional time-dependent residence time θ can be obtained by solving backward in time the partial differential problem

$$\frac{\partial(H\theta)}{\partial t} + \nabla \cdot (H\mathbf{u}\theta) = \nabla \cdot [(-\kappa)\, H\nabla\theta] - H, \tag{1}$$

where t is the time, while $\mathbf{u}$, κ and H denote the depth-averaged horizontal velocity, the diffusivity and the total water depth, which is the sum of the surface elevation (positive upwards) and the reference water depth. It must be stressed that this equation is not a classical depth-integrated advection-diffusion equation (with a production term). If it were so, the diffusivity term would appear with a positive sign in the right-hand side, while it is negative here. In fact, equation (1) is obtained from an adjoint approach similar to that of Delhez *et al.* (2004b). Details of its derivation may be found in Appendix A.

Equation (1) must be integrated backward in time, otherwise the differential problem dealt with would be ill-posed (e.g. Garabedian, 1964). The physical meaning of this backward integration is that the residence time at time t depends on the dynamics within the interval $[t, \infty]$. The backward integration starts at time T, which corresponds to the end of the physical simulation time (i.e. the beginning of the reverse integration time). Introducing $\tau = T - t$, equation (1) transforms to

$$\frac{\partial(H\theta)}{\partial \tau} + \nabla \cdot [H\,(-\mathbf{u})\,\theta] = \nabla \cdot (\kappa H\nabla\theta) + H, \tag{2}$$

which is a classical tracer equation with reversed velocity and a source term.

The residence time is the time taken by a water parcel to touch an open boundary of a control domain for the first time. Water parcels can flow out of the control domain through open boundaries, but they are completely ignored from the moment they quit the domain. A homogeneous Dirichlet boundary condition must be enforced at open boundaries to ensure that the water parcels touching the boundary are removed from the computation (Delhez *et al.*, 2004b). In addition, a no-flux condition is imposed at closed boundaries:

$$\theta = 0 \qquad \text{at open boundaries,} \tag{3}$$

$$\boldsymbol{n} \cdot (H\nabla\theta) = 0 \qquad \text{at closed boundaries,} \tag{4}$$

where $\boldsymbol{n}$ is the outgoing unit normal to the boundary. Unfortunately, at high Peclet number, condition (3) induces a boundary layer in the vicinity of incoming (inflow in physical time) open boundaries. This boundary layer must be treated in a suitable manner in order to prevent spurious oscillations from developing.

3 One-dimensional developments

To gain insight into the residence time boundary layer issue, consider first a one-dimensional steady-state configuration with a constant depth. The do-

main is defined by $0 \leq x \leq L$ where x is the spatial coordinate. For simplicity, the velocity $u = U$ and the diffusivity $\kappa = K$ are taken to be positive constants. This configuration can be interpreted as a highly idealised channel (Delhez *et al.*, 2004b). Under these assumptions, equation (2) simplifies to

$$K\frac{\mathrm{d}^2\theta}{\mathrm{d}x^2} + U\frac{\mathrm{d}\theta}{\mathrm{d}x} + 1 = 0. \tag{5}$$

The boundaries are assumed to be open. Therefore, according to condition (3), the residence time is prescribed to be zero at $x = 0$ and $x = L$. This equation can be adimensionalised, using $x = \tilde{x}L$ and $\theta = \tilde{\theta}L/U$, and defining the Peclet number Pe as UL/K. This yields

$$\frac{1}{Pe}\frac{\mathrm{d}^2\tilde{\theta}}{\mathrm{d}\tilde{x}^2} + \frac{\mathrm{d}\tilde{\theta}}{\mathrm{d}\tilde{x}} + 1 = 0. \tag{6}$$

For the sake of simplicity, the tildes are dropped hereinafter.

Figure 1: Residence time for the dimensionless, steady-state one-dimensional problem for various Peclet numbers. The thick curve represents the analytical solution. The thin curve represents the numerical solution obtained with a classical finite element method where the circles indicate the mesh nodes. The dimensionless thickness of the boundary layer is Pe^{-1}. The mesh Peclet number is defined by $Pe^h = U\Delta x/K$, where Δx is the grid spacing.

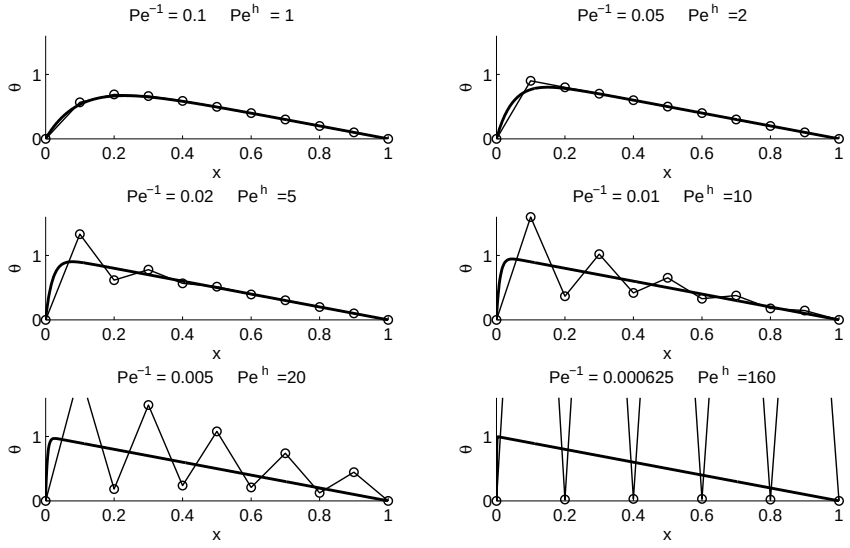

Solving equation (6) under the abovementioned Dirichlet boundary conditions leads to

$$\theta(x) = \frac{1 - e^{-Pe\ x}}{1 - e^{-Pe}} - x. \tag{7}$$

As pointed out by Delhez and Deleersnijder (2006), this solution exhibits a boundary layer near the inflow boundary, i.e. in the vicinity of $x = 0$. The thickness of this boundary layer is of the order of Pe^{-1}, i.e. K/U in dimensional variables. This can be seen in Figure 1 for values of the Peclet number ranging from 10 to 1600. Figure 1 also shows the results of a linear finite-element resolution of equation (5), with a mesh made up of ten elements. Accordingly, the solution is approximated by

$$\theta(x) \approx \theta^h_{\text{fem}} = \sum_{j=1}^{N} \theta_j \phi_j(x), \tag{8}$$

where ϕ_j is a piecewise linear shape function corresponding to the j-th node of the mesh whose total number of nodes is N. The nodal values associated with the shape functions ϕ_j are denoted θ_j. Figure 1 shows that the solution oscillates if the Peclet number is higher than a threshold value. It is shown in Appendix B that, for a finite-differences scheme, oscillations appear when the mesh Peclet number $Pe^h = U\Delta x/K$ is higher than 2, where Δx is the grid spacing. It can be seen that the linear finite elements scheme used for the one-dimensional simulation with U and K constants and a homogeneous mesh is strictly equivalent to the finite-differences scheme. This is illustrated in Figure 1, which exhibits spurious oscillations for $Pe^h > 2$.

To address this issue, one may have recourse to the X-FEM method (Moës *et al.*, 1999), which is able to represent exactly a solution known up to a multiplicative factor. A polynomial component needs to be retained to take into account the discrepancies between the actual solution and that assumed in X-FEM. Accordingly, the set of shape functions in (8) is enriched with shape functions derived from the exact solution:

$$\theta(x) \approx \theta^h_{\text{fem}} + \theta^h_{\text{x-fem}} = \sum_{j=1}^{N} \theta_j \phi_j(x) + \sum_{j=1}^{N_x} b_j \phi_j(x) F(x), \tag{9}$$

where N_x is the number of enriched nodes. $F(x)$ is a function derived from the *a priori* known shape of the solution. It describes the solution up to a multiplicative factor, the latter being unknown. For the present one-dimensional experiment, this function is meant to represent the boundary layer. It is obtained by extracting from the exact solution (7) the part that is associated with the steep residence time gradient in the boundary layer, i.e.

$$F(x) = 1 - e^{-Pe\ x}. \tag{10}$$

The second linear term of (7) will be handled by the classical linear shape functions. Thus, multiplying (10) by a nodal factor in combination with the linear shape functions contribution will allow for a good representation of the solution.

The residence time is computed in the idealised one-dimensional channel using X-FEM with an enriched shape function for the first node of the mesh (corresponding to the inflow boundary). The X-FEM results (Figure 2b) do not show the strong oscillations that appear when a classical finite element method is used (Figure 1), and are very close to the analytical solution (Figure 2a). However, oscillations still appear for moderate mesh Peclet numbers (e.g. when $Pe^h = 5, 10, 20$). These oscillations appears only when the first node is enriched and the boundary layer length exceeds the width of the enrichment zone. One might think that it is desirable to enrich more nodes. But, when doing so, problems arise, especially if extended shape functions are present where the solution is quasi-linear. In this case, the enriching function $F(x)$ is almost equal to 1, and the linear system to be solved becomes ill-conditioned because $\phi_j(x)$ and $\phi_j(x)F(x)$ are almost equivalent. It is thus safe to enrich

Figure 2: Residence time for the dimensionless, steady-state one-dimensional problem for various Peclet numbers (the label on the curves indicates the mesh Peclet number, which is $0.1Pe$ in this case). The simulation configuration corresponds to Figure 1. Dashed vertical lines correspond to the mesh nodes position. (a) Analytical solution, (b) Boundary layer treated using the X-FEM method, (c) Parameterised boundary layer.

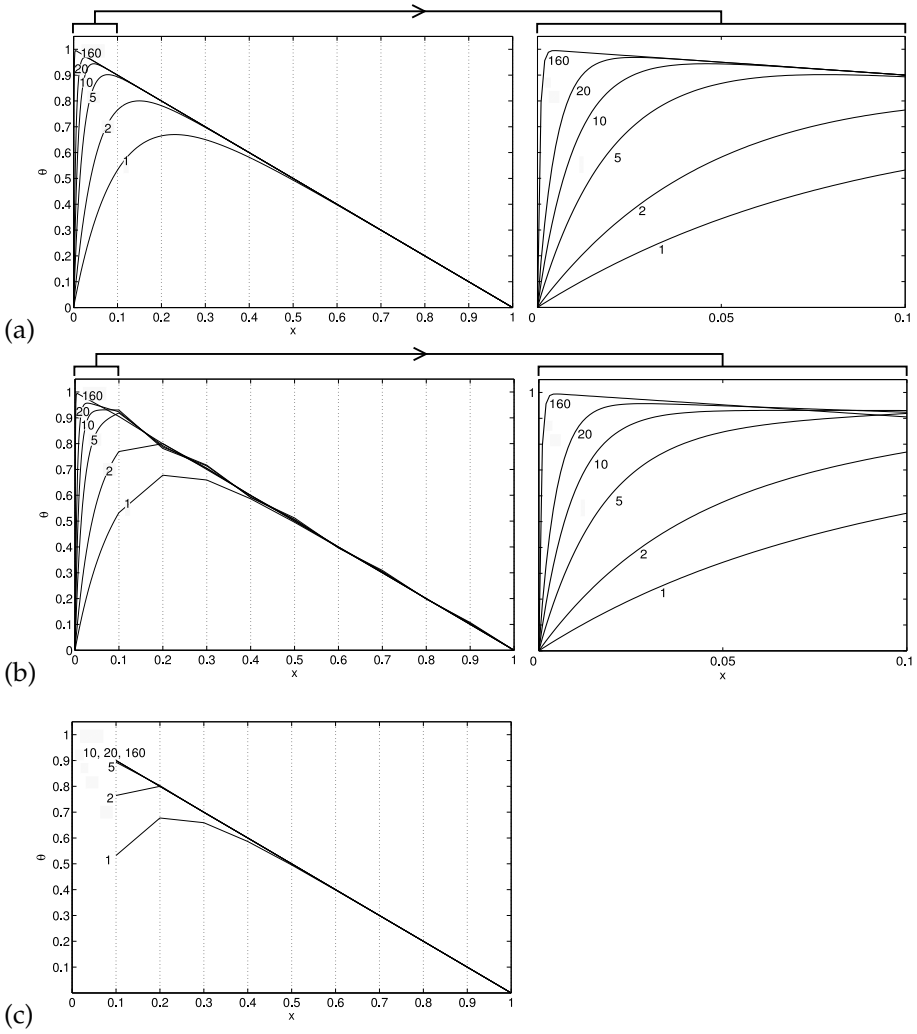

only the node that is adjacent to the boundary, or to resort to a strategy consisting in determining *a priori* the number of nodes to enrich to obtain the most accurate solution while retaining a well-conditioned system. The second option is unlikely to be easy to implement. Furthermore, in many realistic applications, the width of the boundary layer is generally much smaller than the element size, implying that enriching only the first node will be sufficient in most cases.

While the X-FEM method seems promising in an idealised problem, its application in a realistic model might present some difficulties:

- As they depend on the velocity, the extended shape functions vary in time. They thus need to be updated after each temporal iteration. The solution at time $t + \Delta t$ is expressed as a linear combination of the shape functions defined at time t. However the test functions at time $t + \Delta t$ must be used to compute the next time step. It is thus necessary to use two different sets of shape/test functions.

- The shape functions are expressed as a function of the normal distance from the boundary. It is possible to define a generalized distance to the the boundary in complex geometries (Fares and Schröder, 2002), but this distance can be more difficult to compute.

- The enrichment is performed only near the boundary, which can be difficult to handle in a general finite elements code.

- The steepness of the enriched shape functions requires a very high order integration rule. While an exact integration can be performed in the one-dimensional model, it can be more complex in a two-dimensional framework. A possible solution would be to develop integration rules specifically designed for the function to integrate, but this is not straightforward.

Because of these difficulties, it seems appropriate to look for another solution to deal with the boundary layer. An alternative consists in a parameterisation, derived from the analytical solution of the one-dimensional steady-state problem. The idea is to derive an appropriate boundary condition for the outer solution of the boundary layer problem (Figure 3). The representation of the boundary layer is indeed not crucial as long as its effects are taken into account.

We need to enforce a correct boundary condition at the limit of the computational domain. The one-dimensional steady-state equation for the residence time (5) is an ordinary differential equation which can be solved analytically. We first assume that the velocity and diffusivity are constant in the parameterised zone. This hypothesis is acceptable, as this zone generally is very narrow compared with the other length scales of the flow under consideration. Furthermore, the boundary for the residence time is not a physical boundary for the hydrodynamics (i.e. it is just an arbitrary limit fixed by the user),

Figure 3: Parameterisation of the boundary layer for the residence time. The numerical domain boundary is moved to avoid the computation of the boundary layer.

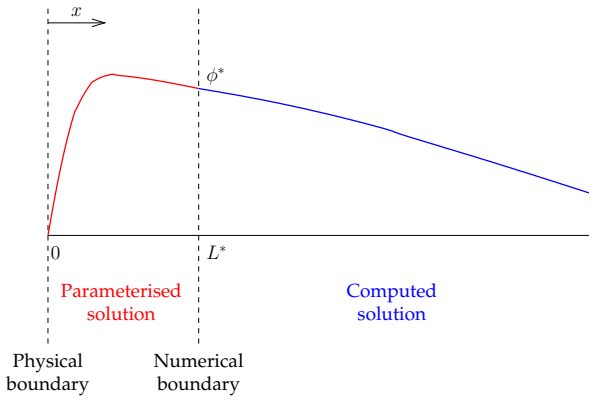

and thus does not affect the velocity and diffusivity. Under these hypotheses, equation (5) will be solved in the parameterised domain to obtain the gradient to enforce (Neumann condition) at the boundary of the computational domain. Following condition (3), a zero residence time is to be imposed at $x = 0$, and we denote θ^* the value of the residence time computed by the model at $x = L^*/L$ (see Figure 3), the boundary of the computational domain (called hereafter numerical boundary). Then, the exact expression of the residence time may be rewritten as follows

$$\theta = \frac{e^{-Pe\,x} - 1}{e^{-Pe\frac{L^*}{L}} - 1}\left(\theta^* + \frac{L^*}{L}\right) - x. \tag{11}$$

To know the gradient to impose at the numerical boundary, expression (11) is derived with respect to x and then evaluated at $x = L^*/L$, leading to

$$\left.\frac{\mathrm{d}\theta}{\mathrm{d}x}\right|_{x=\frac{L^*}{L}} = Pe\frac{e^{-Pe\frac{L^*}{L}}}{1 - e^{-Pe\frac{L^*}{L}}}\left(\theta^* + \frac{L^*}{L}\right) - 1, \tag{12}$$

which corresponds in the dimensional world to:

$$\left.\frac{\mathrm{d}\theta}{\mathrm{d}x}\right|_{x=L^*} = \frac{1}{K}\frac{e^{-UL^*/K}}{1 - e^{-UL^*/K}}\left(\theta^* U + L^*\right) - \frac{1}{U}. \tag{13}$$

It is worth mentioning that the implementation does not require to know the length scale L, as the latter does not appear in (13).

This technique provides numerical results that are devoid of any oscillation (Figure 2c) and very close to the analytical solution (Figure 2a). It must be

stressed, however, that the presence of an oscillating mode is not directly related to the boundary conditions (3); this mode is part of the general solution of the discrete equation if the Peclet number exceeds a critical value. However, selecting the appropriate strategy to impose boundary conditions can strongly reduce the amplitude of the oscillatory mode, particularly at high Peclet number (Appendix C) .

As the X-FEM and parameterisation methods were developed from a time-independent analytical solution, it is useful to validate them on a transient simulation to make sure that they are still relevant if the solution varies in time. In a time-dependent configuration, the velocity in the parameterised region, U, can sometimes be equal to zero. If so, (12) contains divisions by zero, and cannot be computed. This case must be treated separately. If $U = 0$, the advection term of equation (5) vanishes, and the equation for the residence time reduces to

$$K\frac{\mathrm{d}^2\theta}{\mathrm{d}x^2} = -1. \tag{14}$$

Under the previously-used assumptions, the analytical solution of equation (14) in the parameterised zone is

$$\theta = -\frac{x^2}{2K} + \frac{L^* x}{2K} + \frac{\theta^* x}{L^*}. \tag{15}$$

Therefore, the gradient to enforce on the numerical boundary is:

$$\frac{\mathrm{d}\theta}{\mathrm{d}x} = -\frac{x}{K} + \frac{L^*}{2K} + \frac{\theta^*}{L^*}. \tag{16}$$

Expressions (12) and (16) exhibits terms that are linear in θ^*, the other terms being independent of θ^*. The former terms must be treated implicitly to ensure the stability of the numerical method; otherwise an unacceptably small time step is to be used.

To validate the method for a time-dependent flow, we consider the same one-dimensional domain, the velocity being modulated in time by a sine representing an idealised tide. A residual velocity $U_{\mathrm{residual}} = U_{\mathrm{tide}}/100$ is considered, where U_{tide} is the amplitude of the velocity associated with the tidal oscillations. The variables are still dimensionless, and the ratios between parameters are chosen to be comparable to a realistic situation, roughly similar to the characteristic scales encountered in the simulations of the Scheldt Estuary (Section 5). The tidal period is $T_{\mathrm{tide}} = 0.864$. The Peclet number is set to $Pe = 1000$. The left half of the domain has a mesh size of $0.02L$, leading to a maximum mesh Peclet number $Pe^h = 20$. The right half of the domain has a mesh resolution of $10^{-3}L$. Only the left open boundary is treated specifically, while the right open boundary has a sufficient resolution to handle the boundary layer.

A first run is performed using a high-resolution model (mesh size of $10^{-3}L$) so as to obtain a reference solution (Figure 4a). To remove the effects of initialisation, the solution is shown after a simulation time of 30 tidal periods, corresponding approximately to twice the residence time (Delhez *et al.*, 2004b).

Figure 4: Evolution of the residence time for the transient one-dimensional problem, after an initialisation of 30 tidal periods ($\tau' = \frac{\tau}{T_{\text{tide}}} - 30$). The colorbar indicates the residence time. (a) High-resolution solution, (b) Boundary layer treated using the X-FEM method, (c) Parameterised boundary layer.

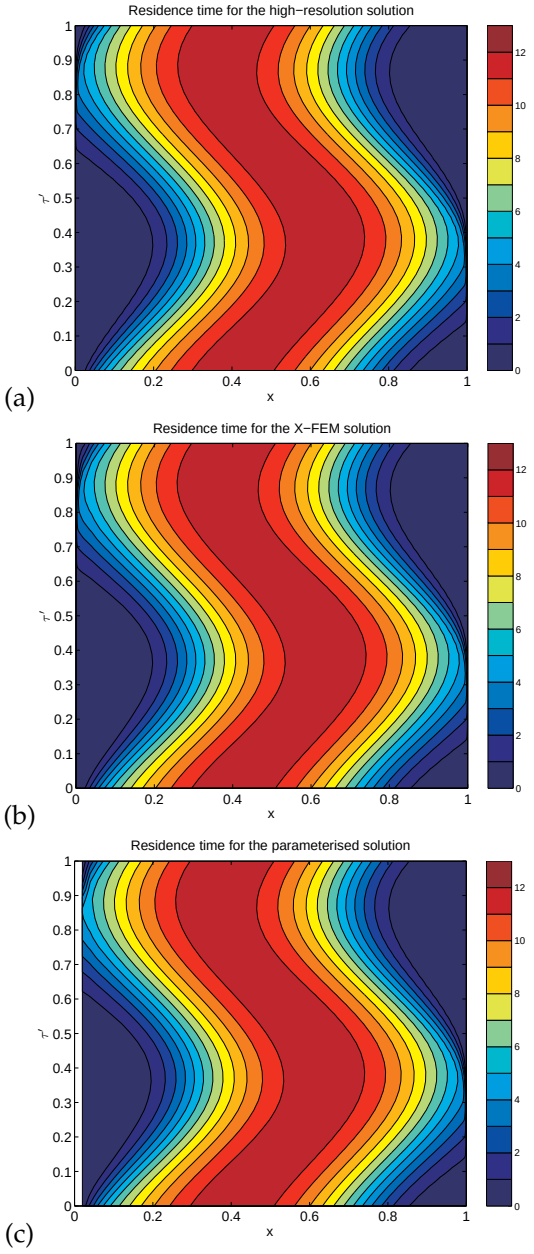

(a)

(b)

(c)

Due to the residual flow, the peak of the residence time is shifted towards the left of the domain; and the solution is non symmetric. This is clearly visible in the middle of the domain, represented by the dashed lines on Figure 4. The X-FEM solution (Figure 4b) is very similar to the high-resolution solution, even in the boundary layer. The parameterised solution (Figure 4c) does not show the boundary layer, but the residence time in the rest of the domain is well computed.

While the X-FEM method allows for an excellent representation of the boundary layer, it was pointed out above that its application in a two-dimensional realistic model can become quite intricate. For this reason, and as we do not need to know exactly the shape of the boundary layer, we will only use the parameterisation method for the realistic application. This method has the advantage of being very simple to implement.

4 Consistency

For simulations involving hydrodynamics and tracer simulations, special attention must be paid to local consistency. A passive tracer simulation is said to be locally consistent if the numerical scheme is such that the tracer concentration remains constant as time progresses, assuming that the initial concentration was homogeneous in space (White *et al.*, 2008). This concept may be applied to the transport terms of the residence time equation, in order to prevent the development of spurious extrema. The latter can be rather strong in coastal and estuarine areas, partly because the sea surface elevation is in many locations of the same order of magnitude as the unperturbed depth. White *et al.* (2008) showed that a discrete compatibility between the free-surface equation and the tracer equation must be fulfilled to ensure consistency. This compatibility is of two kinds:

- **Spatial compatibility** is ensured if the discrete advection operator for a unit tracer simplifies to the divergence term of the incompressibility equation $\nabla \cdot ((h+\eta)\mathbf{u})$. This is obtained by using the same element to represent sea surface elevation and tracers.

  Here we use linear discontinuous Galerkin elements. The Riemann solver used to deduce interface values for velocities and sea-surface elevation must be the same for tracer and continuity equations. The mesh used to compute the residence time is a submesh of the global mesh used for the hydrodynamics simulations. Hence, there is no error due to interpolation or projection of data.

- **Temporal compatibility** is more complex, as we use a residence time simulation which is reversed in time. As we use an implicit Euler method, the time discretisation of the free surface equation reads

$$\frac{\eta^{n+1}-\eta^n}{\Delta t} = -\nabla \cdot \left((h+\eta^{n+1})\mathbf{u}^{n+1}\right), \tag{17}$$

where η is the free surface elevation and h is the water depth at rest. The superscripts correspond to the time step at which the variables are expressed, $n+1$ being the new time step in the physical time (not the simulation time) and n being the old one. If we reverse the time of the simulation, $n+1$ and n need to be switched in the mass term. The opposite of the velocity must be taken for the divergence term, the latter still being computed at time $n+1$ to be consistent with the forward simulation:

$$\frac{\eta^{n+1}-\eta^n}{-\Delta t} = \frac{\eta^n-\eta^{n+1}}{\Delta t} = -\nabla\cdot\left((h+\eta^{n+1})(-\mathbf{u}^{n+1})\right). \qquad (18)$$

The variables used for the residence time equation must be taken at the same time than the corresponding variables in the free surface equation. Thus, the time discretisation of the residence time equation reads

$$\frac{(h+\eta^n)\theta^n-(h+\eta^{n+1})\theta^{n+1}}{\Delta t} = -\nabla\cdot\left((h+\eta^{n+1})(-\mathbf{u}^{n+1})\theta^n\right). \qquad (19)$$

Only the advection and mass terms are taken into account as they are the only ones that need to be compatible with the free surface equation. Source and diffusion terms do not break consistency because the first one is constant over the whole domain and the second one depends on the gradient of the residence time concentration, which is zero if the tracer is constant in space. The mean depth h being constant in time, it is obvious that, for a constant θ, expressions (18) and (19) are equivalent. We thus need to use the variables η and $\mathbf{u}$ at the times corresponding to equation (19) to ensure the local consistency when time is reversed. Hydrodynamic results must then be saved at each time step to reload them for the adjoint simulation. As the method is implicit, the number of time steps can be reduced to a reasonable amount.

5 Application to a two-dimensional realistic problem

The residence time is now computed in a two-dimensional realistic domain, i.e. the Scheldt Estuary (Belgium/Netherlands). First, the hydrodynamics is simulated using the two-dimensional version of the finite element model SLIM (Comblen *et al.*, 2009; de Brye *et al.*, 2009, `http://www.climate.be/SLIM`). This hydrodynamic simulation concerns most of the North Western European Continental Shelf, the Scheldt Estuary, the Scheldt River and the fraction of its tributaries under the influence of tides, the latter two being represented by a one-dimensional mesh (Figure 5). The residence time is then computed backward in time in the Scheldt Estuary sub-domain. The computational grid is unstructured and refined in the regions of interest (e.g. the Scheldt Estuary) or where the dynamics is more demanding (e.g. next to coastlines). The mesh is made up of 26000 triangular elements, and 5000 of them are located in the Scheldt Estuary. The river and its tributaries are represented

Figure 5: Unstructured mesh used for the numerical simulations, with a zoom on the Scheldt Estuary (lower panel). The blue part of the mesh (Scheldt Estuary) is used for the residence time computations. The mesh is made up of 26000 triangular elements, and 5000 among them are located in the Scheldt Estuary. The river and its tributaries are represented by 350 one-dimensional elements. The mesh resolution is about $400\ m$ in the one-dimensional rivers and varies from 150 metres to 30 kilometres in the two-dimensional domain.

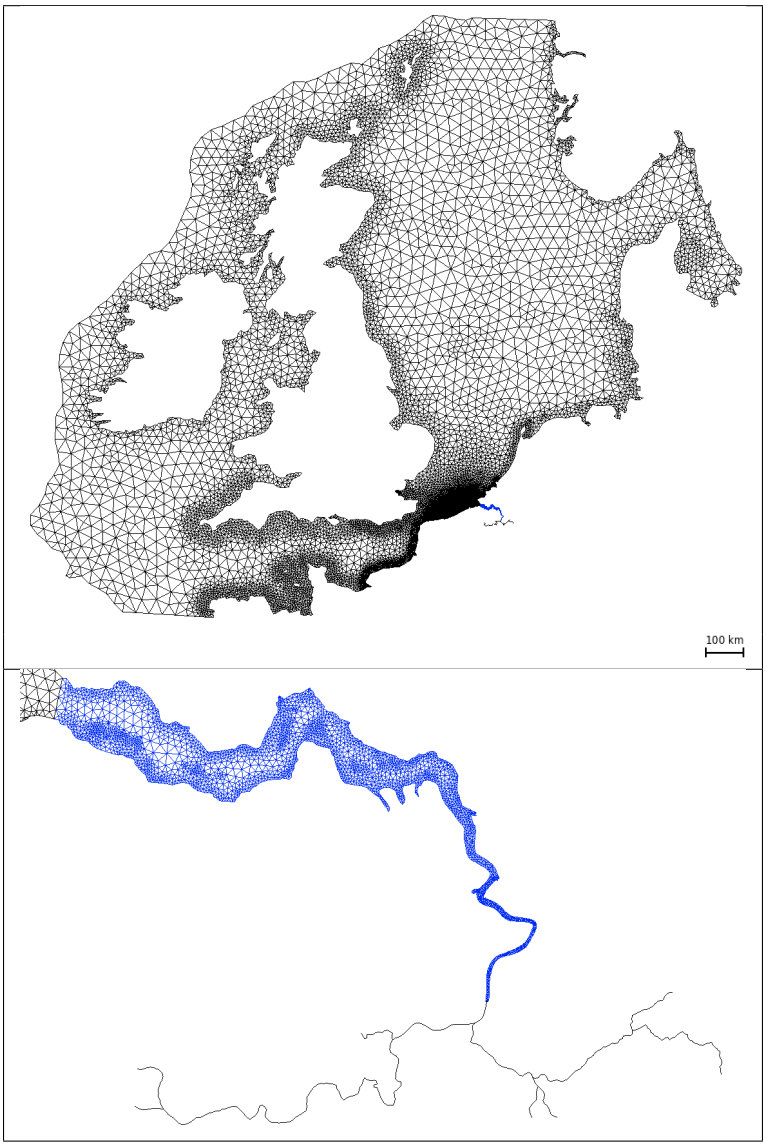

by 350 line elements. The mesh size is about $400\ m$ in the one-dimensional river and tributaries; and it varies from 150 metres to 30 kilometres in the two-dimensional domain. The minimum thickness of the boundary layer $\frac{\kappa}{(-\mathbf{n}\cdot\mathbf{u})_{\max}}$ is approximately 10 metres near the upstream boundary and 70 metres near the sea mouth boundary. The characteristic spatial resolution at the estuary/river interface ($150\ m$) and at the sea mouth ($400\ m$) provides the reference value for the length scale L^* used in the boundary representation. The model and its validation on the present domain are described in detail by de Brye *et al.* (2009). At the shelf break, the sea surface elevation is prescribed from values of the TPXO model, which assimilates satellite altimetry data (Egbert *et al.*, 1994). The following tidal constituents are taken into account: M_m, M_f, Q_1, O_1, P_1, K_1, N_2, M_2, S_2, K_2, and M_4. The surface atmospheric pressure and the wind velocity are obtained from the NCEP Reanalysis data provided by the NOAA/OAR/ESRL PSD (Kalnay *et al.*, 1996). The non-tidal part of the flow in the Scheldt and its tributaries is obtained from various sources, which are mentioned in de Brye *et al.* (2009).

Figure 6 shows the evolution of the residence time in the Scheldt Estuary on February 1, 2001. As the residence time is defined to be the time needed to touch an open boundary of the estuary for the first time, the residence time decreases towards both the upstream and downstream ends. Obviously, most of the water will eventually leave through the mouth of the estuary, because the residual current is directed from the land to the sea. However, due to the tidal motion, some water can indeed cross the upstream boundary first. The residence time varies with the tidal phase. At the sea mouth, the residence time is highest at the end of the ebb tide, because the water will be pushed into the estuary during the coming rising water. Conversely, at the end of flood tide, the residence time is relatively low. This simply reflects the fact that external water has been entering the estuary during rising tide but much of it will be pushed back out soon. The opposite behaviour is observed at the upstream boundary, where rising water correspond to an outflow: the residence time is highest at the end of flood tide, while it is lowest at the end of ebb tide. In addition to tidal effects, Figure 6 also shows that the residence time varies spatially, due to bathymetry and related hydrodynamical features. For instance, the large tidal flat area of the Verdronken Land van Saeftinghe (Figure 6a), is associated with longer residence times than the surroundings. This is because this area is very shallow with a few trenches (the only parts included in the computational domain) and therefore the water velocity is rather low. It is the first time residence times in the Scheldt Estuary have been estimated in such a detailed way, i.e. with such a space-time resolution. The range of the residence time (0 - 56 days) corresponds well with previous studies estimating residence times in a number of longitudinal boxes (0 - 50 days, Soetaert and Herman (1995)) or the nominal flushing time for the entire estuary (25 - 65 days, Steen *et al.* (2002)). Note that these results refer to winter situations and that the residence time tends to increase significantly in summer, up to 70 days (Soetaert and Herman, 1995) or even higher, depending on how much the freshwater

Figure 6: Residence time in the Scheldt Estuary on February 1, 2001 during a tidal period. The arrows are a qualitative indication of the transport through open boundaries. The residence time interval between isolines is five days.

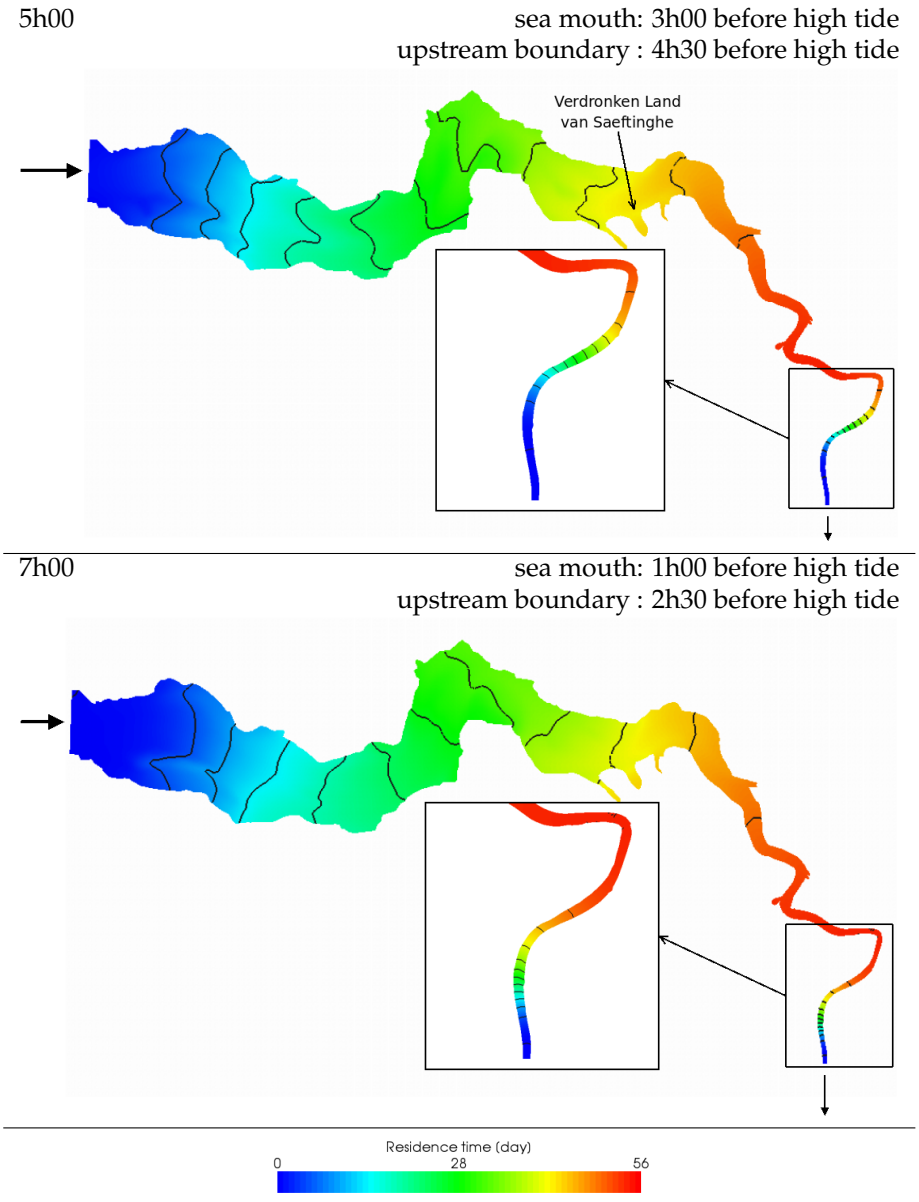

9h00 sea mouth: 1h00 after high tide
upstream boundary : 0h30 before high tide

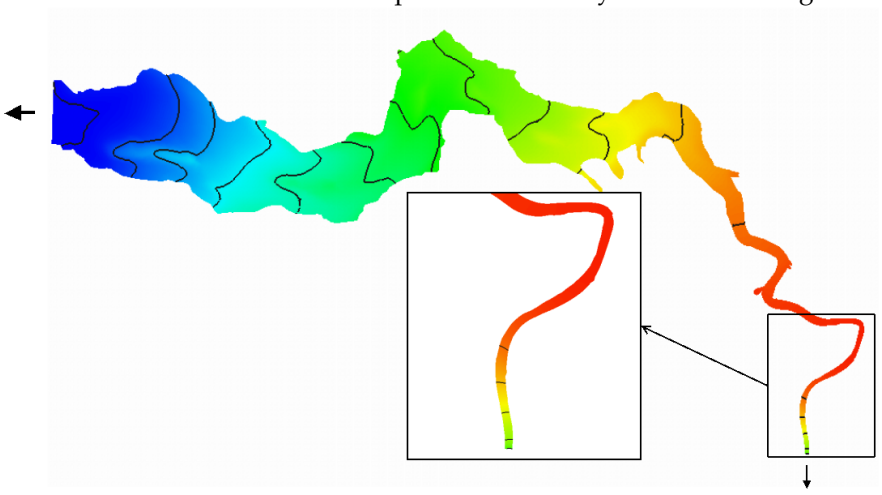

11h00 sea mouth: 3h00 after high tide
upstream boundary : 1h30 after high tide

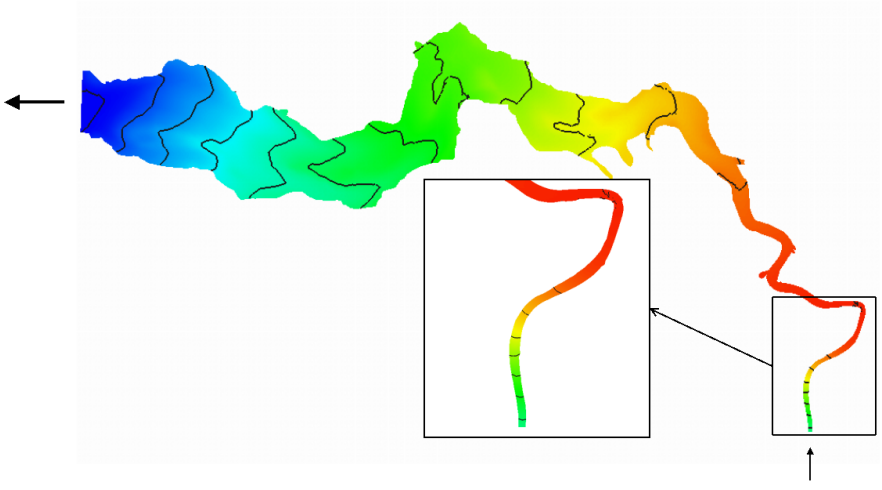

13h00 sea mouth: 1h15 before low tide
upstream boundary : 2h45 before low tide

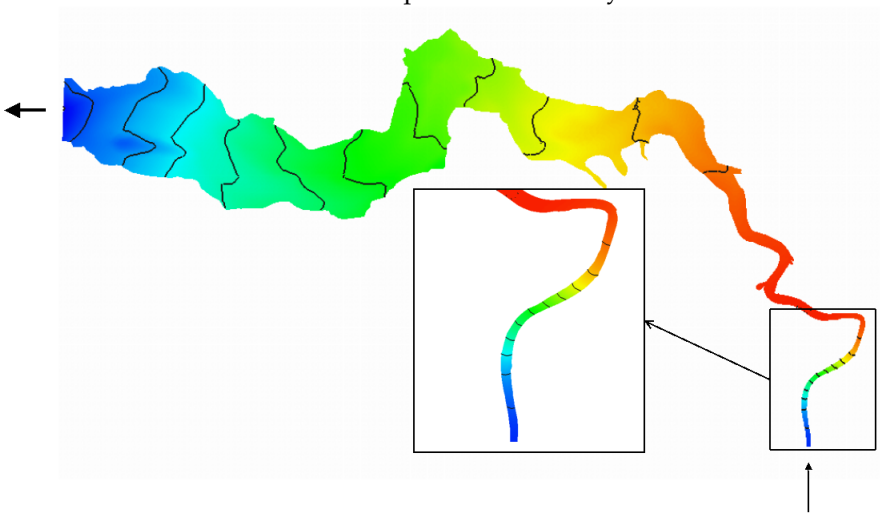

15h00 sea mouth: 0h45 after low tide
upstream boundary : 0h45 before low tide

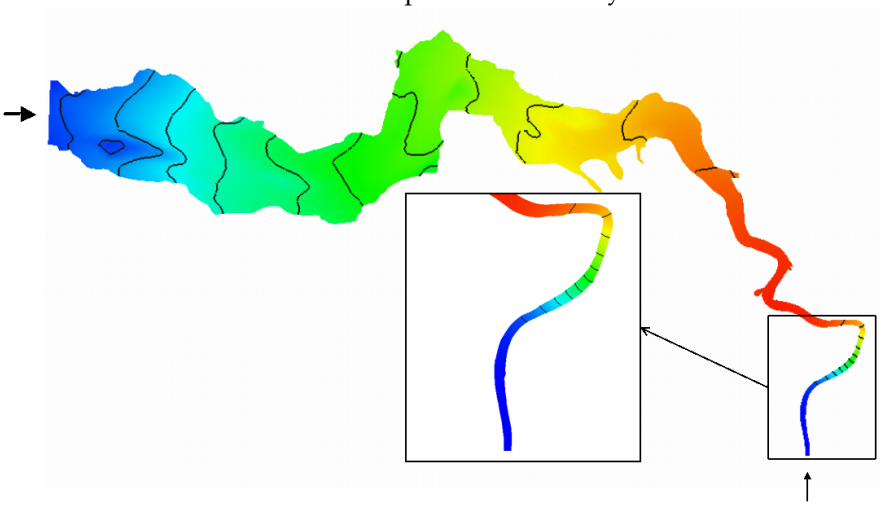

Figure 7: Mean residence time over the estuarine domain. The red curve represents a one day running mean taken to filter out tidal oscillation. Results between the dashed line (November 1, 2001) and December 31, 2001 correspond to the initialisation of the backward simulation and cannot be trusted (a period of twice the order of magnitude of the residence time, following Delhez *et al.* (2004b)).

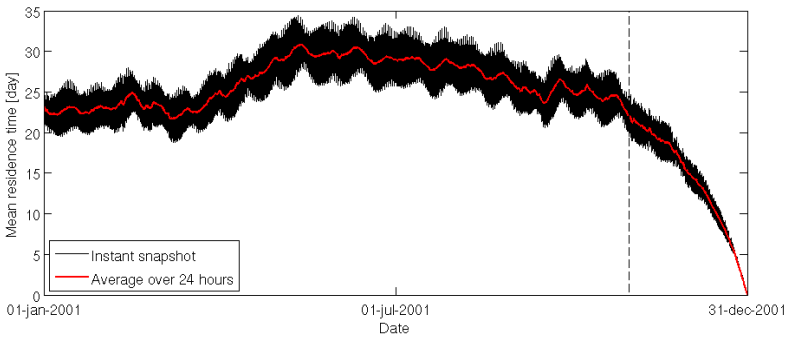

discharge decreases. This seasonal variation, related to the Scheldt flow variability, is also observed in Figure 7 showing the mean residence time over the whole estuary, as it is computed backward from December 31 to January 1, 2001. Besides the seasonal cycle and the high frequency variability of the semi-diurnal tidal cycle (discussed above), Figure 7 also displays a fortnightly variation in the mean residence time, corresponding to the spring-neap tidal cycle. Note that the results from November, 2001 to December, 2001 correspond to the initialisation of the backward simulations and cannot be trusted. According to Delhez *et al.* (2004b), the results become significant after an initialisation period whose duration is about twice the mean residence time, i.e. about two months.

It is interesting to understand how different tidal components act upon the residence time. To this aim, a tidal decomposition using the **T_TIDE** software (Pawlowicz *et al.*, 2002) was performed on the residence time field with data covering the period from May, 2001 to October, 2001. Figure 8 shows the amplitudes of the residence time fluctuations associated with the M_2, S_2 and M_{sf} tidal components. As the adjoint method is used to compute the residence time, these amplitudes can be computed over the whole domain. As in the hydrodynamics, the M_2 component is clearly dominant. This variability is related to the displacement of the residence time structure by the tidal excursion. The S_2 signal is weaker, but its amplitude distribution over the domain is very similar. This is due to the fact that semi-diurnal lunar (M_2) and solar (S_2) components are characterised by a similar period (respectively $12.42\ h$

Figure 8: Amplitude of the residence time variations associated with the M_2, S_2 and M_{SF} tidal components, in days.

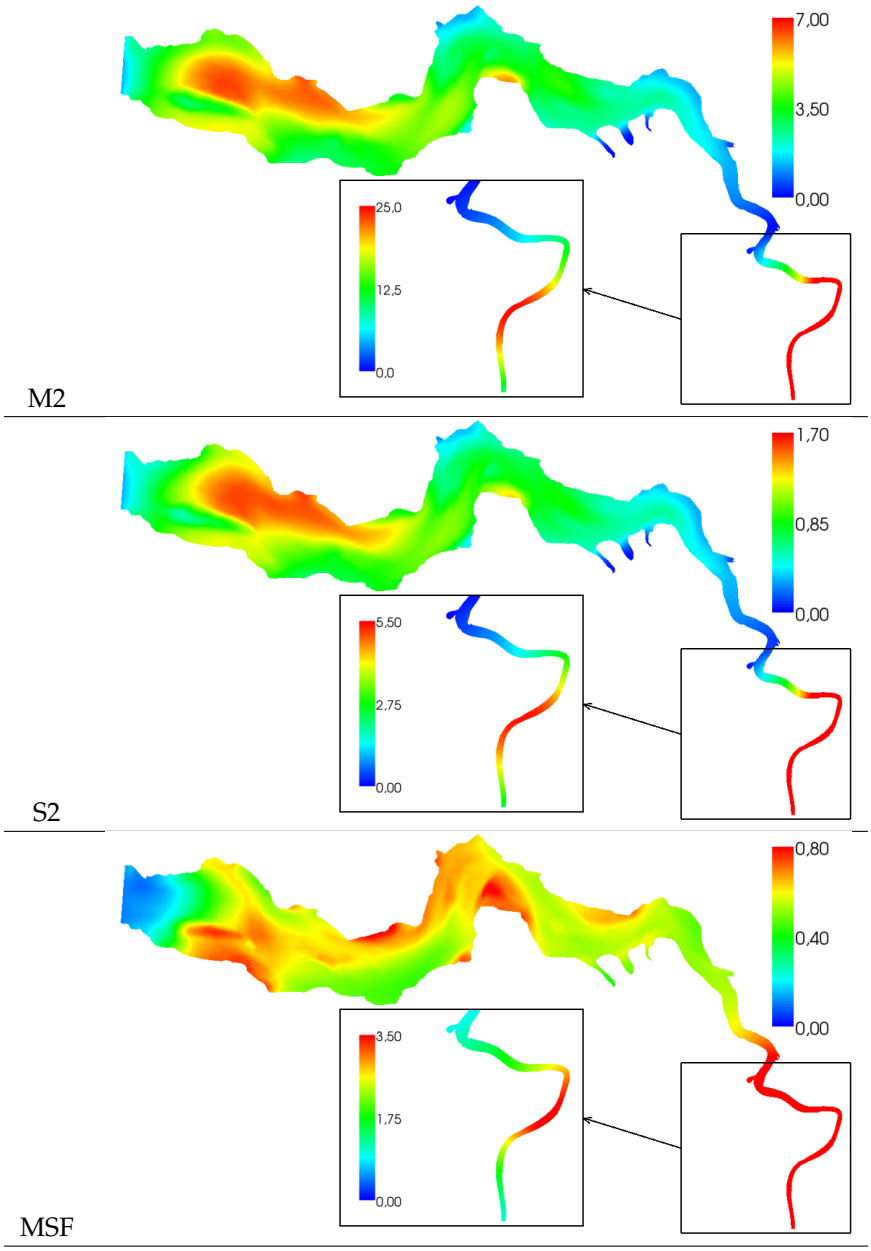

and $12\ h$). The small amplitudes next to the boundaries are an effect of the boundary layer related to the fact that the residence time should be zero at the open boundaries. However, the variability a few kilometers downstream the upstream boundary is very high. The water at rising tide will be carried to the river and will then quit quickly the control domain. At falling tide, most of the water in this zone will flow toward the sea mouth and after many tidal cycles will quit the control domain by the downstream boundary. Its residence time will then be much higher, explaining the high variability in this region. The fortnightly signal M_{sf} of period 13.66 days is induced by the combination of M_2 and S_2 components. As this signal is related to slower variations, it generates a larger boundary layer compared to semi-diurnal components. The residence time in the trenches of the Verdronken Land van Saeftinghe is almost not affected by tidal components, because the temporal variablility of the residence time is limited in this zone. However, a slight temporal variation is related to the M_{sf} period. This is because the variations associated with the main flow are too fast to significantly influence the residence time in this zone; but the variations of the flow corresponding to the fortnightly tidal component are slow enough to drain or fill sufficiently the trenches to impact somewhat the residence time. The residence time variations associated with the fortnightly signal are stronger on sandbanks, because these areas have a relatively large water depth during spring tides (lower residence time), but are covered with a thin layer of water during neap tides, enhancing the relative impact of bottom friction (higher residence time).

Figure 9 shows the residence time along a longitudinal section from the estuary/river interface. The snapshots are taken at times similar to those of Figure 6. As expected, the residence time remains always positive, and tends to zero at the boundaries. The influence of the boundary layer is visible at 11h00. After that time, the water flux enters in the estuary from the river. This inflow boundary influences the residence time in the backward simulations to create the boundary layer which is fully developed at 11h00. For the solution using the parameterisation of the boundary layer, the latter is entirely comprised in the parameterised zone, while the solution using a Dirichlet boundary condition oscillates. If we continue back in time, the outgoing flux breaks the boundary layer and the residence time decreases smoothly in space near the boundary. The residence time at both inflows and outflows is well represented by the model. In the case of the Scheldt Estuary, the issue of the boundary layer is rendered less severe by the time dependency of the flow, as the boundary layer disappears every time the tide reverses. In a flow exhibiting a unique direction, this problem would be more critical as the boundary layer would be present during the whole simulation (Delhez and Deleersnijder, 2006).

Figure 9: Residence time along the line A-B on February 1, 2001 during a tidal period. Solutions using the parameterisation of the boundary layer (black) and a Dirichlet boundary condition (red).

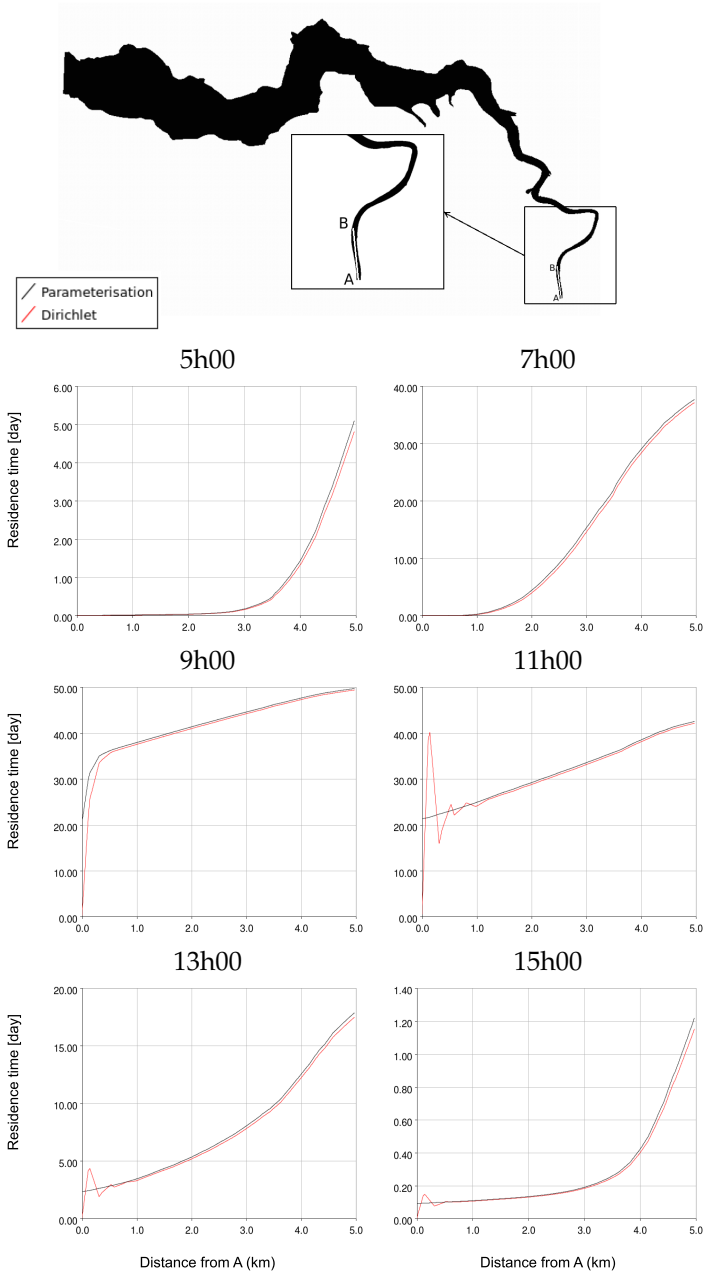

6 Conclusion

The adjoint method from Delhez *et al.* (2004b) presumably is the only one that allows one to obtain at an acceptable CPU cost the residence time at any time and location in the domain of interest. Thus, the residence time is also computed near boundaries, where it exhibits a boundary layer whose characteristic length is generally much smaller than the mesh size.

Two methods were presented for dealing with the residence time boundary layer without explicitly resolving it. The first one, using the extended finite elements method, consists in enriching the functional space available for the representation of the field with shape functions derived from an idealised analytical solution. It is able to represent the boundary layer itself with a high degree of precision and has been validated on one-dimensional stationary and non-stationary configurations. While this method seems promising to represent the boundary layer of the residence time, its implementation in a two-dimensional or three-dimensional realistic model could be revealed difficult.

The second method is a parameterisation of the boundary layer, the latter not being explicitly solved. The effect of the boundary layer is parameterised by imposing on the boundary a normal gradient of the solution, whose expression was developed from an idealised analytical behaviour. This method is easy to implement in realistic models and produces results which are physically acceptable and devoid of any spurious oscillation. This method was validated on one-dimensional simulations and applied to a two-dimensional realistic configuration.

The residence time was computed in the Scheldt Estuary with a high level of detail. The amplitudes of its variations associated with the main tidal components were obtained over the whole domain, showing that the residence time temporal variability is mainly affected by the semidiurnal signals. However, the spring-neap variability also has an influence on the residence time, particularly in the sandbanks and shallow areas. On top of the tidal effects, the residence time varies spatially, due to the bathymetry and related hydrodynamical processes.

The use of the adjoint method to compute the residence time addresses the problem of spatial and temporal consistency, which are mandatory to obtain acceptable results. The way to preserve consistency, specifically for reversed time simulation, was explained in detail.

The adjoint method has strong advantages over other methods to compute the residence time, and it should help significantly doing physical diagnoses. However, its implementation is more complex due to the integration backward in time and boundary aspects. This article is a complement to Delhez *et al.* (2004b) and should help the modeller to compute the residence time distribution in any domain without any critical issue.

Acknowledgements

Sébastien Blaise is a Research fellow with the Belgian Fund for Research in Industry and Agriculture (FRIA). Richard Comblen and Eric Deleersnijder are respectively Research fellow and Research associate with the Belgian National Fund for Scientific Research (FNRS). Eric Delhez is honorary Research Associate with the Belgian National Fund for Scientific Research. Anouk de Brauwere is a postdoctoral researcher at the Research Foundation Flanders (FWO-Vlaanderen). The present study was carried out within the scope of the project "A second-generation model of the ocean system", which is funded by the *Communauté Francaise de Belgique*, as *Actions de Recherche Concertées*, under contract ARC 04/09-316, and the project "Tracing and Integrated Modelling of Natural and Anthropogenic Effects on Hydrosystems" (TIMOTHY), an *Interuniversity Attraction Pole* (IAP6.13) funded by the *Belgian Federal Science Policy Office* (BELSPO). This work is a contribution to the development of SLIM, the Second-generation Louvain-la-Neuve Ice-ocean Model (http://www.climate.be/SLIM). The authors are indebted to Emmanuel Hanert and Olivier Gourgue for their useful comments.

Appendix A: Derivation of the two-dimensional residence time equation

The equation (1) for the depth-averaged residence time can be derived by adapting the procedure introduced in Delhez *et al.* (2004b) in the context of a three-dimensional model.

In the context of two-dimensional depth-integrated model, the (mean) residence time in a control domain ω at a particular location $\boldsymbol{x}_0$ and a given time t_0 is given by

$$\theta(t_0, \boldsymbol{x}_0) = \int_{t_0}^{\infty} \left(\iint_{\omega} H(t, \boldsymbol{x}) C(t, \boldsymbol{x}) d\boldsymbol{x} \right) dt \tag{20}$$

where $C(t, \boldsymbol{x})$ denotes the concentration field produced by a unit point discharge at $\boldsymbol{x}_0$ at time t_0 and where H is the total water depth (which is the sum of the surface elevation and the reference water depth).

In a direct approach, C is obtained by solving the advection-diffusion problem

$$\begin{cases} \dfrac{\partial (HC)}{\partial t} + \nabla \cdot (H \mathbf{u} C) = \nabla \cdot (\kappa H \nabla C) & \\ H(t_0, \boldsymbol{x}) C(t_0, \boldsymbol{x}) = \delta(\boldsymbol{x} - \boldsymbol{x}_0) & \\ C = 0 & \text{at the open boundaries of } \omega, \\ \boldsymbol{n} \cdot \kappa H \nabla C = 0 & \text{at material boundaries of } \omega, \end{cases} \tag{21}$$

where $\mathbf{u}$ and κ denote respectively the depth-averaged horizontal velocity and the diffusivity and where δ is the Dirac impulse function. Using this approach, the direct problem (21) must be solved for a variety of initial conditions corresponding to the times and locations at which the residence time is sought, which can be very demanding in computer resources.

An alternative and more efficient procedure can be derived by considering the adjoint of (21). To this end, we define the adjoint variable $C_T^\star$ as the solution of the differential problem

$$\begin{cases} H \dfrac{\partial C_T^\star}{\partial t} + H \mathbf{u} \cdot \nabla C_T^\star + \nabla \cdot (\kappa H \nabla C_T^\star) = 0 & \\ C_T^\star(T, \boldsymbol{x}) = 1 & \text{in } \omega, \\ C_T^\star = 0 & \text{at the open boundaries of } \omega, \\ \boldsymbol{n} \cdot \kappa H \nabla C_T^\star = 0 & \text{at material boundaries of } \omega. \end{cases} \tag{22}$$

where T denotes some fixed time horizon.

Using (21) and (22), it is easy to show that (see Delhez *et al.*, 2004b)

$$C_T^\star(t_0, \boldsymbol{x}_0) = \iint_\omega H(T, \boldsymbol{x}) C(T, \boldsymbol{x}) d\boldsymbol{x} \tag{23}$$

so that the adjoint variable can be interpreted as the amount of the tracer considered in the direct problem that is still present in the control domain at time T, *i.e.* the fraction of the mass of the tracer released at time t_0 and location $\boldsymbol{x}_0$ with a residence time larger than $T - t_0$. One has therefore

$$\theta(t_0, \boldsymbol{x}_0) = \int_{t_0}^\infty C_t^\star(t_0, \boldsymbol{x}_0) dt = \int_0^\infty D(t_0, \tau, \boldsymbol{x}_0) d\tau \tag{24}$$

where we introduced the cumulative distribution function

$$D(t_0, \tau, \boldsymbol{x}_0) = C_{t_0+\tau}^\star(t_0, \boldsymbol{x}_0) \tag{25}$$

With this definition and using the depth-integrated continuity equation

$$\frac{\partial H}{\partial t} + \nabla \cdot (H \mathbf{u}) = 0 \tag{26}$$

it is easy to show from (22) that D satisfies the differential equation

$$\frac{\partial HD}{\partial t} - \frac{\partial HD}{\partial \tau} + \nabla \cdot (H \mathbf{u} D) + \nabla \cdot (\kappa H \nabla D) = 0 \tag{27}$$

and the auxiliary condition

$$D(t, 0, \boldsymbol{x}) = 1 \qquad \text{in } \omega. \tag{28}$$

Integrating (27) with respect to τ and assuming that $D(t, \tau, \boldsymbol{x})$ decreases to zero when τ tends to infinity, *i.e.* that all the particles are eventually flushed out of the control domain, one gets finally

$$\frac{\partial H\theta}{\partial t} + H + \nabla \cdot (H \mathbf{u} \theta) + \nabla \cdot (\kappa H \nabla \theta) = 0 \tag{29}$$

which is the differential equation for the (mean) depth-averaged residence time in ω.

Appendix B: Constraint on the mesh Peclet number

Starting from equation (6), we will solve the steady-state, one-dimensional problem defined in section 3 by means of a finite difference scheme.

The domain is discretised by N finite difference nodes of indices $n = 1 \rightarrow N$, whose locations are defined by $\tilde{x}_n = (n - 1/2)/N$. The grid resolution is then defined by $\Delta\tilde{x} = 1/N$. The discrete residence time at these points is noted $\tilde{\theta}^h_n$, where h refers to the approximate value of the variable. Two fictive points are added beyond both boundaries of the domain (i.e. at $\tilde{x}_0 = -1/(2N)$ and $\tilde{x}_{N+1} = 1 + 1/(2N)$) whose values will be noted $\tilde{\theta}^h_0$ and $\tilde{\theta}^h_{N+1}$. These points will be useful to enforce the Dirichlet boundary conditions, as no grid point is defined on the boundary. The second order centered finite-difference discretisation of the non-dimensional form of equation (6) yields

$$\frac{1}{Pe}\frac{\tilde{\theta}^h_{n+1} - 2\tilde{\theta}^h_n + \tilde{\theta}^h_{n-1}}{\Delta\tilde{x}^2} + \frac{\tilde{\theta}^h_{n+1} - \tilde{\theta}^h_{n-1}}{2\Delta\tilde{x}} + 1 = 0, \qquad n = 1, 2 \dots N. \tag{30}$$

Boundary conditions, which consist in a zero residence time at each boundary, are enforced by imposing

$$\begin{aligned} \frac{\tilde{\theta}^h_0 + \tilde{\theta}^h_1}{2} &= 0, \\ \frac{\tilde{\theta}^h_N + \tilde{\theta}^h_{N+1}}{2} &= 0. \end{aligned} \tag{31}$$

The solution of the discrete problem defined by (30) and (31) is of the form

$$\tilde{\theta}^h_n = Ar^n + Bn + C \tag{32}$$

where

$$r = \frac{2 - Pe\Delta\tilde{x}}{2 + Pe\Delta\tilde{x}}, \tag{33}$$

$$A = \frac{2}{(1 + r)(r^N - 1)}, \tag{34}$$

$$B = -\frac{1}{N}, \tag{35}$$

$$C = \frac{1}{1 - r^N} + \frac{1}{2N}. \tag{36}$$

The constant r then satisfies

$$-1 < r < 1. \tag{37}$$

When the mesh Peclet number $Pe^h = Pe\Delta\tilde{x}$ is higher than 2, the constant r is negative, and a spurious oscillating oscillating mode appears in the solution (32). In dimensional variables, the critical factor Pe^h becomes $Pe\Delta x/L$. It can be written as $\Delta x/(LPe^{-1})$, i.e. the mesh size divided by the thickness of the boundary layer.

Appendix C: Influence of the boundary condition on the oscillations

Starting from the non-dimensional finite-difference discretisation of the residence time (30), the parameterisation of the boundary layer (12) is now applied to the inflow boundary, while a Dirichlet boundary condition is still used at the outflow boundary:

$$\begin{aligned} \frac{\tilde{\theta}_1^h - \tilde{\theta}_0^h}{\Delta\tilde{x}} &= \frac{e^{-Pe\frac{L^*}{L}}}{1-e^{-Pe\frac{L^*}{L}}} Pe \left(\frac{\tilde{\theta}_1^h + \tilde{\theta}_0^h}{2} + \frac{L^*}{L} \right) - 1, \\ \frac{\tilde{\theta}_N^h + \tilde{\theta}_{N+1}^h}{2} &= 0. \end{aligned} \tag{38}$$

The solution of the discrete problem is still of the form (32). However, due to the different boundary conditions, the coefficients modify to:

$$\begin{aligned} A &= \frac{2Pe(1+\frac{L^*}{L})}{Pe(1+r)(r^N-1)+2N(e^{\frac{L^*}{L}Pe}-1)(r-1)}, \\ B &= -\frac{1}{N}, \\ C &= \frac{2N(e^{\frac{L^*}{L}Pe}-1)(r-1)(1+2N)-Pe(1+r)\left[1+2N+r^T(2\frac{L^*}{L}N-1)\right]}{2N\left[Pe(1+r)(r^N-1)+2N(e^{\frac{L^*}{L}Pe}-1)(r-1)\right]}. \end{aligned} \tag{39}$$

When the mesh Peclet number $Pe\Delta\tilde{x}$ is higher than 2, the oscillating mode is still present. The amplitude of the oscillations is controlled by the constant A. Figure 10 shows that if we use a Dirichlet inflow boundary condition, the norm of this constant will increase with the mesh Peclet number. If the mesh Peclet number is high, the solution will inevitably show significant oscillations. If the parameterisation of the inflow boundary layer is used with a sufficiently large $\frac{L^*}{L}$, the oscillatory part of the solution is limited and decreases as the mesh Peclet number increases (Figure 10). This is due to the fact that, for a high mesh Peclet number, the boundary layer is entirely comprised in the parameterised zone. The parameterisation used with $\frac{L^*}{L} = 0$ produces the same results as the Dirichlet boundary condition. It is then necessary to use a sufficiently large value of $\frac{L^*}{L}$ to limit the oscillating part of the solution.

Figure 10: Evolution of the constant A from equation (32) with the mesh Peclet number $Pe\Delta\tilde{x}$ for the stationary one-dimensional problem. Results obtained using a Dirichlet boundary condition (plain line) and the parameterisation of the inflow boundary layer (dotted lines). The values along the curves indicate different parameterised length L^*/L used for the parameterisation of the boundary layer. The dashed line indicates a mesh Peclet number of 2 under which the solution does not present any oscillation. The number of nodes $N = 10$.

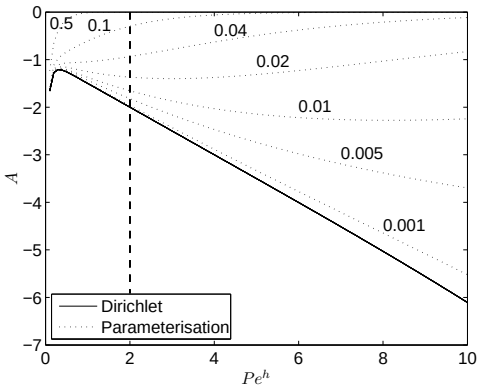

References

Allen, C. M. 1982. Numerical Simulation of Contaminant Dispersion in Estuary Flows. Royal Society of London Proceedings Series A, 381:179–194.

Arega, F., Armstrong, S., and Badr, A. 2008. Modeling of residence time in the East Scott Creek Estuary, South Carolina, USA. Journal of Hydro-environment Research, 2(2):99 – 108.

Black, K. P. and Gay, S. L. 1987. Eddy Formation in Unsteady Flows. Journal of Geophysical Research, 92(C9):9514–9522.

Blumberg, A. F. and Mellor, G. L. 1987. A description of three-dimensional coastal ocean circulation model. In Heaps, N. S., editor, *Three Dimensional Coastal Ocean Model*, pages 1–16. American Geophysical Union.

Bolin, B. and Rhode, H. 1973. A note on the concepts of age distribution and residence time in natural reservoirs. Tellus, 25:58–62.

Burchard, H. 2002. *Applied Turbulence Modelling in Marine Waters*. Number 100 in Lecture Notes in Earth Science. Springer.

Combescure, A., Gravouil, A., Baietto-Dubourg, M.-C., Elguedj, E., Ribeaucourt, R., and Ferri, E. 2005. Extended finite element method for numerical simulation of 3D fatigue crack growth. In D. Dowson, G. D., M. Priest and Lubrecht, A., editors, *Life Cycle Tribology - Proceedings of the 31st Leeds-Lyon Symposium on Tribology Held at Trinity and All Saints College, Horsforth, Leeds, UK 7th–10th September 2004*, volume 48 of *Tribology and Interface Engineering Series*, pages 323 – 328. Elsevier.

Comblen, R., Lambrechts, J., Remacle, J.-F., and Legat, V. 2009. Practical evaluation of five part-discontinuous finite element pairs for the non-conservative shallow water equations. International Journal for Numerical Methods in Fluids. , doi:10.1002/fld.2094.

de Brye, B., de Brauwere, A., Gourgue, O., Kärna, T., Lambrechts, J., Comblen, R., and Deleersnijder, E. 2009. A Finite-Element, Multi-Scale Model of the Scheldt Tributaries, River, Estuary and ROFI. Coastal Engineering, submitted.

Deleersnijder, E. and Delhez, E. J., editors. 2007. *Timescale- and tracer-based methods for understanding the results of complex marine models*, volume 74, 585-776 (Special issue). Estuarine, Coastal and Shelf Science.

Deleersnijder, E., Campin, J.-M., and Delhez, E. J. M. 2001. The concept of age in marine modelling: I. Theory and preliminary model results. Journal of Marine Systems, 28(3-4):229 – 267.

Delhez, E. J., Lacroix, G., and Deleersnijder, E. 2004a. The age as a diagnostic of the dynamics of marine ecosystem models. Ocean Dynamics, 54(2):221 – 231.

Delhez, E. J. M. 2006. Transient residence and exposure times. Ocean Science, 2(1):1–9.

Delhez, E. J. M. and Deleersnijder, E. 2006. The boundary layer of the residence time. Ocean Dynamics, 56:139–150.

Delhez, E. J. M., Heemink, A. W., and Deleersnijder, E. 2004b. Residence time in a semi-enclosed domain from the solution of an adjoint problem. Estuarine, Coastal and Shelf Science, 61:691–702.

Egbert, G. D., Benett, A. F., and Foreman, M. G. G. 1994. TOPEX/POSEIDON tides estimated using a global inverse model. Journal of Geophysical Research, 99:24,821–24,852.

Fares, E. and Schröder, W. 2002. A differential equation for approximate wall distance. International Journal for Numerical Methods in Fluids, 39:743–762.

Garabedian, P. R. 1964. *Partial Differential Equations*. John Wiley & Sons, Inc., New York.

Gourgue, O., Deleersnijder, E., and White, L. 2007. Toward a generic method for studying water renewal, with application to the epilimnion of Lake Tanganyika. Estuarine, Coastal and Shelf Science, 74:764–776.

Hanert, E., Deleersnijder, E., Blaise, S., and Remacle, J.-F. 2007. Capturing the bottom boundary layer in finite element ocean models. Ocean Modelling, 17:153–162.

Kalnay, E., Kanamitsu, M., Kistler, R., Collins, W., Deaven, D., Gandin, L., Iredell, M., Saha, S., White, G., Woollen, J., Zhu, Y., Leetmaa, A., Reynolds, B., Chelliah, M., Ebisuzaki, W., Higgins, W., Janowiak, J., Mo, K. C., Ropelewski, C., Wang, J., Jenne, R., and Joseph, D. 1996. The NCEP/NCAR 40-Year Reanalysis Project. Bulletin of the American Meteorological Society, 77:437–472.

Liu, W.-C., Chen, W.-B., Kuo, J.-T., and Wu, C. 2008. Numerical determination of residence time and age in a partially mixed estuary using three-dimensional hydrodynamic model. Continental Shelf Research, 28(8):1068 – 1088.

Luther, K. H. and Haitjema, H. M. 1998. Numerical experiments on the residence time distributions of heterogeneous groundwatersheds. Journal of Hydrology, 207(1-2):1 – 17.

Miller, S. D. and Luther, M. E. 2008. A Numerical Simulation of Residual Circulation in Tampa Bay. Part II: Lagrangian Residence Time. Estuaries and Coasts, 31:815–827.

Moës, N., Dolbow, J., and Belytschko, T. 1999. A finite element method for crack growth without remeshing. International Journal for Numerical Methods in Engineering, 46:131–150.

Monsen, N. E., Cloern, J. E., Lucas, L. V., and Monismith, S. G. 2002. A comment on the use of flushing time, residence time, and age as transport time scales. Limnology and oceanography, 47:1545–1553.

Nauman, E. B. 1981. Residence time distributions in systems governed by the dispersion equation. Chemical Engineering Science, 36(6):957 – 966.

Pawlowicz, R., Beardsley, B., and Lentz, S. 2002. Classical tidal harmonic analysis including error estimates in MATLAB using T_TIDE. Computers and Geosciences, 28:929–937.

Soetaert, K. and Herman, P. M. J. 1995. Estimating estuarine residence times in the Westerschelde (The Netherlands) using a box model with fixed dispersion coefficients. Hydrobiologia, 311:215–224.

Spivakovskaya, D., Hemink, A. W., and Deleersnijder, E. 2007. Lagrangian modelling of multi-dimensional advection-diffusion with space-varying diffusivities: theory and idealized test cases. Ocean Dynamics, 57:189 – 203.

Steen, R. J. C. A., Evers, E. H. G., Hattum, B. V., Cofino, W. P., and Brinkman, T. U. A. 2002. Net fluxes of pesticides from the Scheldt Estuary into the North Sea: a model approach. Environmental Pollution, 116(1):75 – 84.

Takeoka, H. 1984. Fundamental concepts of exchange and transport time scales in a coastal sea. Continental Shelf Research, 3(3):311 – 326.

Tartinville, B., Deleersnijder, E., and Rancher, J. 1997. The water residence time in the Mururoa atoll lagoon: sensitivity analysis of a three-dimensional model. Coral Reefs, 16:193–203.

Wang, C.-F., Hsu, M.-H., and Kuo, A. Y. 2004. Residence time of the Danshuei River estuary, Taiwan. Estuarine, Coastal and Shelf Science, 60(3):381 – 393.

White, L., Legat, V., and Deleersnijder, E. 2008. Tracer Conservation for Three-Dimensional, Finite-Element, Free-Surface, Ocean Modeling on Moving Prismatic Meshes. Monthly Weather Review, 136:420–442.

Wyart, E., Duflot, M., Coulon, D., Martiny, P., Pardoen, T., Remacle, J.-F., and Lani, F. 2008. Substructuring FE-XFE approaches applied to three-dimensional crack propagation. Journal of Computational and Applied Mathematics, 215(2):626 – 638.

Zimmerman, J. T. F. 1976. Mixing and flushing of tidal embayments in the western dutch Wadden Sea. Part I: distribution of salinity and calculation of mixing time scales. Netherlands Journal of Sea Research, 10:149–191.

Chapter 3

Density gradient in estuarine models

A three-dimensional model is described by Chapter 1, while Chapter 2 presents two-dimensional simulations performed on the Scheldt estuary. Becoming more and more complex, two-dimensional and three-dimensional models results can be difficult to interpret and diagnostic variables like the residence time can be needed. These models are also long to configure for a specific application and require generally a lot of data sets (bathymetry and coasts, forcings,...), especially when there is a baroclinic components (salt and temperature). A strong simplification is to use one-dimensional models. When the physics is mainly one-dimensional (horizontal or vertical), these models can be fast to set up and lead to results that are easy to interpret. Furthermore, the computational time is generally much smaller using one-dimentional models. These models can then be used for preliminary studies to provide a quick idea of the physics before performing more complex simulations. However, this dimensional simplification adresses the need of parameterisations for phenomena which do not occur in the one-dimensional model space.

The next article (Blaise and Deleersnijder, 2008) introduces a new parameterisation of the horizontal density gradient in a one-dimensional baroclinic water column model applied to an estuary. In the absence of more complete data, this density gradient is estimated from upstream and downstream density. However, being used as a forcing term in the momentum equation, it has a strong impact on the results and can influence the stability of the model. It is then useful to develop some parameterisations that ensure the model to remain stable, and constraint the model output to physically acceptable values. Such a parameterisation is developed in the following article. It is shown that short analytical developments can be used to obtain the above mentioned properties.

Although these developments are related exclusively to one-dimensional models, the underlying method can be used in parameterisations applied to

models of higher dimension. It is worth noticing that a one-dimensional model implies several hypothesis which must be verified before using it. Some important phenomena could not be represented by a one-dimensional model and be missed by the user of such a model. Moreove, these phenomena could modify the one-dimensional flow, which would make the model results wrong if they are not taken into account. It is generally useful to verify the typical configuration of the considered domain of interest with a three-dimensional model or data to validate the one-dimensional simplification.

Improving the parameterisation of horizontal density gradient in one-dimensional water column models for estuarine circulation

Sébastien Blaise[1] and E. Deleersnijder[2]

[1]Université catholique de Louvain,
Unité de Génie Civil et Environnemental,
B-1348 Louvain-la-Neuve, Belgium

[2]Université catholique de Louvain,
Centre for Systems Engineering and Applied Mechanics (CESAME)
B-1348 Louvain-la-Neuve, Belgium

E-mail: sebastien.blaise@uclouvain.be

Originally published in Ocean Science, 4, 239-246 (2008)

Abstract

A new parameterisation of horizontal density gradient for a one-dimensional water column estuarine model, inspired by the first-order finite-difference upwind scheme, is presented. This parameterisation prevents stratification from growing indefinitely, a deficiency usually referred to as "runaway stratification". It is seen that, using this upwind-like parameterisation, the salinity must remain comprised between upper and lower bounds set a priori and that any initial over- or under-shooting is progressively eliminated. Simulations of idealised and realistic estuarine regimes indicate that the new parameterisation lead to results that are devoid of the runaway stratification phenomenon, as opposed to previously used models.

1 Introduction

Estuaries and their regions of freshwater influence (ROFIs) have been studied for a long time. They exhibit strong gradients of several variables: salinity, temperature, plankton and nutrient concentrations can vary over a wide range of values, strongly impacting physical and biological processes. For instance, complex dynamics, influenced by tides and input of freshwater from rivers, have a strong influence on the growth of phytoplankton (Lucas *et al.*, 1998, 1999).

This work focuses on estuarine dynamics, especially on the evolution of stratification. The latter is a key player in vertical mixing, which influences directly the vertical fluxes of heat, salt, momentum and nutrients (Simpson *et al.*, 1990). Many studies were devoted to the evolution of stratification in estuaries. They firstly described *in situ* observations gathered from field surveys (Sharples and Simpson, 1993; Stacey and Monismith, 1999), showing that the dynamics is mainly driven by the tidal flow, associated with a density driven circulation generated by an input of freshwater from rivers. This was reproduced in laboratory experiments by Linden and Simpson (1986, 1988), who focused on the mechanisms influencing stratification. These mechanisms were described in detail by Simpson *et al.* (1990). Several models were applied to simulate and understand the evolution of stratification in estuaries. Linear prescriptive models were first used (Simpson *et al.*, 1991; Nunes Vaz and Simpson, 1994; Scott, 2004). Then, several authors turned to one-dimensional water column non linear models (Monismith *et al.*, 1996; Monismith and Fong, 1996; Nunes Vaz and Simpson, 1994; Lucas *et al.*, 1998). Recently, three-dimensional models were used to simulate estuarine flows (Burchard and Baumert, 1998; Hetland and Geyer, 2004; Warner *et al.*, 2005).

One-dimensional non linear models can be very useful to understand and predict the evolution of stratification in an estuary. They are light and simple to build. They require a minimal amount of data and parameters. Furthermore, they generate simple results, which permits to easily understand the key processes and quickly establish diagnoses. However, one common failure of these models is the generation of runaway stratification : when the tidal amplitude is low, stratification tends to grow without bound due to an inadequate parameterisation of horizontal density gradient (Nunes Vaz and Simpson, 1994; Monismith *et al.*, 1996; Warner *et al.*, 2005). This paper shows that simple analytical developments can lead to a new version of the model which keeps stratification under control. It is also seen that, in the long run, the model is insensitive to an unrealistic initial stratification.

Herein we use a one-dimensional finite-element water column model. Such finite-element models and their advantages were described by Hanert *et al.* (2006, 2007). As mixing is a key player in the evolution of the stratification (Nunes Vaz and Simpson, 1994), we use the Mellor and Yamada level 2.5 turbulence closure (Mellor and Yamada, 1974, 1982; Galperin *et al.*, 1988) which is well suited for the prediction of stratification in estuaries (Nunes Vaz and Simpson, 1994). This turbulence closure was recently implemented using the finite-element method for one-dimensional (Hanert *et al.*, 2006) and three-dimensional (Blaise *et al.*, 2007) models.

The physical setting is described in section 2. Then, in section 3, the model is presented. Two parameterisations of horizontal density gradient, the classical one and a new one, are introduced in section 4 and it is seen rigorously that the new approach prevents stratification from running away. This is illustrated by numerical results in section 5. Section 6 examines the sensitivity of the model to the initial stratification and the influence of the parameteri-

Figure 1: Physical setting: the stratification is to be simulated in the water column located at point C. The latter is located in a region of high salinity gradient. Its order of magnitude is $(S_s - S_r)/2L$, where S_s and S_r denote the downstream and the upstream salinity, respectively.

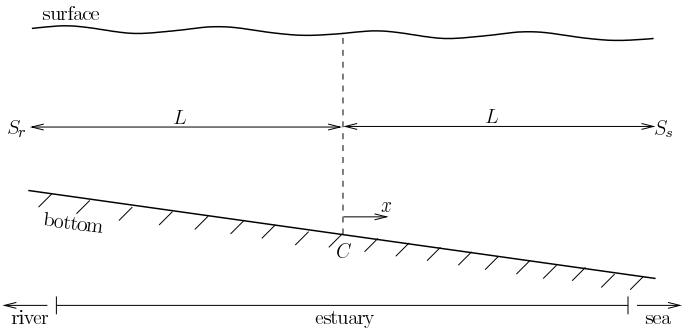

sation of the horizontal salinity gradient in the momentum equation. Finally, conclusions are drawn in section 7.

2 Physical setting

We will study the stratification in an estuary, which is generated by the front between freshwater and salty seawater. This front is of a crucial importance for the dynamics of the estuary, notably for the vertical density gradient. Therefore, we will consider a water column located at C in Fig. 1, at a distance L to the sea limit. We assume that the salinity at a distance L upstream of C is of the order of S_r and that the salinity at the sea limit is of the order of S_s. We also assume that S_r and S_s are constants satisfying the following condition:

$$S_r < S_s. \tag{1}$$

In such a configuration, the water velocity is mainly caused by two processes (Simpson *et al.*, 1990):

- The presence of freshwater originating from the river creates a density front with the salty seawater (Fig. 2a). This front induces a circulation, with light freshwater going towards the sea at the surface, and dense water going towards the river near the bottom. Due to the bottom friction, this circulation is reduced near the sea bottom.

- The tidal circulation, influenced by the shear stress due to the bottom friction, generates a logarithmic-like velocity profile (Fig. 2b). This profile induces a transport of freshwater varying over the water column, leading to stratification. The succession of ebbs/floods generates a

Figure 2: Circulation induced (a) by the freshwater input generating a front with the dense seawater and (b) by tides (here at falling tide), as described by Simpson *et al.* (1990).

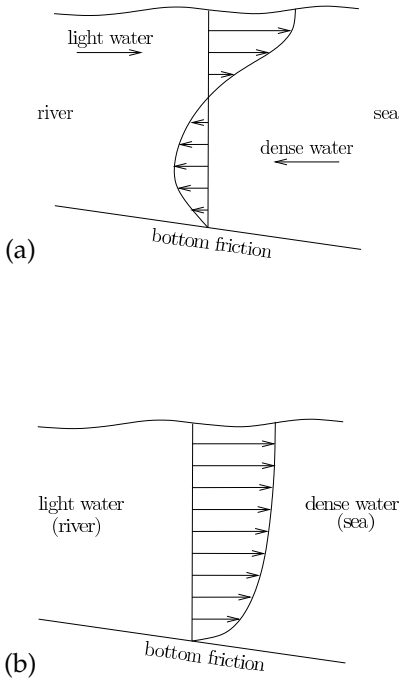

Strain-Induced Periodic Stratification (SIPS) regime, which can be described as follows: during falling tide, a stable stratification develops, which is reduced by mixing at the end of the falling tide. During rising tide, the salinity profile is unstable and is quickly mixed over the vertical, leading to a non stratified water column. Due to the tidal velocity asymmetry, the velocity profile is different at ebb and flood tides (Jay and Musiak, 1994). The mixing near the bottom is indeed enhanced at flood tides, due to the unstable stratification resulting from the quick displacement of salty water over slow freshwater or brackish (Burchard and Baumert, 1998). This high near-bottom mixing at flood tides leads to higher bottom velocities during rising tides than during falling tides, which has the effect of increasing the stratification.

The combination of these processes can generate different flow regimes. If the tides are dominant, the SIPS regime prevails. When the effect of the horizontal

density gradient becomes important compared to the tidal effect, the tidal mixing is not sufficient to annihilate the stratification; this stratification strengthens during each tidal cycle, inducing a persistent stratification regime (Lucas *et al.*, 1998). The presence of different non-synchronous tidal components, by generating an alternation of spring/neap tides, can lead to a succession of SIPS and permanent stratification periods (Simpson *et al.*, 1990; Sharples and Simpson, 1993; Nunes Vaz and Simpson, 1994; Monismith *et al.*, 1996).

3 Model description

The model used herein is based on that of Lucas *et al.* (1998) and Monismith *et al.* (1996). For the flow under study, the impact on density of temperature variations is negligible compared with those of salinity. Therefore, density is assumed to be a function of salinity only and the following equations will be expressed in terms of salinity. As in Lucas *et al.* (1998) and Monismith *et al.* (1996), a linear equation of state is adopted:

$$\rho = \rho_0 \left(1 + \beta(S - S_0)\right), \tag{2}$$

where ρ and S are the density and the salinity, whose reference values are denoted ρ_0 and S_0, respectively; $\beta = 7.6 \cdot 10^{-4}\ psu^{-1}$ is the salinity expansion coefficient, which is assumed to be constant.

If x is the horizontal coordinate increasing toward the sea, the along-estuary horizontal velocity $u(t, z)$ at location C obeys the following momentum equation:

$$\frac{\partial u}{\partial t} = -g\frac{\partial \eta}{\partial x} - g\beta\frac{\partial S}{\partial x}\left(-z + \gamma\frac{H}{2}\right) + \frac{\partial}{\partial z}\left(\nu\frac{\partial u}{\partial z}\right), \tag{3}$$

where g, η, z and H are the gravitational acceleration, the sea surface elevation, the vertical coordinate pointing upwards with its origin at the sea surface and the constant water depth, respectively. The effect of Earth rotation is neglected. The surface stress and bottom velocity are equal to zero. The turbulent viscosity ν is calculated by means of the Mellor and Yamada level 2.5 turbulence closure (Mellor and Yamada, 1974, 1982) implemented in its quasi-equilibrium version (Galperin *et al.*, 1988; Deleersnijder and Luyten, 1994). The surface slope due to the barotropic tides can be represented as

$$-g\frac{\partial \eta}{\partial x} = \sum_i U_{i,max}\left(\frac{2\pi}{T_i}\right)\cos\left(\frac{2\pi}{T_i}t\right) \tag{4}$$

in which T_i is the tide period and $U_{i,max}$ the maximum velocity for the i-th tidal component. The baroclinic pressure gradient can be divided into two contributions (Lucas *et al.*, 1998; Monismith *et al.*, 1996): a term derived from the horizontal salinity gradient, $g\beta\frac{\partial S}{\partial x}z$, and a term derived from the surface slope generated by the baroclinic flow, $-g\beta\frac{\partial S}{\partial x}\gamma\frac{H}{2}$. The dimensionless coefficient γ is to be tuned in such a way that the residual transport is zero, *i.e.*

the average over a tidal cycle of the depth-integrated velocity vanishes. Practically, γ is found iteratively to minimize this velocity (Lucas *et al.*, 1998). It is possible to impose a prescribed mean velocity, and in this way take into account the effect of residual run-off from the river (Burchard, 1999), but this was not done in the present paper.

The salinity S obeys the equation

$$\frac{\partial S}{\partial t} = -u\frac{\partial S}{\partial x} + \frac{\partial}{\partial z}\left(\lambda\frac{\partial S}{\partial z}\right), \tag{5}$$

where the eddy diffusivity λ is obtained from the same turbulence closure model as the eddy viscosity. The surface and bottom salinity fluxes are prescribed to be zero:

$$\left[\lambda\frac{\partial S}{\partial z}\right]_{z=-H,0} = 0. \tag{6}$$

4 Parameterisation of the horizontal salinity gradient

In the previous governing equations, most authors (Nunes Vaz and Simpson, 1994; Lucas *et al.*, 1998; Monismith *et al.*, 1996; Monismith and Fong, 1996) assumed the horizontal salinity gradient to be a constant that was evaluated as follows:

$$\frac{\partial S}{\partial x} = \tau, \tag{7}$$

where $\tau = \frac{S_s - S_r}{2L}$. In some situations (e.g. for some idealised studies or when it is in accordance with observations), it is a good choice to prescribe the salinity gradient as a constant. However, this parameterisation has been identified as the cause of the so-called "runaway stratification", a phenomenon in which stratification increases indefinitely (Warner *et al.*, 2005). The salinity reaches values that are no longer comprised in the interval $[S_r, S_s]$, which is unacceptable. By annihilating vertical mixing, this overestimated stratification corrupts the computation of the evolution of velocity and water properties.

This complication is related to the variation of the forcing terms over the water column in the momentum equation (3). Figure 3 shows that, when averaged over a tidal cycle, the sum of each forcing term present in (3) decreases linearly with depth. This variation over the vertical will lead to a seaward tidally-averaged velocity greater in the upper part of the water column than near the bottom. With such a distribution of the velocity, it is obvious that the use of a constant salinity gradient in (5) will inevitably lead to a constantly increasing stratification if mixing is not taken into account. Indeed, at falling tide, the advection of freshwater will decrease with depth whereas, at rising tide, the advection of seawater will increase with depth, causing stratification to grow indefinitely. The turbulent mixing can counterbalance this phenomenon and stabilize the stratification, especially at the end of rising tide when its effect surpasses the effect of advection. At falling tide, the mixing is

Figure 3: Vertical profiles of the tidally-averaged forcing terms appearing in the momentum equation (3). The resulting forcing varies linearly with depth.

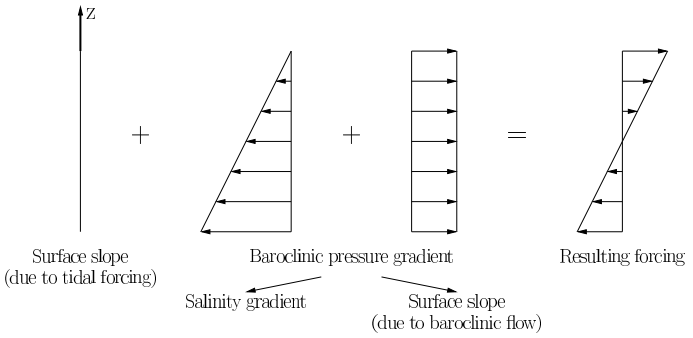

intense due to the low or unstable stratification, contributing to a non stratified water column. However, if turbulent mixing is not sufficient, the water column will stratify indefinitely.

The apparition of "runaway stratification" can be avoided by using an alternative parameterisation of the horizontal salinity gradient, inspired by the first-order upwind difference scheme:

$$\frac{\partial S}{\partial x} = \begin{cases} \frac{S-S_r}{L} & \text{if } u \geq 0, \\ \frac{S_s-S}{L} & \text{if } u < 0. \end{cases} \tag{8}$$

By introducing u^+ and u^- the positive and negative parts of the longitudinal velocity,

$$u^{\pm} = \frac{u \pm |u|}{2}, \tag{9}$$

and by using relation (8), we can rewrite equation (5) as

$$\frac{\partial S}{\partial t} = -u^+ \frac{S - S_r}{L} - \left|u^-\right| \frac{S - S_s}{L} + \frac{\partial}{\partial z}\left(\lambda \frac{\partial S}{\partial z}\right). \tag{10}$$

If the velocity is directed toward the sea ($u > 0$), the first term in the right-hand side of (10) relaxes the salinity to its river value S_r, the relaxation timescale being L/u^+. On the other hand, when the velocity is directed toward the river, the salinity is relaxed toward S_s with a relaxation timescale equal to $L/|u^-|$.

It is interesting to notice that resorting to this new parameterisation is equivalent to add to the classical formulation (7) a horizontal diffusion term. Indeed, with the parameterisation suggested herein, the horizontal salinity advection may be rewritten as (E. Hanert, personal communication, March 2008)

$$-u\frac{\partial S}{\partial x} = -u\frac{S_s - S_r}{2L} + \frac{|u|\,L}{2}\frac{S_s - 2S + S_r}{L^2}. \tag{11}$$

Clearly, the last term in the equation above may be viewed as the discrete form of the harmonic diffusion operator, the associated diffusivity being $|u|\,L/2$.

The interpretation of the role of the first two terms in the right-hand side of salinity equation (10) suggests that, whatever the horizontal velocity, the salinity should tend to be comprised in the interval $[S_r, S_s]$. In fact, this can be demonstrated rigorously. For an arbitrary large value of t ($t \to \infty$), the salinity must obey the following inequalities:

$$S_r \leq S(t,z) \leq S_s, \tag{12}$$

implying that stratification cannot grow out of control. We first define the overshooting of the salinity by

$$\delta^+ = \max\left[0, S(t,z) - S_s\right] \tag{13}$$

So, the overshooting is a positive variable that is equal to $S(t,z) - S_s$ if the salinity is greater than its sea value S_s, and is equal to zero otherwise. Multiplying equation (10) by the overshooting and integrating over the height of the water column yields:

$$\frac{1}{2}\frac{\mathrm{d}}{\mathrm{d}t}\int_{-H}^{0}\left(\delta^+\right)^2\mathrm{d}z = \\ -\int_{-H}^{0}\left[u^+\frac{S-S_r}{L} + \left|u^-\right|\frac{S-S_s}{L}\right]\delta^+\mathrm{d}z - \int_{-H}^{0}\lambda\left(\frac{\partial\delta^+}{\partial z}\right)^2\mathrm{d}z. \tag{14}$$

The manipulations leading to this equation are not trivial, but they are of the same type as those of Appendix C of Deleersnijder *et al.* (2001). All of the terms in the right-hand side of (14) are negative unless the overshooting is zero at every point of the water column. Thus, the quadratic measure of the overshooting tends to zero as time increases, implying that

$$\lim_{t\to\infty}\delta^+ = 0. \tag{15}$$

Combining relations (13) and (15) leads to

$$S(t,z) \leq S_s \quad \text{for } t \to \infty. \tag{16}$$

A similar analysis can be performed for the undershooting $\delta^- = \max\left[0, S_r - S(t,z)\right]$, eventually leading to $S(t,z) \geq S_r$ for $t \to \infty$. Hence, (12) holds valid. *QED*.

Needless to say, it cannot be seen that, when the classical parameterisation (7) is used, the salinity asymptotically remains within the interval $[S_r, S_s]$.

5 Model results

To illustrate the advantages of the parameterisation designed above, we will simulate the situations described in section 2. All of the simulations are achieved using a time-step of 60 seconds. The one-dimensional vertical mesh contains 30 nodes. The main physical parameters are similar to those of Nunes

Vaz and Simpson (1994). The water column depth is $15\ m$, and the values of S_r and S_s are respectively $0\ psu$ and $35\ psu$.

We first consider a SIPS regime similar to that of Nunes Vaz and Simpson (1994). There is only one tidal component with a magnitude of $U_{0,max} = 1\ m/s$ and a period of $T_0 = 12\ h$. The longitudinal constant salinity gradient τ is set to $0.25\ psu/km$. Figure 4 shows that the SIPS regime is quickly established, with an alternation of stratified/unstratified phases. The tidal mixing at the end of the falling tide is sufficient to annihilate stratification. The latter is very similar using both parameterisations of salinity gradient. However, the constant parameterisation (7) leads to higher peaks of stratification while the latter is limited using the new parameterisation (8). These smaller peaks can be explained by the horizontal diffusion added to the model (11) when we use the new parameterisation of salinity gradient. The mean velocity remains rather insensitive to the used parameterisation.

For the SIPS regime simulated above, the two expressions of the salinity gradient led to rather similar results. This is not always the case, especially if a permanently stratified regime is considered, such as that investigated by Nunes Vaz and Simpson (1994). Accordingly, the tidal amplitude is decreased ($U_{0,max} = 0.5\ m/s$) to reduce mixing and the longitudinal salinity gradient is increased ($\tau = 0.3\ psu/km$). All the other parameters remain unchanged. Model results are displayed on Fig. 5. Using the classical parameterisation of the horizontal salinity gradient, the stratification grows out of control to unrealistic values exceeding the imposed bounds, which is the deficiency known as "runaway stratification". As demonstrated in section 4, the stratification remains within the imposed limits when we use the new parameterisation. The slight oscillations show that, even when the stratification is high, it is still influenced by tide. While the classical parameterisation (7) gives useless results, the new parameterisation (8) gives qualitatively realistic results for a large number of tidal cycles.

The spring/neap cycles are now simulated by taking into account two tidal components. The first one has an amplitude of $U_{0,max} = 0.8\ m/s$ and a period of $T_0 = 12.42\ h$; while the second component has an amplitude of $U_{1,max} = 0.46 \cdot U_{0,max}$ and a period of $T_1 = 12\ h$ (Nunes Vaz and Simpson, 1994). Using this combination of tidal components, we generate an alternation of spring and neap tides (Fig. 6). We set the longitudinal constant salinity gradient to the value of $\tau = 0.25\ psu/km$. It is shown on Fig. 6 that both parameterisations represent a spring-neap cycle of stratification. During neap tides, the stratification grows until the tidal amplitude increases at spring tides. Then, the stratification weakens and comes back to a SIPS regime. However, the classical parameterisation leads to unrealistic peaks of stratification, with salinity exceeding the limits imposed by the river and sea salinities. This is a common issue when using expression (7) (i.e. Nunes Vaz and Simpson (1994) in which the difference between bottom and surface density grows during neaps as far as $180\ kg/m^3$). This problem does not occur when the new parameterisation is resorted to.

Figure 4: Simulation of a Strain-Induced Periodic Stratification (SIPS) regime: results obtained using the old (7) (dashed curves) and the new (8) (solid curves) parameterisations of the horizontal salinity gradient. The tidal forcing is characterised by $U_{0,max} = 1\ m/s$ and $T_0 = 12\ h$. The longitudinal salinity gradient is set to $\tau = 0.25\ psu/km$. The bounds of salinity are set to $S_r = 0$ psu and $S_s = 35$ psu. Upper panel: Evolution of the stratification (difference between bottom salinity and surface salinity). Middle panel: Minimum and maximum values of salinity over the water column. Lower panel: Evolution of the depth-averaged velocity. The latter is similar for both parameterisations.

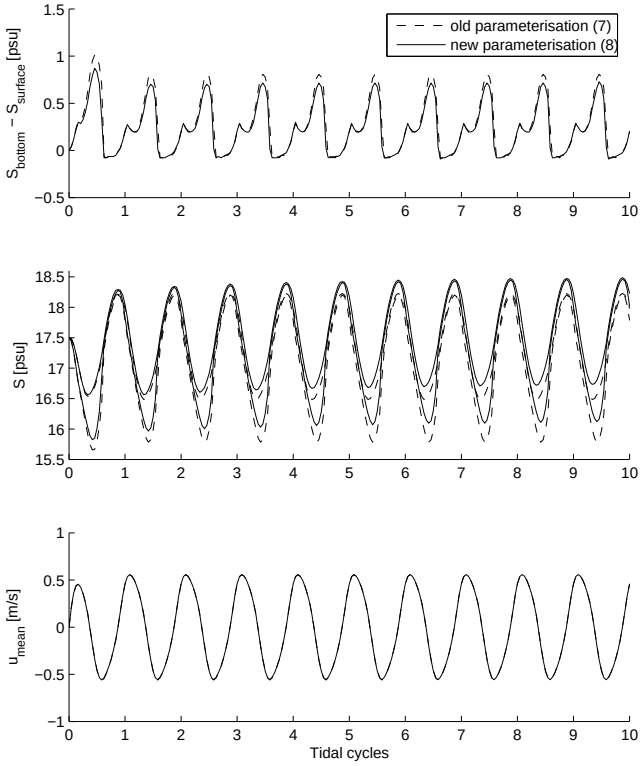

Figure 5: Simulation of a persistent stratification regime: results obtained using the old (7) (dashed curves) and the new (8) (solid curves) parameterisations of the horizontal salinity gradient. The tidal forcing is characterised by $U_{0,max} = 0.5\ m/s$ and $T_0 = 12\ h$. The longitudinal salinity gradient is set to $\tau = 0.3\ psu/km$. The bounds of salinity are set to $S_r = 0$ psu and $S_s = 35$ psu. Upper panel: Evolution of the stratification (difference between bottom salinity and surface salinity). Middle panel: Minimum and maximum values of salinity over the water column. Lower panel: Evolution of the depth-averaged velocity. The latter is similar for both parameterisations.

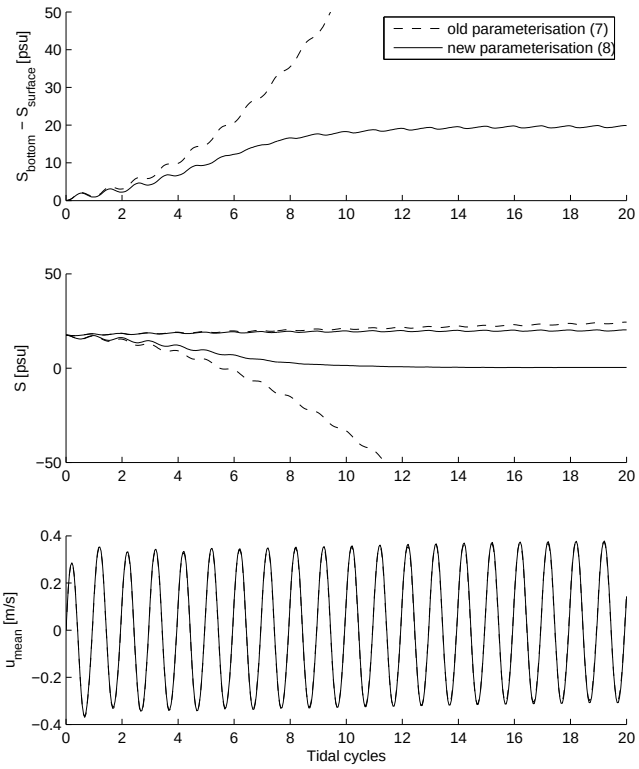

Figure 6: Simulation of the circulation induced by a succession of spring/neap tides: results obtained using the old (7) (dashed curves) and the new (8) (solid curves) parameterisations of the horizontal salinity gradient. The tidal forcing is characterised by $U_{0,max} = 0.8\ m/s$, $T_0 = 12.42\ h$, $U_{1,max} = 0.46 \cdot U_{0,max}$ and $T_1 = 12\ h$. The longitudinal salinity gradient is set to $\tau = 0.25\ psu/km$. The bounds of salinity are set to $S_r = 0$ psu and $S_s = 35$ psu. Upper panel: Evolution of the stratification (difference between bottom salinity and surface salinity). Middle panel: Minimum and maximum values of salinity over the water column. Lower panel: Evolution of the depth-averaged velocity. The latter is similar for both parameterisations.

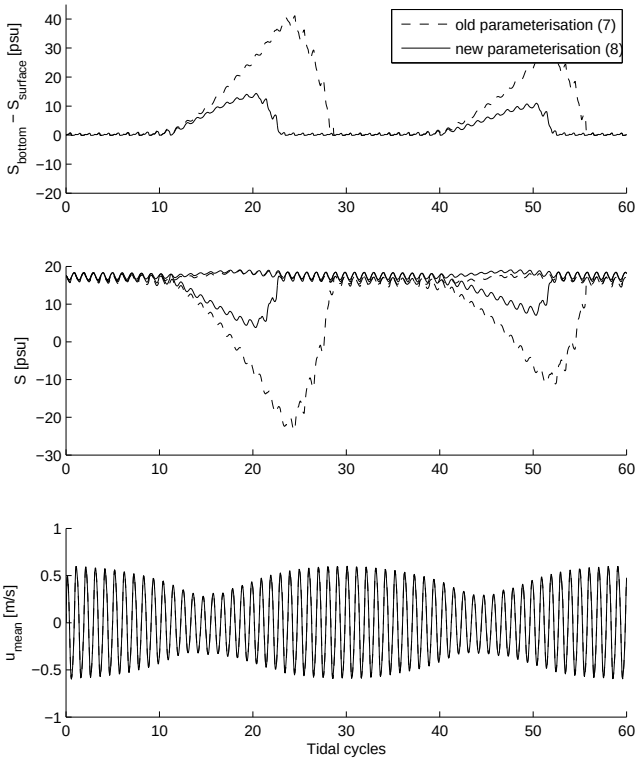

Figure 7: Simulation of the circulation induced by a of succession spring/neap tides: results obtained using the old (7) (dashed curves) and the new (8) (solid curves) parameterisations of the horizontal salinity gradient. The tidal forcing is characterised by $U_{0,max} = 0.7\ m/s$, $T_0 = 12.42\ h$, $U_{1,max} = 0.46 \cdot U_{0,max}$ and $T_1 = 12\ h$. The longitudinal salinity gradient is set to $\tau = 0.3\ psu/km$. The bounds of salinity are set to $S_r = 0$ psu and $S_s = 35$ psu. Upper panel: Evolution of the stratification (difference between bottom salinity and surface salinity). Middle panel: Minimum and maximum values of salinity over the water column. Lower panel: Evolution of the depth-averaged velocity. The latter is similar for both parameterisations.

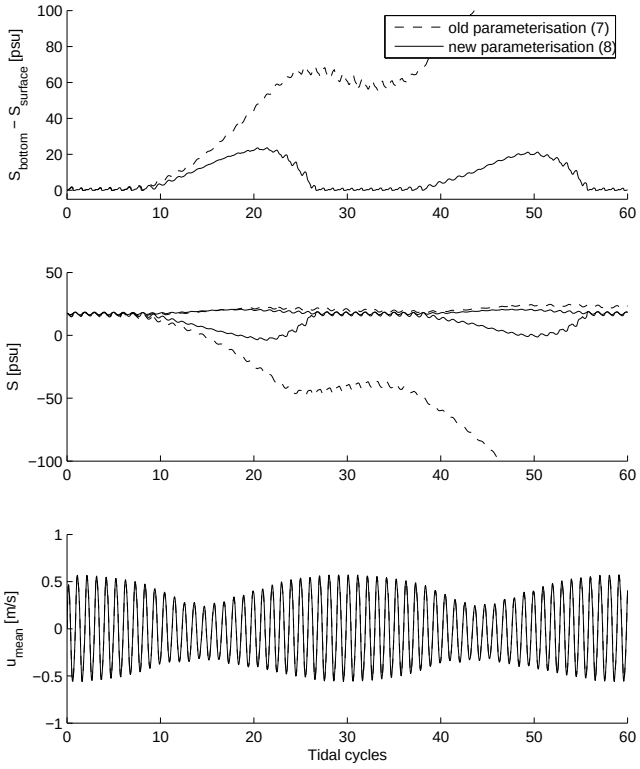

Figure 8: Sensitivity to the initial stratification: evolution of the stratification (difference between bottom salinity and surface salinity) for the different parameterisations of the horizontal salinity gradient, in the case of a SIPS regime (a) and persistent stratification (b). Two simulation results are showed for both regimes, with initial differences between bottom salinity and surface salinity set to 40 psu and 80 psu.

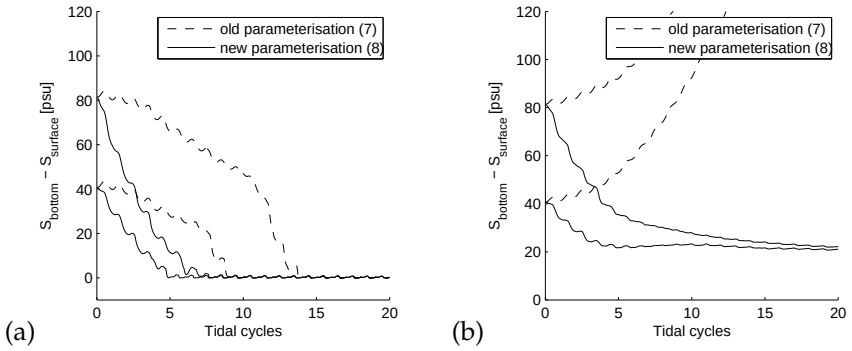

In the last experiment, we simulate a spring-neap cycles regime giving rise to runaway stratification. To this aim, the tidal amplitude is decreased to $U_{0,max} = 0.7\ m/s$ and $U_{1,max} = 0.46 \cdot U_{0,max}$, while the longitudinal constant salinity gradient is increased to $\tau = 0.3\ psu/km$. Figure 7 shows that the classical parameterisation of the horizontal salinity gradient term leads to a stratification which increases unboundedly and then cannot come back to the SIPS regime. During successive tidal cycles, the stratification strengthen to excessively large values. The new parameterisation, by limiting the peak of stratification to acceptable values, permits to come back to the SIPS regime during spring tides which is believed to be consistent with observation (Simpson *et al.*, 1990; Sharples and Simpson, 1993).

6 Discussion

We now investigate the impact of the initial conditions, in particular the stratification prescribed at the initial instant. Figure 8a shows the evolution of the stratification using different initial stratifications for the SIPS regime. For each parameterisation, the mixing is able to annihilate the stratification, yielding a SIPS regime. However, the decrease of the stratification is much faster using the new parameterisation. It was demonstrated in section 4 that, even if we have an overshooting or an undershooting in the initial salinity, this excess will be eliminated by the new parameterisation of the horizontal salinity gradient. If the stratification exceeds the upper limit, it cannot strengthen anymore when the new parameterisation is used, whereas the classical pa-

rameterisation still generates cycles of increase/decrease of stratification. In a persistent stratification regime (Fig. 8b), using the new parameterisation, the stratification decreases under its upper limit value, and then reaches a regime solution. The solution converges for any initial stratification. This confirms that any overshooting is directly eliminated by that parameterisation. The classical parameterisation, on the other hand, generates a runaway stratification.

By slightly modifying the equations, the present model could also be applied to the simulation of the tidal straining in a Region of Freshwater Influence (ROFI), for which the stratification induced by a gradient of density is also a key process (Visser *et al.*, 1994). The new parameterisation of the salinity gradient should be able to avoid the generation of runaway stratification in a ROFI model, for which this numerical complication can also occur.

7 Conclusions

Using simple mathematical developments, a new expression of the horizontal density gradient was developed in order to avoid the phenomenon known as "runaway stratification". This method allows for the simulation of rather realistic flows such as spring/neap cycles without any unrealistic stratification peak. It is guaranteed that no over- or under-shooting will be generated and that any initial over- or under-shooting will progressively disappear. The mathematical method we had recourse to for establishing the properties of the new parameterisation of horizontal salinity gradient may be applied to a wide range of partial differential problems in order to derive a priori upper or lower bounds of their solution. This technique is inspired by Lewandowski (1997). To the best of our knowledge, it has been used in a small number of oceanographic studies only (Deleersnijder *et al.*, 2001; Legrand *et al.*, 2006; Gourgue *et al.*, 2007).

Acknowledgements

Sébastien Blaise is a Research fellow with the Belgian Fund for Research in Industry and Agriculture (FRIA). Eric Deleersnijder is a Research associate with the Belgian National Fund for Scientific Research (FNRS). The present study was carried out within the scope of the project "A second-generation model of the ocean system", which is funded by the *Communauté Francaise de Belgique*, as *Actions de Recherche Concertées*, under contract ARC 04/09-316 and the project "Tracing and Integrated Modelling of Natural and Anthropogenic Effects on Hydrosystems" (TIMOTHY), an *Interuniversity Attraction Pole* (IAP6.13) funded by the *Belgian Federal Science Policy Office* (BELSPO). This work is a contribution to the development of SLIM, the Second-generation Louvain-la-Neuve Ice-ocean Model (http://www.climate.be/SLIM).

References

Blaise, S., Deleersnijder, E., White, L., and Remacle, J.-F. 2007. Influence of the turbulence closure scheme on the finite-element simulation of the upwelling in the wake of a shallow-water island. *Continental Shelf Research*, 27:2329–2345.

Burchard, H. 1999. Recalculation of surface slopes as forcing for numerical water column models and tidal flow. *Applied Mathematical Modelling*, 23:737–755.

Burchard, H. and Baumert, H. 1998. The formation of estuarine turbidity maxima due to density effects in the salt wedge. A hydrodynamic process study. *Journal of Physical Oceanography*, 28:309–321.

Deleersnijder, E. and Luyten, P. 1994. On the practical advantages of the quasi-equilibrium version of the Mellor and Yamada level 2.5 turbulence closure applied to marine modelling. *Applied Mathematical Modelling*, 18:281–287.

Deleersnijder, E., Campin, J.-M., and Delhez, E. J. M. 2001. The concept of age in marine modelling I. Theory and preliminary model results. *Journal of Marine Systems*, 28:229–267.

Galperin, B., Kantha, L., Hassid, S., and Rosati, A. 1988. A quasi-equilibrium turbulent energy model for geophysical flows. *Journal of the Atmospheric Sciences*, 45:55–62.

Gourgue, O., Deleersnijder, E., and White, L. 2007. Toward a generic method for studying water renewal, with application to the epilimnion of Lake Tanganyika. *Estuarine, Coastal and Shelf Science*, 74:764–776.

Hanert, E., Deleersnijder, E., and Legat, V. 2006. An adaptative finite element water column model using the Mellor-Yamada level 2.5 turbulence closure scheme. *Ocean Modelling*, 12:205–223.

Hanert, E., Deleersnijder, E., Blaise, S., and Remacle, J.-F. 2007. Capturing the bottom boundary layer in finite element ocean models. *Ocean Modelling*, 17:153–162.

Hetland, R. D. and Geyer, W. R. 2004. An idealized study of the structure of long, partially mixed estuaries. *Journal of Physical Oceanography*, 34:2677–2691.

Jay, D. A. and Musiak, J. D. 1994. Particle trapping in estuarine tidal flows. *Journal of Geophysical Research*, 99:445–461.

Legrand, S., Deleersnijder, E., Hanert, E., Legat, V., and Wolanski, E. 2006. High-resolution, unstructured meshes for hydrodynamic models of the Great Barrier Reef, Australia. *Estuarine, Coastal and Shelf Science*, 68:36–46.

Lewandowski, R. 1997. *Analyse Mathématique et Océanographie*. Masson, Paris. 281 p.

Linden, P. F. and Simpson, J. E. 1986. Gravity-driven flows in a turbulent fluid. *Journal of Fluid Mechanics*, 172:481–497.

Linden, P. F. and Simpson, J. E. 1988. Modulated mixing and frontogenesis in shallow seas and estuaries. *Continental Shelf Research*, 8(10):1107–1127.

Lucas, L. V., Cloern, J. E., Koseff, J. R., Monismith, S. G., and Thompson, J. K. 1998. Does the Sverdrup critical depth model explain bloom dynamics in estuaries? *Journal of Marine Research*, 56:375–415.

Lucas, L. V., Koseff, J. R., Cloern, J. E., Monismith, S. G., and Thompson, J. K. 1999. Processes governing phytoplankton blooms in estuaries. I: The local production-loss balance. *Marine Ecology Progress Series*, 187:1–15.

Mellor, G. L. and Yamada, T. 1974. A hierarchy of turbulence closure models for planetary boundary layers. *Journal of the Atmospheric Sciences*, 31:1791–1806.

Mellor, G. L. and Yamada, T. 1982. Development of a turbulence closure model for geophysical fluid problems. *Review of Geophysics and Space Physics*, 20:851–875.

Monismith, S. G. and Fong, D. A. 1996. A simple model of mixing in stratified tidal flows. *Journal of Geophysical Research*, 101(C12):28,583–29,595.

Monismith, S. G., Burau, J. R., and Stacey, M. T. 1996. *San Francisco Bay: The Ecosystem*, chapter Stratification dynamics and gravitational circulation in Northern San Francisco Bay, pages 123–153. American Association for the Advancement of Science, San Francisco.

Nunes Vaz, R. A. and Simpson, J. H. 1994. Turbulence closure modeling of estuarine stratification. *Journal of Geophysical Research*, 99(C8):16,143–16,160.

Scott, C. F. 2004. A prescriptive bulk model of periodic estuarine stratification driven by density currents and tidal straining. *Environmental Modeling and Assessment*, 9:13–22.

Sharples, J. and Simpson, J. H. 1993. Periodic frontogenesis in a region of freshwater influence. *Estuaries*, 16(1):74–82.

Simpson, J. H., Brown, J., Matthews, J., and Allen, G. 1990. Tidal Straining, Density Currents, and Stirring in the Control of Estuarine Stratification. *Estuaries*, 13(2):125–132.

Simpson, J. H., Sharples, J., and Rippeth, T. P. 1991. A prescriptive Model of Stratification Induced by Freshwater Runoff. *Estuarine, Coastal and Shelf Science*, 33:23–35.

Stacey, M. T. and Monismith, S. G. 1999. Observations of turbulence in a partially stratified estuary. *Journal of Physical Oceanography*, 29:1950–1970.

Visser, A. W., Souza, A. J., Hessner, K., and Simpson, J. H. 1994. The effect of stratification on tidal current profiles in a region of freshwater influence. *Oceanologica Acta*, 17(4):369–381.

Warner, J. C., Geyer, W. R., and Lerczak, J. A. 2005. Numerical modeling of an estuary: a comprehensive skill assessment. *Journal of Geophysical Research*, 110:C05001. Doi:10.1029/2004JC002691.

Figure 3.1: Equivalent two-dimensional $x - z$ model with three grid points and Dirichlet boundary conditions.

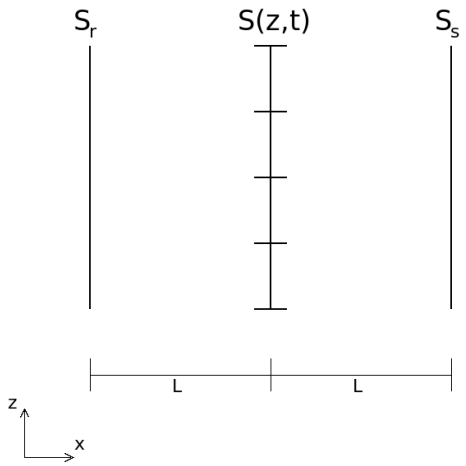

3.1 Comments on the publication

The configuration of the model described in the previous publication can be compared to a two-dimensional $x - z$ model with three grid points along the horizontal direction (Figure 3.1). The main difference is that upstream salinity S_r and downstream salinity S_s are not part of the discretization but consist of external data, not included in the discretization space. It is then comparable to the two-dimensional $x - z$ model with three grid points along the horizontal direction, in which we enforce Dirichlet boundary conditions on the two external water columns (Figure 3.1).

The treatment of the density gradient is called "parameterisation", because it is not included in the discretization space and can only be deduced from upstream and downstream constant values. It is then needed to parameterise this density gradient to be able to compute the advection term. Two different parameterisations were compared: a constant parameterisation (7) and a new parameterisation (8) which prevents the runaway stratification to appear.

If we consider the problem as a two-dimensional $x - z$ model with three grid points along the horizontal direction and dirichlet boundary conditions, the constant parameterisation (7) can no longer be called a parameterisation, as the density gradient is now included in the discretization space. Instead of a parameterisation, the method is equivalent to a centered discretization. As for the new parameterisation, it consists of a first order upwind discretization. It is then obvious that this upwind discretization will add horizontal diffusion (Fletcher, 1988).

Chapter 4

Turbulence modelling in three-dimensional models

Despite a highly multiscale aspect, a marine model is never able to compute all the scales of a flow. Complex phenomena whose characteristic lengths cannot be handled by the mesh need to be parameterised using a turbulence model. Turbulence model also parameterise phenomena that cannot be described by the equations. Such models have been subject to an extensive research for more than twenty years, and their increasing complexity is motivated by the raise of computing power that allows to use them on real scale problems (Burchard, 2002a).

4.1 The Mellor-Yamada level 2.5 turbulence closure

Different popular turbulence models were implemented in the framework of the present thesis. They belong to the class of eddy viscosity models: the effect of turbulence is parameterised using a turbulent viscosity (diffusivity for tracers) which is added to the molecular one, the latter often being negligible. The complexity of these models vary with the method used to compute the turbulent viscosity and diffusivity. Each turbulence model has assets and drawbacks, and no one can be claimed superior to others. However, some turbulence models are better adapted for specific configurations. It was also shown that more complex turbulence models can improve significantly the computation of ocean properties (Goosse *et al.*, 1999; Li *et al.*, 2001). In this chapter, we focus on the Mellor and Yamada level 2.5 turbulence closure developed by Mellor and Yamada (1974, 1982). It is a two-equations model with an equation used to compute the turbulent velocity energy scale while the other equation is used to obtain the turbulence length scale. The vertical eddy

viscosity and diffusivity for tracers are given by

$$\nu_v = S_u q l \qquad \text{and} \qquad \kappa_v = S_b q l \tag{4.1}$$

where l is a length scale, named the turbulence macroscale, representing the size of the energy-containing eddies. q is a velocity scale, linked to the turbulent kinetic energy k by

$$k = \frac{q^2}{2}. \tag{4.2}$$

The two equations of the model read

$$\frac{\partial q^2}{\partial t} = 2\nu_v M^2 - 2\kappa_v N^2 - \frac{2q^3}{B_1 l} + \frac{\partial}{\partial z}\left(K_q \frac{\partial q^2}{\partial z}\right), \tag{4.3}$$

$$\frac{\partial (q^2 l)}{\partial t} = E_1 l \nu_v M^2 - E_1 l \kappa_v N^2 - \frac{W q^3}{B_1} + \frac{\partial}{\partial z}\left(K_q \frac{\partial q^2 l}{\partial z}\right), \tag{4.4}$$

where $B_1 = 16.6$ and $E_1 = 1.8$ are constants of the model, and K_q is the eddy diffusivity for turbulence variables that is given by

$$K_q = S_q q l. \tag{4.5}$$

Stability functions S_u, S_b and S_q are needed to compute the eddy viscosity and diffusivity coefficients. S_q is generally taken equal to 0.2. The S_u and S_b stability functions devised by Galperin *et al.* (1988) for the quasi-equilibrium version of the MY25 turbulence closure are used, leading to a more robust model for marine modelling (Deleersnijder and Luyten, 1994):

$$S_u = \frac{0.39 - 3.09 G_H}{1 - 40.8 G_H + 212 G_H^2}, \tag{4.6}$$

$$S_b = \frac{0.49}{1 - 34.7 G_H}, \tag{4.7}$$

with $G_H = -\frac{l^2}{q^2} N^2$. The following constraints are enforced

$$l^2 \leq \frac{0.28 q^2}{\max(0, N^2)} \qquad \text{and} \qquad -0.28 \leq G_H \leq 0.0233. \tag{4.8}$$

A wall proximity function is needed to represent the logarithmic bottom boundary layer. This function W is defined as

$$W = 1 + \frac{E_2 l^2}{(\kappa L)^2}, \tag{4.9}$$

with the constant $E_2 = 1.33$. The function L depends on the distance to the sea bed d_b and the distance to the sea surface d_s, and is given by

$$L = \frac{d_s d_b}{d_s + d_b}. \tag{4.10}$$

The following article (Blaise *et al.*, 2007) is devoted to the influence of the Mellor and Yamada level 2.5 model on the simulation of the flow in the wake of a shallow-water island. It is shown that some phenomena, like the hysteresis effect, are not taken into account by simple closure models, and that the results are then less realistic in the considered configuration. The stress is put on the interaction between vertical mixing and upwelling, which are key players in the carrying of sediments from the seabed to higher depths. By making these sediments available to higher trophic levels, they act upon the whole food chain and have then a critical influence on the ecosystem.

Influence of the Turbulence Closure Scheme on the Finite-Element Simulation of the Upwelling in the Wake of a Shallow-Water Island

Sébastien Blaise[1], Eric Deleersnijder[2,3], Laurent White[3,2] and Jean-François Remacle[1,3]

[1]Université catholique de Louvain,
Unité de Génie Civil et Environnemental,
Louvain-la-Neuve, Belgium

[2]Université catholique de Louvain,
Institut d'Astronomie et de Géophysique G. Lemaître
B-1348 Louvain-la-Neuve, Belgium

[3]Université catholique de Louvain,
Centre for Systems Engineering and Applied Mechanics (CESAME)
B-1348 Louvain-la-Neuve, Belgium

E-mail: sebastien.blaise@uclouvain.be

Originally published in Continental Shelf Research, 27, 2329-2345 (2007)

Abstract

A three-dimensional finite-element model is used to investigate the tidal flow around Rattray Island, Great Barrier Reef, Australia. Field measurements and visual observations show both stable eddies developing at rising and falling tide in the wake of the island. The water turbidity suggests intense upwelling able to carry bed sediments upwards. Based on previous numerical studies, it remains unclear at this point whether the most intense upwelling occurs near the centre of the eddies or off the island's tips, closer to the island. All these studies resorted to a very simple turbulence closure, with a zero-equation model whereby the coefficient of vertical viscosity is computed via an algebraic expression. In this work, we aim at studying the influence of the turbulence closure on model results, with emphasis on the prediction of vertical motions. The Mellor and Yamada level 2.5 closure scheme is used and an increase in the intensity of vertical transport is observed. This increase is partly explained by the fact that the Mellor and Yamada model takes into account the hysteresis effect in the time variation of turbulence variables. The influence of the advection of turbulence variables is estimated to be negligible. By a better representation of transient coastal phenomena, the Mellor and Yamada level 2.5 turbulence closure improves the model to a significant degree.

Keywords: Finite Element Method, Turbulence closure scheme, Upwelling, Lee eddies, Shelf dynamics, Tidal currents, Unstructured mesh, Australia, Great Barrier Reef, Rattray Island

1 Introduction

Over the last decade, increasing effort has been directed toward the development of marine models using unstructured meshes. A thorough review of these studies is presented by Pain *et al.* (2005). Admittedly, unstructured meshes have much to offer for marine modelling. They allow for an accurate representation of the topography (e.g., islands, narrow straits) and the bathymetry (Legrand *et al.*, 2007, 2006). The mesh can easily be refined in regions of interest or coarsened in those regions where the dynamics is less demanding. Finally, unstructured meshes set up in spherical geometry should be able to circumvent the singularity at the poles, rendering those techniques potentially very useful for global scale ocean modelling (Legrand *et al.*, 2000; Gorman *et al.*, 2006). These assets are quite compelling for marine modelling and should prompt further developments and research for improving current models. Several numerical methods can handle unstructured meshes; among them the finite volume method, the spectral element method and the finite element method. In this paper, we focus on the finite element (FE) method.

The first developments of FE marine models were based on the wave continuity equation (Lynch and Gray, 1979), whereby the primitive shallow-water equations are manipulated to form a wave equation to predict the free-surface elevation. This method does not suffer from spurious oscillations occurring when using equal-order interpolations with the primitive equations. The generalisation of this method led to the generalised wave continuity equation (GWCE), documented by Kinnmark (1986). The GWCE has been extensively used over the past 20 years with successful applications in coastal regions for tidal predictions (Walters and Werner, 1989; Lynch and Naimie, 1993; Lynch *et al.*, 1996; Fortunato *et al.*, 1997; Cushman-Roisin and Naimie, 2002). This method, however, is subject to advective instabilities (Kolar *et al.*, 1994) and suffers from the breaking down of mass conservation (Massey and Blain, 2006), making it less suitable for coupling with transport equations and long-term integrations.

These limitations urged the development of marine models based on the primitive equations. To that end, research toward finding a stable mixed FE formulation for the shallow-water equations has been thriving since the end of the nineties (Le Roux *et al.*, 1998; Le Roux, 2001; Hanert *et al.*, 2003; Le Roux, 2005). Early issues of the FE method, often cited as pretexts not to use it, are starting to lose resilience. Nowadays, developments and applications of FE marine models based on the primitive equations are becoming less of an exception (Nechaev *et al.*, 2003; Danilov *et al.*, 2004; Ford *et al.*, 2004a,b; Danilov *et al.*, 2005; Hanert *et al.*, 2005b; Labeur and Pietrzak, 2005; Pain *et al.*, 2005;

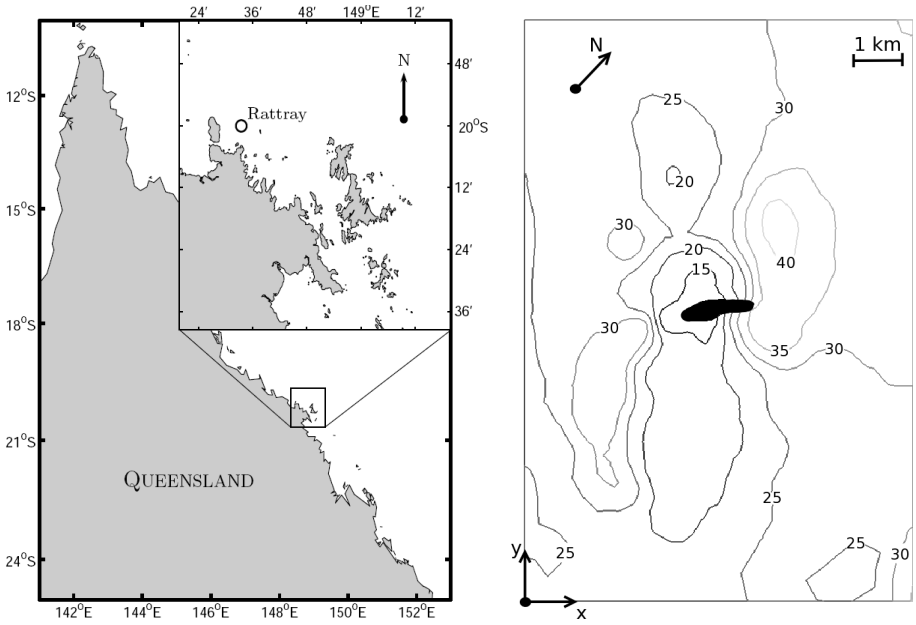

Figure 1: Left: location of Rattray Island in the Great Barrier Reef, Northeast Australia. Right: domain of interest with bathymetry in metres. Rattray Island is the black area in the centre. (from White *et al.*, 2007)

Pietrzak *et al.*, 2005, 2006; Walters, 2006; White and Deleersnijder, 2006; White *et al.*, 2007). This revolution in model design calls for validation test cases. Idealised test cases are generally too simple and are usually set up to validate the numerical component of a model without too much regard onto the ability of the model to represent the physics. There is a great need of realistic test cases against which models can assess their ability at representing processes encountered in the field. With this objective in mind, a self-forming group is putting together a set of realistic benchmarks that ought to remain relevant for the next decade (Aikman *et al.*, 2006). Following these guidelines, Blaise and White (2006) recently set up a benchmark focusing on the three-dimensional flow around Rattray Island, Great Barrier Reef, Northeast Australia (Figure 1).

In 1982, the Australian Institute of Marine Science carried out an extensive field survey at Rattray Island (Wolanski *et al.*, 1984). Twenty-six currentmeters were deployed at various sites in the southeast of the island and the water elevation was recorded. Landsat imagery and aerial photographs allow for direct visualisation of the secondary circulation in the wake of the island. The recirculating water is turbid, facilitating the interpretation of the circulation from the air. Since then, Rattray Island has been the focus of several stud-

ies (Falconer *et al.*, 1986; Black and Gray, 1987; Wolanski and Hamner, 1988; Deleersnijder *et al.*, 1992; Wolanski *et al.*, 1996; White and Deleersnijder, 2006; White *et al.*, 2007), all of them but the last using the finite difference method. By using a finite element model, White and Deleersnijder (2006) aimed at investigating the effect of an increase in mesh resolution, keeping all other parameterisations identical to that used in previous studies using the finite difference method (Deleersnijder *et al.*, 1992; Wolanski *et al.*, 1996). In this paper, the same FE model is utilised but it is improved with a more sophisticated turbulence closure.

Vertical mixing by turbulence is a key player in the dynamics of processes encountered in shallow coastal areas (Burchard, 2002). Simple turbulence closures, such as that used by Deleersnijder *et al.* (1992) and White and Deleersnijder (2006), neglect parts of the complex evolution of turbulent flows. In this paper, the Mellor and Yamada level 2.5 turbulence closure (MY25) (Mellor and Yamada, 1974, 1982) is considered mainly because it was designed and tuned for geophysical fluid flow problems. Moreover, this turbulence closure has been widely used in marine models (e.g. Blumberg and Galperin, 2006; Ruddick *et al.*, 1995; Ezer, 2005; Timmermann and Losch, 2005) and was recently implemented in a FE water column model (Hanert *et al.*, 2006). With a better parameterisation of turbulence, we seek to improve the prediction of the flow around Rattray Island and, in particular, the representation of the upwelling mechanisms. By carrying the sediments from the sea bed to the sea surface, an intense upwelling could be a dominant factor explaining the water turbidity in the wake of the island. Previous numerical models gave an insufficient upwelling velocity in the wake of the island. It was initially thought that the resolution of the models was insufficient (Deleersnijder *et al.*, 1992); but recent finite-element simulations with variable horizontal resolutions (White and Deleersnijder, 2006) showed that the resolution was not in question. In that study, the authors used a diagnosis of vertical transport based on the age of the bottom water, that can be considered to be the time elapsed since a constituent left the sea bottom (Delhez *et al.*, 1999; Deleersnijder *et al.*, 2001). Their results allow for concluding that upwelling also occurs off the island's tips (very close to the island) and not only near the centre of the eddies. Moreover, they found that upwelling off the island's tips was the most intense. However, the upwelling predicted by the model was not always sufficient to explain the presence of sediments at the sea surface. The turbulence closure used in their study was admittedly too simple. Therefore, it remains unclear whether the most significant upwelling mechanisms occur off the island's tips or near the centre of the eddies.

In this paper, after introducing the upwelling velocity we will describe the model and the parameters used to perform the simulations. Sections 4 to 7 will be devoted to the results of simulations and comparisons using different parameterisations of turbulence. The last section before the conclusion will estimate the importance of the advection of turbulence variables in the model applied to Rattray Island.

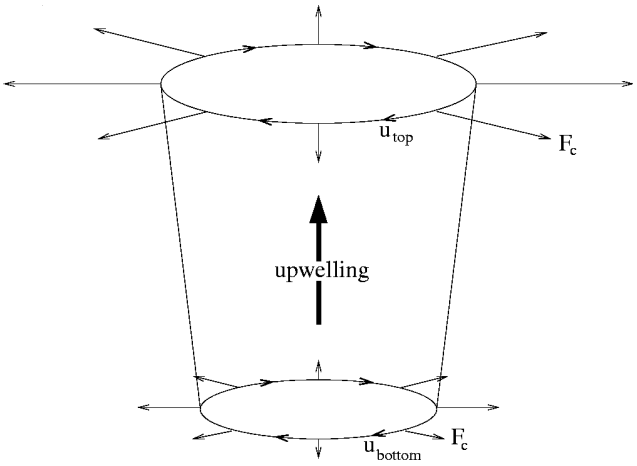

Figure 2: Schematic illustration of the mechanism of the upwelling induced in the centre of an eddy. F_c is the centrifugal acceleration due to the rotating velocity on the top (u_{top}) and on the bottom (u_{bottom}) perimeters of the eddy.

2 Upwelling velocity within eddies

The quantitative assessment of vertical motions calls for a representative estimator. In this work, the intensity of vertical transport will be estimated by using the so-called upwelling velocity (Deleersnijder, 1989, 1994). The upwelling velocity is not directly influenced by the bathymetry but is entirely due to upwelling mechanisms. Let us consider the following transformation to σ-coordinates:

$$\sigma = \frac{z - \eta}{h + \eta}, \tag{1}$$

where h and η are respectively the unperturbed sea depth and the sea surface elevation, positive upwards. The vertical coordinate z is pointing upward with its origin at the mean sea level. The upwelling velocity is the component of the vertical velocity that modifies the relative position of a particle within the water column, i.e. the vertical velocity component that allows a particle to cross iso-sigma surfaces. In this study, we will focus on the upwelling velocity, and the transport by turbulent mixing will not be included in the diagnoses. White and Deleersnijder (2006) showed that the upwelling velocity is presumably a dominant process in the rise of sediments.

Upwelling mechanisms in an eddy configuration are represented in Figure 2. The velocity of the fluid on the perimeter of the eddy is smaller near the sea bed (u_{bottom}) than near the sea surface (u_{top}) because of bottom friction. The rotating fluid is sustained by a centrifugal acceleration in equilibrium with the pressure gradient induced by the slope of the sea surface. Close to the

sea bed and because of bottom friction, the centrifugal acceleration magnitude decreases while the pressure gradient remains constant and this balance breaks down. This leads to flow convergence near the seabed and upwelling within the centre of the eddy. On the outer edge of the eddy, the centrifugal acceleration leads to a convergence of the flow at the sea surface, inducing downwelling. Thus, shallow-water eddies tend to induce upwelling at the centre and downwelling along the outer edge. The upwelling mechanism in eddies is similar to that occuring in a stirred tea cup, with a convergent flow near the bottom and upwelling in the centre (Bowker, 1988; Wolanski *et al.*, 1996). In this work, we will focus on upwelling zones. According to the foregoing explanations, the larger the difference between the bottom velocity and the surface velocity, the larger the upwelling in the centre of the eddy.

3 Model description

We use the three-dimensional finite-element marine model developed within the scope of the SLIM project (Second-generation Louvain-la-Neuve Ice-ocean Model, http://www.climate.be/SLIM). A version of the model SLIM, using sigma coordinates and considering a constant density, is described in detail by White *et al.* (2007) and the configuration used for studying the flow around Rattray Island is presented by White and Deleersnijder (2006). It is very briefly recalled here. According to Wolanski *et al.* (1984), temperature and salinity contrasts are negligible near Rattray Island. Therefore, we consider the water to have a constant density. We work on an f-plane and under the hydrostatic approximation. Wind stress is not considered. The same assumptions as those of White and Deleersnijder (2006) are made here so that the only difference between both models is the turbulence closure.

The horizontal momentum equation is then

$$\frac{\partial \mathbf{u}}{\partial t} + (\mathbf{v} \cdot \nabla)\,\mathbf{u} + f\widehat{\mathbf{e}}_{\mathbf{z}} \wedge \mathbf{u} = -g\nabla_h \eta + \frac{\partial}{\partial z}\left(\nu_v \frac{\partial \mathbf{u}}{\partial z}\right) + \mathbf{D}, \tag{2}$$

where $\mathbf{v} = (u, v, w)$ is the velocity and $\mathbf{u} = (u, v)$ contains the horizontal components of $\mathbf{v}$. The three-dimensional gradient operator is designated by ∇; ∇_h is used to designate the horizontal gradient operator, which applies on the horizontal components of a vector. The constant Coriolis parameter and the gravitational acceleration are respectively represented by f and g; ν_v and $\widehat{\mathbf{e}}_{\mathbf{z}}$ are respectively the vertical eddy viscosity coefficient and the upward-pointing unit vector. In the scope of this work, the vertical eddy viscosity will be calculated by means of different turbulence closure schemes in order to investigate their effect on the results. $\mathbf{D}$ is the parameterisation of horizontal momentum diffusion. In addition to equation (2), the continuity equation is used to diagnostically compute the vertical velocity:

$$\frac{\partial u}{\partial x} + \frac{\partial v}{\partial y} + \frac{\partial w}{\partial z} = 0. \tag{3}$$

The free-surface elevation equation is derived from

$$\frac{\partial \eta}{\partial t} + \nabla_h \cdot \left(\int_{-h}^{\eta} \mathbf{u} \mathrm{d}z \right) = 0. \tag{4}$$

The total height of the water column is defined as $H(x, y, t) = h(x, y) + \eta(x, y, t)$. The horizontal momentum diffusion term $\mathbf{D}$ is

$$\mathbf{D} = \frac{\partial}{\partial x} \left(\nu_h \frac{\partial \mathbf{u}}{\partial x} \right) + \frac{\partial}{\partial y} \left(\nu_h \frac{\partial \mathbf{u}}{\partial y} \right), \tag{5}$$

in which ν_h is computed using a Smagorinsky scheme (Smagorinsky, 1963)

$$\nu_h = c_s \triangle^2 \left[\frac{\partial \overline{u}}{\partial x} \frac{\partial \overline{u}}{\partial x} + 0.5 \left(\frac{\partial \overline{u}}{\partial y} + \frac{\partial \overline{v}}{\partial x} \right)^2 + \frac{\partial \overline{v}}{\partial y} \frac{\partial \overline{v}}{\partial y} \right]^{\frac{1}{2}}, \tag{6}$$

where c_s is a constant and Δ^2 is a the surface area of the local triangle (Akin *et al.*, 2003). The overbar stands for depth-averaged quantities.

In this paper, the domain geometry, boundary conditions and forcings are identical for all simulations.. The tidal ellipses are strongly polarised (Wolanski *et al.*, 1984) and a good approximation consists in assuming the mean flow to be unidirectional. The domain is rotated so that its y-axis is parallel to the direction of the tidal flow. Lateral boundaries are then assumed to be impermeable, without lateral friction. The southeast and northwest boundaries remain open. On the open boundaries, the depth-averaged velocity and the elevation obtained from field measurements are imposed under the form of the incoming characteristic variable $\overline{u}_n - \eta\sqrt{g/h}$ where $\overline{u}_n$ is the depth-averaged normal velocity (Flather, 1976; Ruddick *et al.*, 1994). The phase lag between incoming and outgoing boundaries is neglected. The size of the domain is $8,2km$ in the x-direction and $12,1km$ in the y-direction.

Two different unstructured meshes, refined in the vicinity of the island, are employed. The coarse mesh is made of 3024 triangles and 10 layers on the vertical (Figure 3). Its horizontal resolution varies from $140m$ in the vicinity of the island to $700m$ near the domain boundaries. The fine mesh comprises 6096 triangles and 16 layers on the vertical. Its horizontal resolution in the vicinity of the island is $85m$ whereas the resolution near the domain boundaries is unchanged. The Smagorinsky constant c_s is set to 0.1 for the coarse mesh and 0.3 for the fine mesh, giving approximately the same peak eddy viscosity values in the island's wake ($\nu_h = 0.5$ m^{2}s^{-1}) for both meshes, in agreement with estimates by Wolanski *et al.* (1984). The time step is 15 seconds. All results are presented after three days of physical time in order to reach a regime situation.

4 Simple turbulence closure

In this section, the simple algebraic turbulence closure suggested by Fisher *et al.* (1979) and used by Deleersnijder *et al.* (1992) and White and Deleersnijder (2006) is presented. Accordingly, the vertical eddy viscosity ν_v is

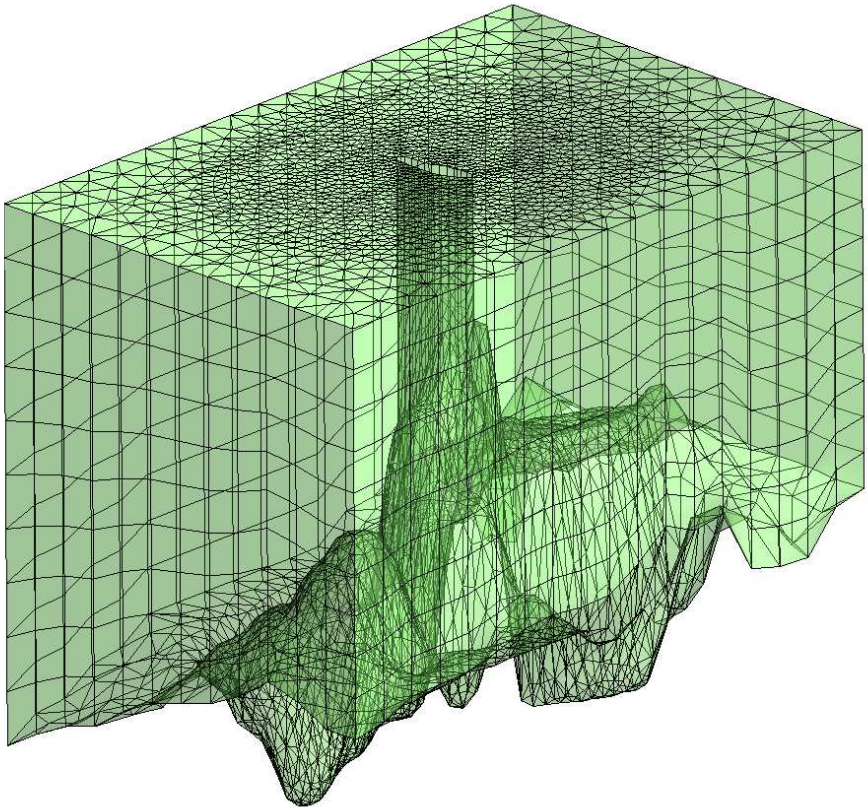

Figure 3: Coarsest unstructured mesh used for the simulations. The mesh contains 3024 triangles and 10 layers on the vertical. To better render the bathymetry, a stretch is applied in the vertical direction.

$$\nu_v = \kappa u_* \left(h + z + z_0\right) \left(1 - \delta \frac{h + z + z_0}{H}\right), \tag{7}$$

where $\kappa \simeq 0.4$ is the von Karman constant, δ is an adjustable parameter, z_0 is the bottom roughness height and u_* is the bottom friction velocity computed as

$$u_*^2 = \frac{|\boldsymbol{\tau}|}{\rho_0} \tag{8}$$

in which ρ_0 is the water density and $\boldsymbol{\tau}$ is the bottom stress parameterised by

$$\frac{\boldsymbol{\tau}}{\rho_0} = \left(\frac{\kappa}{\ln\left(\frac{h+z+z_0}{z_0}\right)}\right)^2 |\mathbf{u}(\mathbf{z})|\, \mathbf{u}(\mathbf{z}), \tag{9}$$

where z is taken at mid-height of the first layer near the bottom. First, the δ parameter is taken to be the usual value of 0.6. This value was used in several works, including studies focusing on Rattray Island (Deleersnijder *et al.*, 1992; White and Deleersnijder, 2006). However, using this value implies a nonzero vertical eddy viscosity at the sea surface. With the MY25 closure, the boundary condition is $\nu_v = 0$ at the sea surface when the wind stress is neglected. Obtaining a qualitatively comparable eddy viscosity profile with the simple turbulence closure requires the choice of $\delta = 1$. Results for both values of δ are presented.

Results considered in this section are taken at four different simulation times. Snapshots at these times (labelled 1 to 4) correspond respectively to December 1, 1982 at 1h40 (falling tide, peak ebb velocity), 5h00 (end of falling tide, shortly before tide reversal), 7h55 (rising tide, peak flood velocity) and 10h50 (end of rising tide, shortly before tide reversal). Figure 4 shows the depth-averaged velocity at these different times, using the model with the simple turbulence closure and $\delta = 0.6$. Trial calculations showed that the choice of turbulence closure (simple or MY25) did not significantly influence the depth-averaged horizontal velocity field. Therefore, Figure 4 gives an overview of the flow around the island that is applicable to all subsequent discussions. Figure 4 clearly shows two counter-rotating eddies of different sizes in the wake of the island. The difference between these eddies is mostly due to bathymetric effects. A study by Falconer *et al.* (1986) shows that when the model is run on a flat bottom, both eddies are almost symmetric in size and intensity. Our model reproduces these predictions (not shown).

Results for the upwelling velocity using the simple turbulence closure and $\delta = 0.6$ are depicted in Figure 5. Simulations on the coarse mesh give results that are slightly noisier, but not qualitatively different. Therefore, further simulations with the simple turbulence closure will only be carried out on the fine mesh. Since the model is the same as that used by White and Deleersnijder (2006), we have similar results. Using a value of $\delta = 1$ (Figure 6) has the

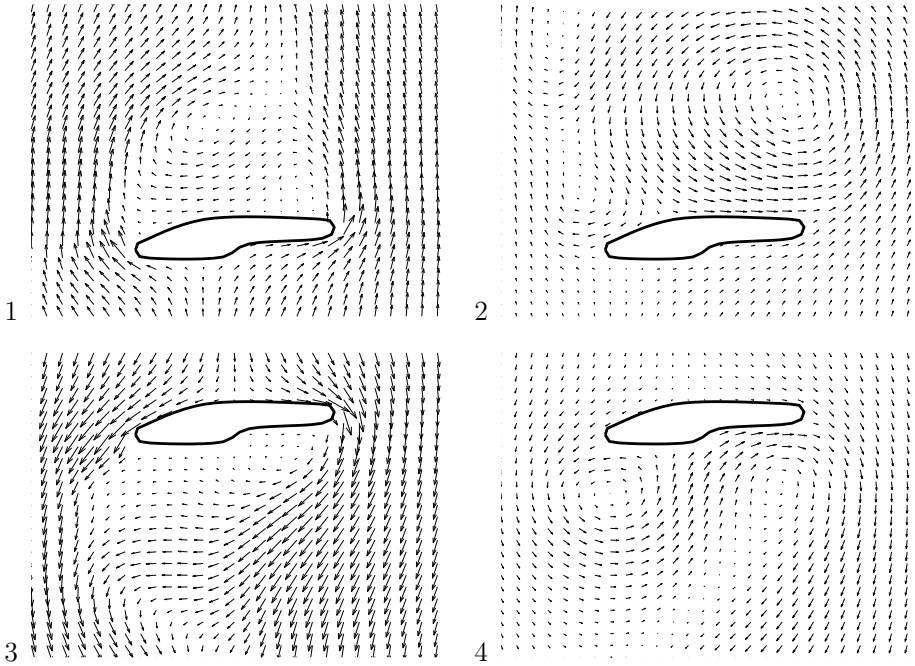

Figure 4: Depth-averaged velocity field on the fine mesh, using the model with simple turbulence closure with the parameter $\delta = 0.6$. Snapshots (1,2,3 and 4) respectively taken on December 1, 1982 at 1h40 (falling tide, peak ebb velocity), 5h00 (end of falling tide, shortly before tide reversal), 7h55 (rising tide, peak flood velocity) and 10h50 (end of rising tide, shortly before tide reversal). The velocity has been interpolated on a structured mesh. The mean velocity in the y-direction at snapshots (1,2,3 and 4) is respectively $0.49m/s$, $0.16m/s$, $-0.52m/s$ and $-0.16m/s$.

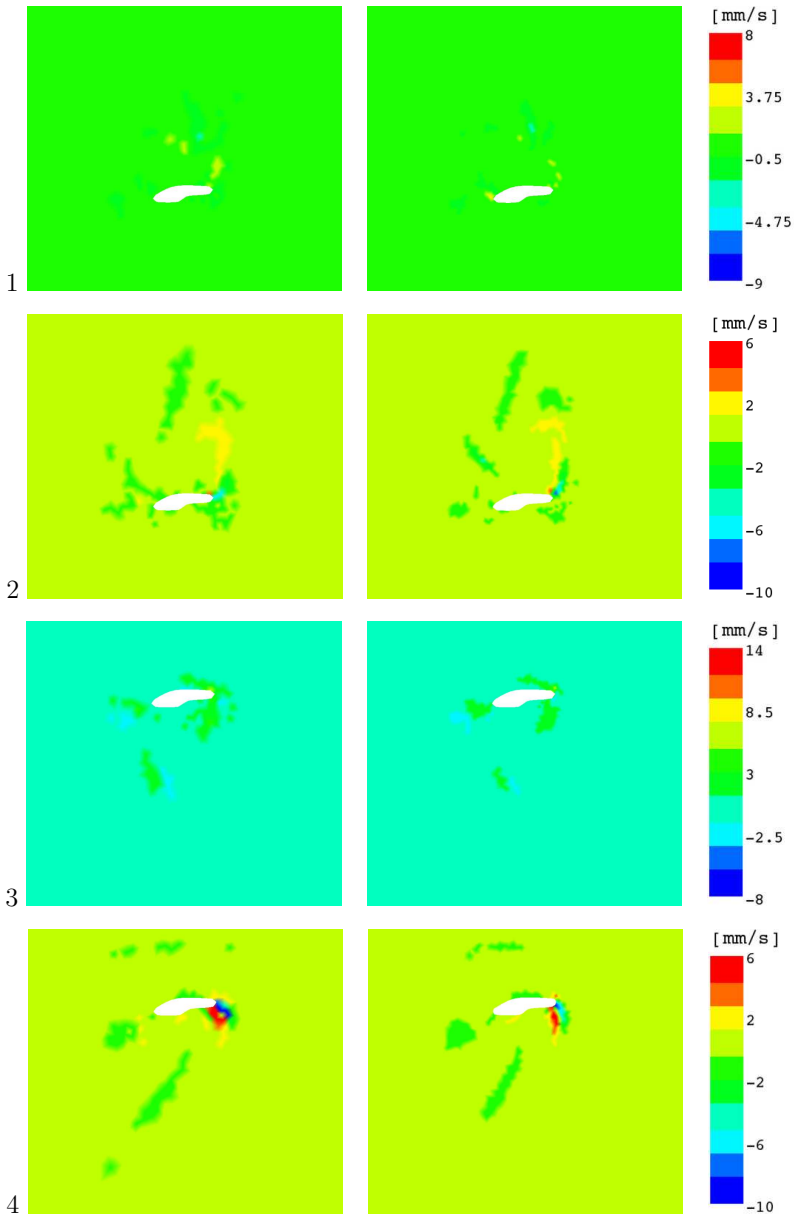

Figure 5: Upwelling velocity at mid-depth for the coarse mesh (left column) and for the fine mesh (right column), using the simple turbulence closure with the parameter $\delta = 0.6$. Snapshots (1,2,3 and 4) respectively taken on December 1, 1982 at 1h40 (falling tide, peak ebb velocity), 5h00 (end of falling tide, shortly before tide reversal), 7h55 (rising tide, peak flood velocity) and 10h50 (end of rising tide, shortly before tide reversal).

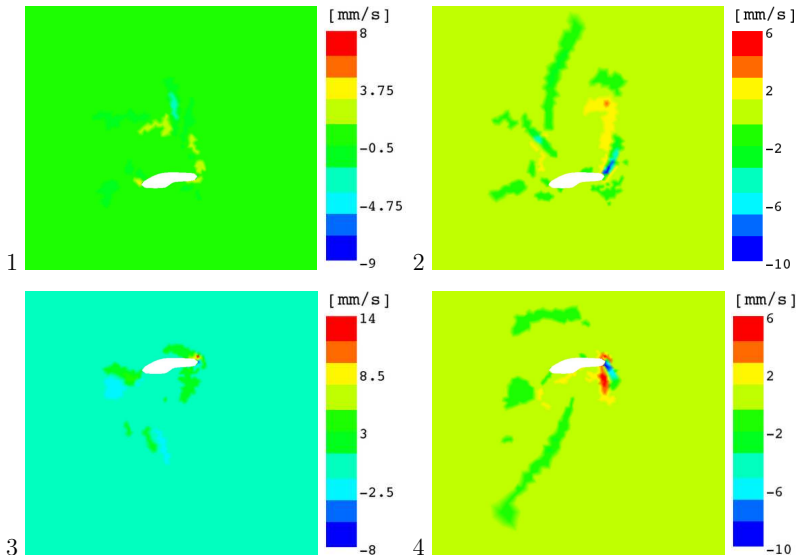

Figure 6: Upwelling velocity at mid-depth for the fine mesh, using the simple turbulence closure with the parameter $\delta = 1$. Snapshots (1,2,3 and 4) respectively taken on December 1, 1982 at 1h40 (falling tide, peak ebb velocity), 5h00 (end of falling tide, shortly before tide reversal), 7h55 (rising tide, peak flood velocity) and 10h50 (end of rising tide, shortly before tide reversal).

effect of increasing the area on which upwelling is significant. The explanation is as follows. As we can see in equation (7), a larger value of δ leads to a lower value of ν_v, implying less vertical mixing. This decrease in vertical mixing gives rise to a larger vertical shear in the horizontal velocity near the bottom, inducing more intense upwelling.

5 A sophisticated turbulence closure

We have implemented the Mellor and Yamada level 2.5 (MY25) turbulence closure that was developed by Mellor and Yamada (1974, 1982). This turbulence closure includes an equation for the evolution of the variable q^2 (where $q^2/2$ is the turbulent kinetic energy), and an equation for the evolution of the variable $q^2 l$ (where l is the turbulent length scale). To have a more robust model for marine modelling, the quasi-equilibrium version of the MY25 turbulence closure was used (Galperin *et al.*, 1988; Deleersnijder and Luyten, 1994). Since we consider a fluid of constant density, stratification is not considered in the model. The following boundary condition on q^2 is enforced both at the sea

surface and at the bottom (Stacey and Pond, 1997):

$$q^2 = B_1^{2/3} u_*^2. \tag{10}$$

Note that we neglect the surface stress, which implies that we have $q^2 = 0$ at the surface. The boundary condition on the turbulent length scale, used at the bottom, is

$$l = \kappa z_0. \tag{11}$$

As in Deleersnijder *et al.* (1992) and White and Deleersnijder (2006), the value of the bottom roughness height z_0 is fixed to $5 \cdot 10^{-3} m$, that is typical of rough sea beds (Black and Gray, 1987). Simulations showed that variations of the bottom roughness height do not change significantly the results. At the sea surface, the boundary condition on the turbulent length scale is:

$$l = 0. \tag{12}$$

In this section, horizontal diffusion and advection of turbulence variables are not considered since they are generally deemed negligible in marine modelling compared to the more important production and destruction terms. We will investigate below how including advection affects the turbulence closure behaviour. Simulation results with the MY25 turbulence closure are shown in Figure 7. Similarly to the simple closure, simulation results are less noisy with the finest mesh. However, results using the two meshes are not qualitatively different. Now, these results will be compared with the model using the simple closure and $\delta = 1$ (Figure 6). This comparison emphasises an increase in the upwelling velocity with the MY25 model, especially for snapshots (1) and (3).

Though upwelling mechanisms are influenced by a lot of complex processes, general tendencies can nonetheless be brought to light. In order to analyse the effect of the turbulence closure scheme upon the upwelling velocity, let us consider a particular location in the two-dimensional plane where these mechanisms will be studied. This location, noted P in Figure 8, lies on the perimeter of the main eddies in the wake of the island at falling tide. Figure 9 shows the temporal evolution of the vertical eddy viscosity coefficient at P and at a depth equivalent to 90% of the total depth. Two differences between both turbulence closures are clearly visible. First, the mean eddy viscosity coefficient is slightly greater with the simple closure model. Second, there is a time lag between the two models. With the simple closure, the eddy coefficients react instantaneously when the flow changes. However, in nonstationary flows, the turbulence variables are affected by a hysteresis phenomenon. The latter has a great influence on the modeled flow during the acceleration and deceleration phases of the tide (Baumert and Radach, 1992). This hysteresis phenomenon is taken into account by the MY25 closure but not by the simple closure. In Figure 9, the time line is decomposed into two types of intervals (A and B), corresponding respectively to intervals where the vertical

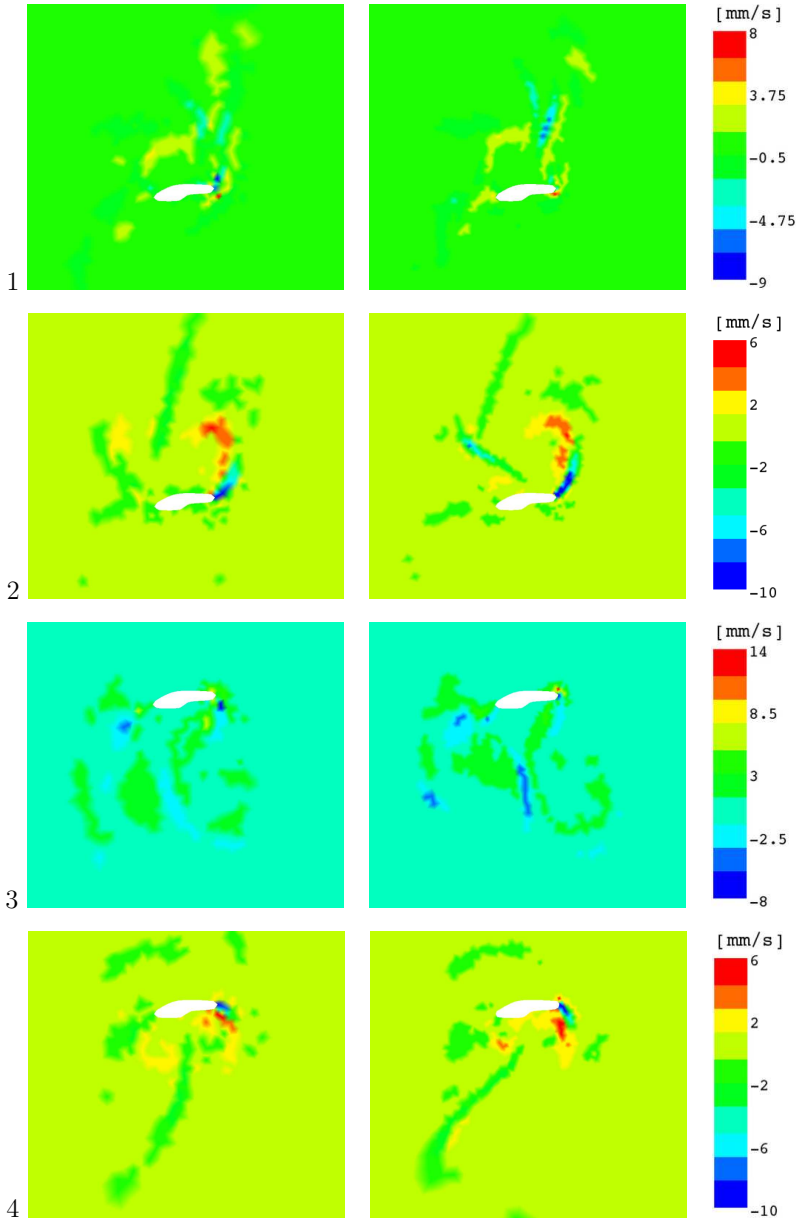

Figure 7: Upwelling velocity at mid-depth for the coarse mesh (left column) and for the fine mesh (right column), using the Mellor and Yamada level 2.5 turbulence closure. Snapshots (1,2,3 and 4) respectively taken on December 1, 1982 at 1h40 (falling tide, peak ebb velocity), 5h00 (end of falling tide, shortly before tide reversal), 7h55 (rising tide, peak flood velocity) and 10h50 (end of rising tide, shortly before tide reversal).

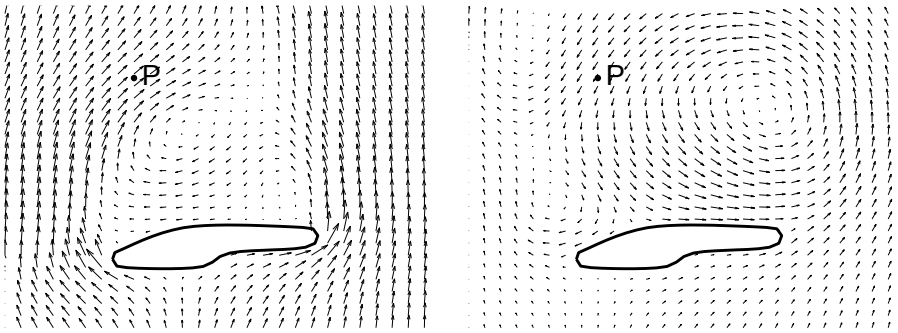

Figure 8: Position of the water column where temporal plots of velocity and eddy viscosity are studied. P is located on the perimeter of the eddy at falling tide. Snapshots (1,2) taken respectively on December 1, 1982 at 1h40 (falling tide, peak ebb velocity) and 5h00 (end of falling tide, shortly before tide reversal).

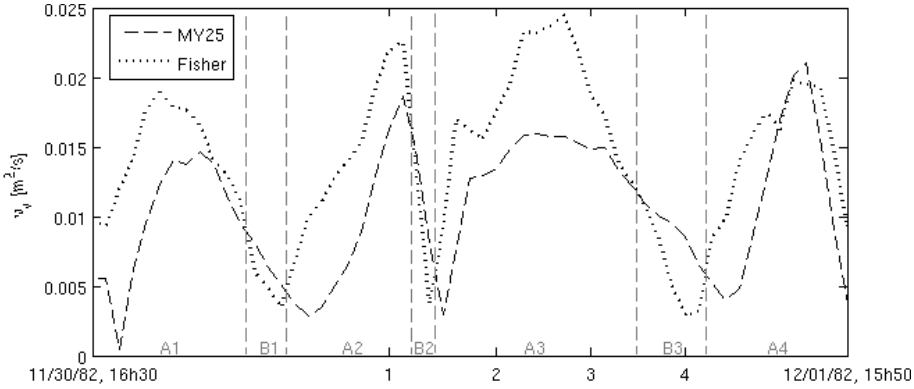

Figure 9: Temporal evolution of the eddy viscosity at a depth of 90% near the bottom and at P position. Comparison between the Mellor and Yamada level 2.5 turbulence closure and the simple turbulence closure (Fisher) with $\delta = 1$. Times (1,2,3 and 4) correspond respectively to December 1, 1982 at 1h40 (falling tide, peak ebb velocity), 5h00 (end of falling tide, shortly before tide reversal), 7h55 (rising tide, peak flood velocity) and 10h50 (end of rising tide, shortly before tide reversal).

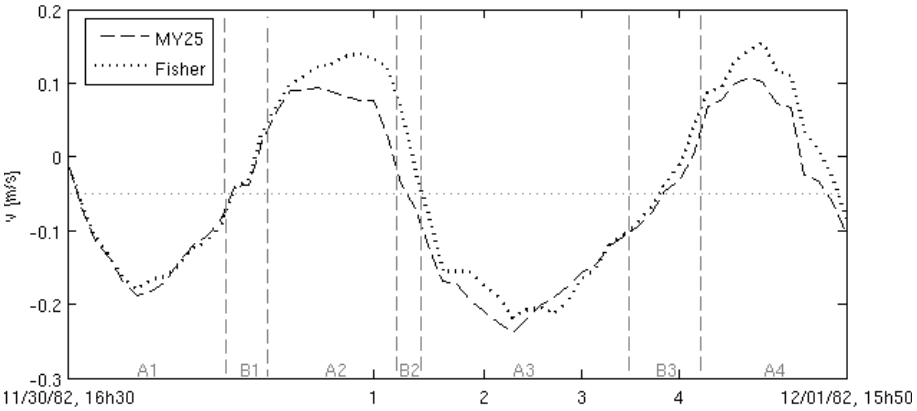

Figure 10: Temporal evolution of the bottom velocity at P position. Comparison between the Mellor and Yamada level 2.5 turbulence closure and the simple turbulence closure (Fisher) with $\delta = 1$. Times (1,2,3 and 4) correspond respectively to December 1, 1982 at 1h40 (falling tide, peak ebb velocity), 5h00 (end of falling tide, shortly before tide reversal), 7h55 (rising tide, peak flood velocity) and 10h50 (end of rising tide, shortly before tide reversal).

eddy viscosity coefficient with the MY25 model is smaller or larger than that computed by the simple closure. Figure 10 shows the bottom velocity in the y direction at P using both closures. The velocity in the y direction was chosen in lieu of the norm of the velocity in order to clearly distinguish between rising and falling tides. Moreover, the velocity in the y direction corresponds to the main component of the three-dimensional velocity during the simulation. The interesting time intervals for the study of upwelling in Figure 10 and 9 are situated in the proximity of times (1) and (2). At times (3) and (4), location P is situated upstream of the island where there is neither eddies nor upwelling.

The effects of the MY25 closure in the A intervals are explained in Figure 11. In these zones, we have less mixing with the MY25 model yielding a larger vertical shear in the horizontal velocity. Then, the accelerations near the bottom are smaller with the MY25 closure, whereas the decelerations are larger; i.e. the bottom velocity tends to be lower with the MY25 closure. This is visible in Figure 10, mainly in (A-2) and (A-4) intervals.

Over the B intervals (Figure 11), the opposite behaviour is expected (i.e. the bottom velocity tends to be greater with the MY25 closure). In Figure 10, it is difficult to observe such a tendency. There are three possible reasons for this. First, the bottom velocity is so small in these regions, that the bottom friction has a very limited effect. Second, there is a time lag between the variations of the vertical eddy viscosity and their effect on the velocity. Third, the difference in the vertical eddy viscosity between both closures remain quite limited

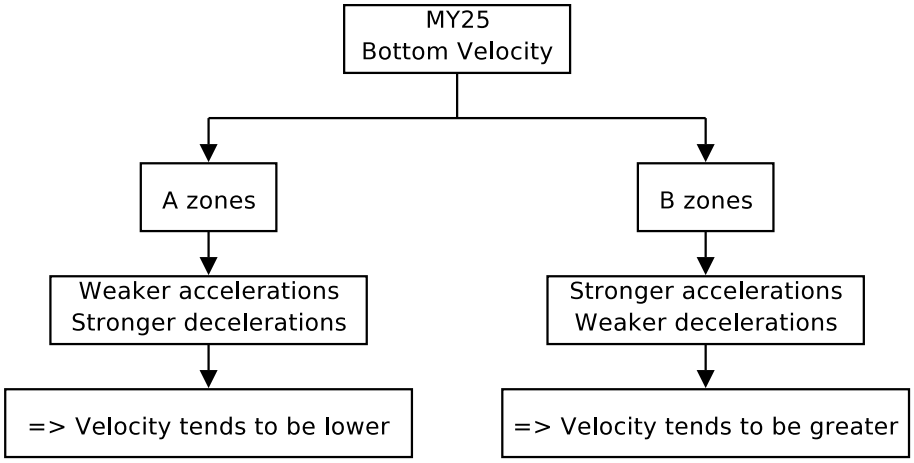

Figure 11: Effects on the bottom velocity due to the MY25 model.

in these intervals (except in (B-3) where we can better observe the expected tendency).

The influence of the turbulence closure on the bottom velocity causes differences in the upwelling velocity. As the A intervals are dominant in this case, the bottom velocity is generally lower with the MY25 model. This leads to a greater vertical gradient of velocity and a more intense upwelling with the MY25 model, which can be seen by comparing Figure 6 and Figure 7.

Vertical profiles of the vertical eddy viscosity are shown in Figure 12 at the four different times. The profiles are very similar for the two models. They have the same parabolic shape, but the maximum value of the eddy viscosity on the water column is different. The difference between both closures is mainly related to the time lag and the generally larger values of the eddy viscosity coefficient for the simple closure model. These two factors influence the difference between the profiles.

To isolate the hysteresis effect, one can fix the eddy viscosity coefficient, averaged over the whole spatial and temporal domains, at the same value for the two methods. Doing so, only the hysteresis phenomena will have an effect in the comparison between both closures. This correction was made by multiplying the eddy viscosity coefficient field obtained with the MY25 model by a constant value in order to make its mean value equal to the mean eddy viscosity obtained with the simple closure model with $\delta = 1$.

Results obtained with the MY25 modified closure are shown in Figure 13. We see that, for snapshots 1, 2 and 3, the upwelling velocity increases with the MY25 modified closure in comparison with the simple closure model. However, at snapshot (4) at the end of rising tide, values of upwelling velocity are smaller with the MY25 modified model. This can be explained in Figure 14

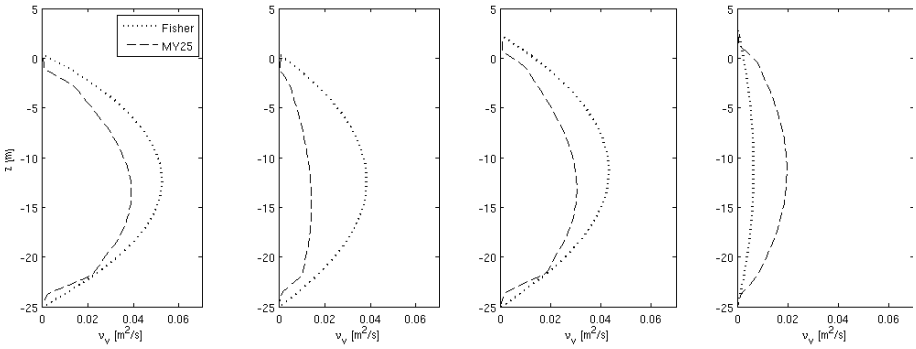

Figure 12: Vertical profile of vertical eddy viscosity at P position. Comparison between the Mellor and Yamada level 2.5 turbulence closure and the simple turbulence closure (Fisher) with $\delta = 1$. Snapshots (1,2,3 and 4) respectively taken on December 1, 1982 at 1h40 (falling tide, peak ebb velocity), 5h00 (end of falling tide, shortly before tide reversal), 7h55 (rising tide, peak flood velocity) and 10h50 (end of rising tide, shortly before tide reversal).

showing the temporal evolution of the vertical eddy viscosity coefficient at P and at a depth of 90% near the bottom. We can see that the only effect is the time lag. The MY25 modified closure responds with a delay compared with the simple closure. The consequence is that, at the beginning of the tides (A intervals), the MY25 modified closure gives less mixing than the simple closure model. The upwelling at these times tends to be more important for the MY25 modified closure. However, before tide reversal (B intervals), the MY25 modified closure gives more mixing than the simple closure model. This is particularly visible at snapshot (4). At this moment, the upwelling velocity is less important compared with the simple closure model.

The time lag effect can cause differences in the upwelling velocity, but since these differences can be positive or negative, they do not necessarily lead to a global increase or decrease in upwelling. This time lag may be substantial and can reach up to one hour.

6 Discussion

To see if the predicted upwelling would be sufficient to carry the sediments from the sea bed to the sea surface within an eddy, the upwelling velocity can be time-integrated during the course of a tidal cycle. This integration yields what we will define as an upwelling height, and takes into account both upwelling and downwelling that can occur during the integration period. This integration was carried out at a location (noted Q in Figure 15), situated in

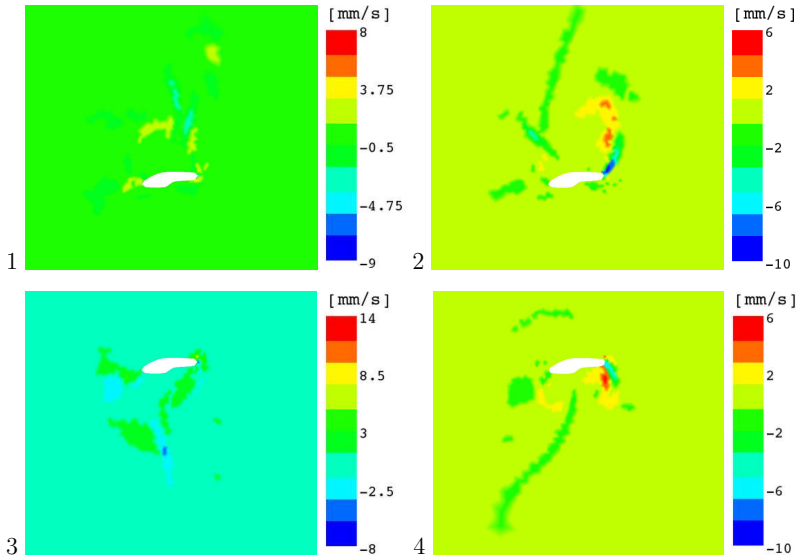

Figure 13: Upwelling velocity at mid-depth for the fine mesh, using the Mellor and Yamada level 2.5 turbulence closure with modified vertical eddy viscosity in order to have the same mean value than using the simple turbulence closure. Snapshots (1,2,3 and 4) respectively taken on December 1, 1982 at 1h40 (falling tide, peak ebb velocity), 5h00 (end of falling tide, shortly before tide reversal), 7h55 (rising tide, peak flood velocity) and 10h50 (end of rising tide, shortly before tide reversal).

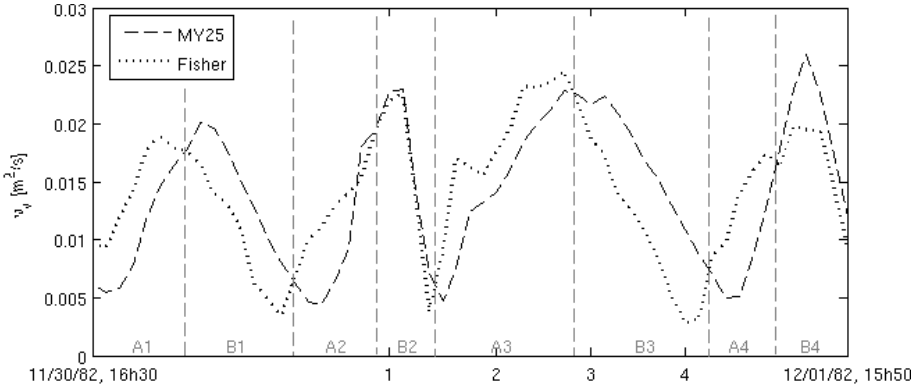

Figure 14: Temporal evolution of the eddy viscosity at a depth of 90% near the bottom and at P position. Comparison between the Mellor and Yamada level 2.5 turbulence closure with a multiplicative factor for ν_v and the simple turbulence closure (Fisher) with $\delta = 1$. Times (1,2,3 and 4) correspond respectively to December 1, 1982 at 1h40 (falling tide, peak ebb velocity), 5h00 (end of falling tide, shortly before tide reversal), 7h55 (rising tide, peak flood velocity) and 10h50 (end of rising tide, shortly before tide reversal).

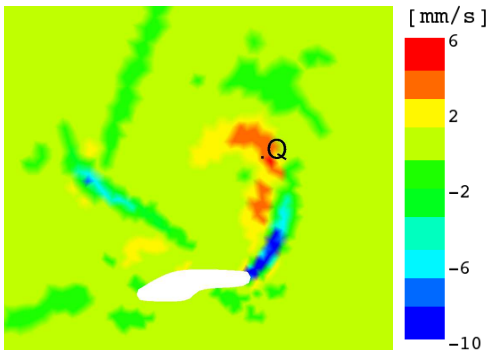

Figure 15: Position of the water column where the upwelling velocity is time-integrated over a tide period. Snapshot taken on December 1, 1982 at 5h00 (end of falling tide, shortly before tide reversal) with the Mellor and Yamada level 2.5 turbulence closure.

Turbulence model	Upwelling height $[m]$
Simple closure, $\delta = 0.6$	11.5
Simple closure, $\delta = 1$	19.6
MY25 modified	24.6
MY25	30.1

Table 1: Time-integration over a tide period of the upwelling velocity at mid-depth on Q position. Integration started on December 1, 1982 at 0h55 and ended at 7h05, the same day.

a high upwelling zone at falling tide. The results of the time integration of the upwelling velocities are shown on Table 1. As the depth at Q is about 25 m, we can reasonably assume that only the MY25 and the MY25 modified closures will be able to account for the vertical transport throughout the water column during the period considered. However, this diagnosis is based on restrictive hypotheses. First, we use the upwelling velocity at mid-depth where it typically reaches its maximum value. Second, the integration of the upwelling velocity does not take into account the horizontal transport. By resorting to the theory of the age (Delhez *et al.*, 1999; Deleersnijder *et al.*, 2001), the study by White and Deleersnijder (2006) showed that horizontal transport could be crucial in explaining upwelling mechanisms. Nevertheless, the time integration of the upwelling velocity can give a good idea of the capacity of the vertical flow to carry the sediments to the sea surface within eddies.

It is often assumed that the characteristic time is much larger for the advection of turbulence variables than for the production/destruction terms. If so, the advection term can be regarded as negligible. At smaller scales, this term could be more important, particularly for complex bathymetries. There we study the influence of the advection term of turbulence variables upon the upwelling velocity. Figure 16 shows the upwelling velocity at four different times, obtained from the simulation using the MY25 closure with advection of turbulence variables. The simulations are performed with the coarse mesh. In comparison with Figure 7, we can see that advection of turbulence variables has a small influence on the results. This can be understood with an order of magnitude analysis of the different terms influencing the evolution of the turbulent kinetic energy. The simulation results show that the advection has an influence that is on average 10 times less important than the production/destruction terms. Vertical diffusion is almost of the same order of magnitude as the production/destruction term. In the context of Rattray Island and similar problems, the advection of turbulence variables has a limited effect and can be neglected. It might, however, be important in other configurations, especially for flow characterised by smaller horizontal scales.

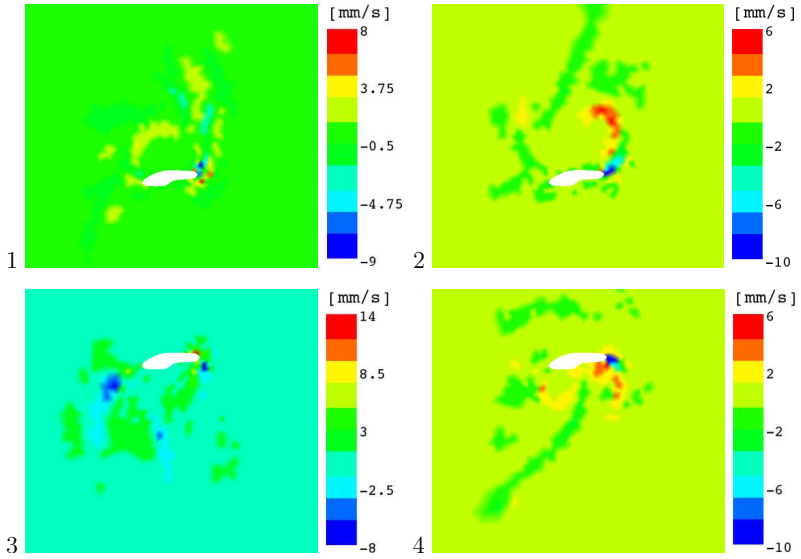

Figure 16: Upwelling velocity at mid-depth for the coarse mesh, using the Mellor and Yamada level 2.5 turbulence closure with advection of turbulence variables. Snapshots (1,2,3 and 4) respectively taken on December 1, 1982 at 1h40 (falling tide, peak ebb velocity), 5h00 (end of falling tide, shortly before tide reversal), 7h55 (rising tide, peak flood velocity) and 10h50 (end of rising tide, shortly before tide reversal).

7 Conclusion

In this work, a Mellor and Yamada level 2.5 (MY25) turbulence closure was implemented in a three-dimensional finite element hydrodynamic marine model. Simulations were performed around Rattray Island, in order to estimate the effect of the turbulence closure on the upwelling velocity in the wake of the island.

The upwelling velocity is significantly altered when using the MY25 closure instead of a simple algebraic closure. This difference is mostly caused by two factors. First, the vertical eddy viscosity is, on average, smaller with MY25. This leads to less mixing and a larger vertical shear in the horizontal velocity at the bottom. As a consequence, this tends to increase upwelling in the centre of the eddies. The second reason is that the MY25 closure takes into account the hysteresis effect on turbulence variables. This hysteresis effect induces a delay in the variation of turbulence variables, which has an influence on the upwelling velocity. This influence can, depending on the situation, increase or decrease the upwelling. The shape of the vertical profiles of eddy viscosity are quite similar with both closures.

The MY25 closure gives sufficient upwelling in the wake of the island to reasonably explain the transport of sediments from the sea bottom to the sea surface. This is not the case with the model using the simple turbulence closure. However, a diagnosis based on the age (White and Deleersnijder, 2006) accounted for the presence of mud at the surface via intense upwelling off the tips of the island. The high turbidity downstream of the island is possibly due to the combination of upwelling in the centre of the eddies and vertical transport near the tips of the island.

A simulation was performed with advection of turbulence variables in order to estimate its effect on smaller scale. In the case of the tidal circulation around a shallow-water island, the effect of advection of turbulence variables is relatively small and can be neglected. This conclusion was confirmed by an analysis of orders of magnitude carried out on the turbulent kinetic energy equation.

The Mellor and Yamada level 2.5 turbulence closure improves the model in its ability to predict upwelling. The sophistication level of MY25 is not mandatory for a non-stratified problem such as Rattray Island, yet it brings to light phenomena that are simply absent when using a simple algebraic closure.

Acknowledgements

Sébastien Blaise is a Research fellow with the Belgian Fund for Research in Industry and Agriculture (FRIA). Laurent White and Eric Deleersnijder are a Research fellow and a Research associate, respectively, with the Belgian National Fund for Scientific Research (FNRS). The present study was carried out within the scope of the project "A second-generation model of the ocean system", which is funded by the *Communauté Francaise de Belgique*, as *Actions de*

Recherche Concertées, under contract ARC 04/09-316. This work is a contribution to the development of SLIM, the Second-generation Louvain-la-Neuve Ice-ocean Model (http://www.climate.be/SLIM). The authors indebted to Eric Wolanski for providing data concerning Rattray Island.

References

Aikman, F., Baptista, A., Blain, C., and Iskandarani, M. 2006. Cross-scale Ocean Modelling Benchmark. WWW Page, *http://www.stccmop.org/node/114*.

Akin, J., Tezduyar, T., Ungor, M., and Mittal, S. 2003. Stabilization parameters and Smagorinsky turbulence model. *Journal of Applied Mechanics*, 70(1):1–9.

Baumert, H. and Radach, G. 1992. Hysteresis of Turbulent Kinetic Energy in Nonrotational Tidal Flows: A Model Study. *Journal of Geophysical Research*, 97:3669–3677.

Black, K. and Gray, S. 1987. Eddy formation in unsteady flows. *Journal of Geophysical Research*, 92(C9):9514–9522.

Blaise, S. and White, L. 2006. Development of a marine modelling benchmark: tidal circulation around Rattray Island. WWW Page, *http://www.climate.be/SLIM/Benchmarks*.

Blumberg, A. and Galperin, B. 2006. Modeling Vertical Structure of Open-Channel Flows. *Journal of Hydraulic Engineering*, 118(8):1119–1134.

Bowker, K. A. 1988. Albert Einstein and meandering rivers. *Earth Science History*, 7(1):45–46.

Burchard, H. 2002. *Applied Turbulence Modelling in Marine Waters, vol. 100 of Lecture Notes in Earth Sciences*. *Springer, Berlin, Heidelberg, New York*.

Cushman-Roisin, B. and Naimie, C. E. 2002. A 3D finite-element model of the Adriatic tides. *Journal of Marine Systems*, 37(4):279–297.

Danilov, S., Kivman, G., and Schröter, J. 2004. A finite element ocean model: principles and evaluation. *Ocean Modelling*, 6:125–150.

Danilov, S., Kivman, G., and Schröter, J. 2005. Evaluation of an eddy-permitting finite-element ocean model in the North Atlantic. *Ocean Modelling*, 10:35–49.

Deleersnijder, E. 1989. Upwelling and upsloping in three-dimensional marine models. *Applied Mathematical Modelling*, 13:462–467.

Deleersnijder, E. 1994. An analysis of the vertical velocity field computed by a three-dimensional model in the region of the Bering Strait. *Tellus A*, 46:149–159.

Deleersnijder, E. and Luyten, P. 1994. On the practical advantages of the quasi-equilibrium version of the Mellor and Yamada level 2.5 turbulence closure applied to marine modelling. *Applied Mathematical Modelling*, 18:281–287.

Deleersnijder, E., Norro, A., and Wolanski, E. 1992. A three-dimensional model of the water circulation around an island in shallow water. *Continental Shelf Research*, 12(7/8):891–906.

Deleersnijder, E., Campin, J.-M., and Delhez, E. J. M. 2001. The concept of age in marine modelling: I. Theory and preliminary results. *Journal of Marine Systems*, 28:229–267.

Delhez, E. J. M., Campin, J.-M., Hirst, A. C., and Deleersnijder, E. 1999. Toward a general theory of the age in ocean modelling. *Ocean Modelling*, 1:17–27.

Ezer, T. 2005. Entrainment, diapycnal mixing and transport in three-dimensional bottom gravity current simulations using the Mellor-Yamada turbulence scheme. *Ocean Modelling*, 9:151–168.

Falconer, R., Wolanski, E., and Mardapitta-Hadjipandeli, L. 1986. Modeling tidal circulation in an island's wake. *Journal of Waterway, Port, Coastal and Ocean Engineering*, 112:234–254.

Fisher, H., List, J., Koh, C., Imberger, J., and Brooks, N. 1979. *Mixing in Inland and Coastal Waters*. *Academic Press, New York*.

Flather, R. 1976. A tidal model of the northwest European continental shelf. *Mémoires de la Société Royale des Sciences de Liège*, 6(10):141–164.

Ford, R., Pain, C. C., Piggott, M. D., Goddard, A. J. H., de Oliveira, C. R. E., and Umpleby, A. P. 2004a. A non-hydrostatic finite element model for three-dimensional stratified oceanic flows. Part I: model formulation. *Monthly Weather Review*, 132:2816–2831.

Ford, R., Pain, C. C., Piggott, M. D., Goddard, A. J. H., de Oliveira, C. R. E., and Umpleby, A. P. 2004b. A non-hydrostatic finite element model for three-dimensional stratified oceanic flows. Part II: model validation. *Monthly Weather Review*, 132:2832–2844.

Fortunato, A. B., Baptista, A. M., and Luettich, R. A. 1997. A three-dimensional model of tidal currents in the mouth of the Tagus estuary. *Continental Shelf Research*, 17(14):1689–1714.

Galperin, B., Kantha, L., Hassid, S., and Rosati, A. 1988. A quasi-equilibrium turbulent energy model for geophysical flows. *Journal of the Atmospheric Sciences*, 45:55–62.

Gorman, G. J., Piggott, M. D., Pain, C. C., de Oliveira, C. R. E., Umpleby, A. P., and Goddard, A. J. H. 2006. Optimisation based bathymetry approximation through constrained unstructured mesh adaptivity. *Ocean Modelling*, 12:436–452.

Hanert, E., Legat, V., and Deleersnijder, E. 2003. A comparison of three finite elements to solve the linear shallow water equations. *Ocean Modelling*, 5:17–35.

Hanert, E., Roux, D. Y. L., Legat, V., and Deleersnijder, E. 2005b. An efficient Eulerian finite element method for the shallow water equations. *Ocean Modelling*, 10:115–136.

Hanert, E., Deleersnijder, E., and Legat, V. 2006. An adaptative finite element water column model using the Mellor-Yamada level 2.5 turbulent closure scheme. *Ocean Modelling*, 12:205–223.

Kinnmark, I. 1986. *The Shallow Water Wave Equations: Formulation, Analysis and Applications*, volume 15 of *Lecture Notes in Engineering*. Springer-Verlag.

Kolar, R. L., Westerink, J. J., Cantekin, M. E., and Blain, C. A. 1994. Aspects of nonlinear simulations using shallow-water models based on the wave continuity equation. *Computers and Fluids*, 23(3):523–538.

Labeur, R. and Pietrzak, J. 2005. A fully three dimensional unstructured grid non-hydrostatic finite element coastal model. *Ocean Modelling*, 10:51–67.

Le Roux, D. Y. 2001. A new triangular finite-element with optimum constraint ratio for compressible fluids. *SIAM Journal on Scientific Computing*, 23(1):66–80.

Le Roux, D. Y. 2005. Dispersion relation analysis of the $P_1^{NC} - P_1$ finite-element pair in shallow-water models. *SIAM Journal on Scientific Computing*, 27(2):394–414.

Le Roux, D. Y., Staniforth, A., and Lin, C. A. 1998. Finite elements for shallow-water equation ocean models. *Monthly Weather Review*, 126:1931–1951.

Legrand, S., Legat, V., and Deleersnijder, E. 2000. Delaunay mesh generation for unstructured-grid ocean general circulation model. *Ocean Modelling*, 2:17–28.

Legrand, S., Deleersnijder, E., Hanert, E., Legat, V., and Wolanski, E. 2006. High-resolution unstructured meshes for hydrodynamic models of the Great Barrier Reef, Australia. *Estuarine, Coastal and Shelf Science*, 68:36–46.

Legrand, S., Deleersnijder, E., Delhez, E., and Legat, V. 2007. Unstructured, anisotropic mesh generation for the Northwestern European continental shelf, the continental slope and the neighboring ocean. *Continental Shelf Research*, 27:1344–1356.

Lynch, D., Ip, J., Naimie, C., and Werner, F. 1996. Comprehensive coastal circulation model with application to the Gulf of Maine. *Continental Shelf Research*, 16:875–906.

Lynch, D. R. and Gray, W. R. 1979. A wave equation model for finite element tidal computations. *Computers and Fluids*, 7:207–228.

Lynch, D. R. and Naimie, C. E. 1993. The M2 tide and its residuals on the outer banks of the Gulf of Maine. *Journal of Physical Oceanography*, 23:2222–2253.

Massey, T. C. and Blain, C. A. 2006. In search of a consistent and conservative mass flux for the GWCE. *Computer Methods in Applied Mechanics and Engineering*, 195:571–587.

Mellor, G. L. and Yamada, T. 1974. A hierarchy of turbulence closure models for planetary boundary layers. *Journal of the Atmospheric Sciences*, 31:1791–1806.

Mellor, G. L. and Yamada, T. 1982. Development of a turbulence closure model for geophysical fluid problems. *Review of Geophysics and Space Physics*, 20:851–875.

Nechaev, D., Schröter, J., and Yaremchuk, M. 2003. A diagnostic stabilized finite-element ocean circulation model. *Ocean Modelling*, 5:37–63.

Pain, C. C., Piggott, M., Goddard, A., Fang, F., Gorman, G., Marshall, D. P., Eaton, M., Power, P., and de Oliveira, C. 2005. Three-dimensional unstructured mesh ocean modelling. *Ocean Modelling*, 10:5–33.

Pietrzak, J., Deleersnijder, E., and Schröter, J. 2005. Special Issue: The Second International Workshop on Unstructured Mesh Numerical Modelling of Coastal, Shelf and Ocean Flows. *Ocean Modelling*, 10:1–252.

Pietrzak, J., Iskandarani, M., Schröter, J., and Lyard, F. 2006. Special Issue: The Third International Workshop on Unstructured Mesh Numerical Modelling of Coastal, Shelf and Ocean Flows. *Ocean Modelling*, 15:1–138.

Ruddick, K., Deleersnijder, E., Mulder, T. D., and Luyten, P. 1994. HA model study of the Rhine discharge front and downwelling circulation. *Tellus Ser. A*, 46:149–159.

Ruddick, K., Deleersnijder, E., Luyten, P., and Ozer, J. 1995. Haline stratification in the Rhine-Meuse freshwater model sensitivity analysis. *Continental Shelf Research*, 15:1597–1630.

Smagorinsky, J. 1963. General circulation experiments with the primitive equations. 1 The basic experiments. *Monthy Weather Review*, 91(5):99–165.

Stacey, M. W. and Pond, S. 1997. On the Mellor-Yamada Turbulence Closure Scheme: The Surface Boundary Condition for q^2. *Journal of Physical Oceanography*, 27:2081–2086.

Timmermann, R. and Losch, M. 2005. Using the Mellor-Yamada mixing scheme in seasonally ice-covered seas-Corrigendum to: Parameterization of vertical mixing in the Weddell Sea. *Ocean Modelling*, 10:369–372.

Walters, R. A. 2006. Design considerations for a finite element coastal ocean model. *Ocean Modelling*, 15:90–100.

Walters, R. A. and Werner, F. E. 1989. A comparison of two finite element models of tidal hydrodynamics using the North Sea data set. *Advances in Water Resources*, 12:184–193.

White, L. and Deleersnijder, E. 2006. Diagnoses of vertical transport in a three-dimensional finite-element model of the tidal circulation around an island. *Estuarine, Coastal and Shelf Science*. (in press).

White, L., Deleersnijder, E., and Legat, V. 2007. A Three-Dimensional Unstructured Mesh Finite Element Marine Model, With Application to the Flow Around a Shallow-Water Island. *Ocean Modelling, in preparation*.

Wolanski, E. and Hamner, W. 1988. Topographically controlled fronts in ocean and their biological influence. *Science*, 241(4862):177–181.

Wolanski, E., Imberger, J., and Heron, M. 1984. Island wakes in Shallow Waters. *Journal of Geophysical Research*, 89(C6):10553–10569.

Wolanski, E., Asaeda, T., Tanaka, A., and Deleersnijder, E. 1996. Three-dimensional island wakes in the field, laboratory experiments and numerical models. *Continental Shelf Research*, 16(11):1437–1452.

4.2 Comments on the publication

The original paper from Mellor and Yamada (1982) suggests to use a Dirichlet boundary condition for the turbulence energy scale q^2 at the sea surface and at the sea bottom:

$$q^2 = B_1^{2/3} u_*^2. \tag{4.11}$$

In the absence of wind, the surface friction velocity $u_* = \sqrt{\tau/\rho}$ vanishes because the surface stress τ is nil. The resulting zero turbulent kinetic energy at the sea surface does not represent a physical behaviour, and a Neumann-type boundary leads to more accurate results (Burchard, 2002a). In order to avoid a zero turbulent kinetic energy at the sea surface, a no-flux boundary condition for q^2 is typically used

$$\frac{\partial q^2}{\partial z} = 0. \tag{4.12}$$

Such a condition may lead to more realistic results and should have been considered in the study. If so, there would have been no need to chose $\delta = 1$ as a parameter in the turbulence closure (7) suggested by Fisher *et al.* (1979).

The Mellor and Yamada (1982) turbulence closure model is quite old, but it is still used in many realistic simulations. Its study is then still of interests because of its availability in popular marine model. However, more recent approaches may provide a better representation of the turbulence.

Conclusions and perspectives

The first objective of this work was to build a three-dimensional unstructured finite-element marine model that uses suitable numerical methods, in order to obtain the most accurate representation of physical phenomena. Based upon the Discontinuous Galerkin method, the model was designed to be stable and introduce few numerical diffusion. Its stabilization relies on interface fluxes only and the treatment of closed and bottom boundaries produces non-oscillating solutions without adding any explicit diffusion.

The model was applied to different baroclinic benchmarks, showing that it was able to reproduce the qualitative behaviour of physical phenomena in typical ocean test cases. These applications are however not sufficient to validate the model quantitatively. Deeper diagnostics need to be performed on various benchmarks, and intercomparisons with other models should be done.

The current structure of the model, still in development, is presented in the first chapter. As it is continuously evolving, the formulation is not definitively set and the present conclusion is probably already out of date; but its main characteristics should not change. Among them, the core features making the model computationnaly efficient and scaling on large parallel clusters will eventually be preserved:

- Unstructured prismatic three-dimensional meshes.
- Discontinuous Galerkin method with explicit treatment of horizontal advection and diffusion to allow independent block systems associated to columns of prisms.
- Implicit/explicit Runge-Kutta time discretization, with an implicit treatment of vertical processes, gravity waves and coriolis
- Mode splitting technique in which two-dimensional and three-dimensional operators are computed only once.

Some components may be subject to modifications or improvements. To compute the fluxes at the interfaces between elements, we rely on Riemann solvers derived from the two-dimensional shallow-water equations (Comblen

et al., 2009b). However, it is not clear if a baroclinic component should be included in the formulation. More sophisticated expressions of the interface fluxes may improve the simulation of baroclinic flows. Another choice to be investigated is the specific treatment of lateral and bottom boundaries. It provides a new alternative to model consistent and conservative closed boundaries without adding diffusion in the momentum equations. However, further studies should confirm that this treatment produces a physically acceptable behaviour. In particular, it should be confirmed that the vertical transport of tracers induced at the lateral closed boundaries is acceptable. This solution should be compared with classical ones such as limiting or increased viscosity.

To evolve into a global ocean model, many improvements need to be developed in the code. In the perspective of the research for a stable and accurate formulation, the code has been made very flexible, sometimes at the expense of efficiency. After that exploratory work, further optimisations are needed to efficiently take advantage of the numerical scheme and allow fast simulations of multiscale realistic cases. For a complete validation, the model must be applied to realistic baroclinic applications, first at the regional scale. An interesting application is the simulation of the flow in the Northwest European Continental Shelf Sea. Unstructured grid abilities can be used by performing a mesh refinement in the vicinity and inside the main estuaries. It is then a good application to evaluate a multiscale model. Two-dimensional and three-dimensional diagnostics can validate that the model predicts the correct water properties: the tidal residual flow, the presence or absence of stratification and the dispersion of freshwater injected by the rivers. Simulations of the global ocean require additional components to be added to the model. Computations on the sphere were made possible through the work of Comblen *et al.* (2008) that is already implemented in the code. The different vertical coordinates systems have to be toroughly validated in order to be able to really conclude that shaved cells are the most appropriate choice. Then, a long period of parameterisation tuning is needed before obtaining global ocean three-dimensional results fitting the main aspects of the global circulation.

When the model will be able to reproduce the global circulation, additional components will have to be considered. Mesh adaptation can be implemented using the MAdLib library, developed at the UCL[1]. It is open source and supports mesh adaptation on the sphere. When making use of mesh adaptation, attention must be paid to the interpolation of variables between meshes that must conserve mass and tracers. High-order computations should be investigated. They fit in the framework of the Discontinuous Galerkin method and seem promising for ocean modelling (Bernard *et al.*, 2005). Technically, high-order elements are already implemented in the code. A major adaptation to work on is the use a high-order description of the boundaries, needed for such methods (Bernard *et al.*, 2008b).

[1]MAdLib: an open source Mesh Adaptation Library (`http://sites.uclouvain.be/madlib`)

Fulfilling the objective of building a finite-element marine model, some issues related to unresolved physics were addressed. A part of this work is dedicated to this topic. Three types of phenomena, unresolved in most of the models, are considered:

- Phenomena related to boundaries, called boundary layers
- Phenomena whose spatial dimension is higher than the model dimension
- Small-scale phenomena, not necessarily related to boundaries, which are smaller than the grid size

Numerical techniques were developed in this work to efficiently capture some unresolved phenomena while ensuring stability.

The extended finite element method is very powerful to represent some boundary layers. Its application to the logarithmic bottom and the residence time boundary layers showed that the latter can be resolved up to a high degree of precision without refinement of the mesh, simply by taking into account the behaviour of an idealised solution in the choice of the shape functions. However, the interest of this method in most geophysical models is limited, as the complete description of subgrid scale phenomena is generally not of interest for the modeller. The advantages of the extended finite element method for boundary layers (i.e. the explicit representation of the boundary layer) may not worth the extra complexity in the implementation of the method. Making use of parameterisations is often much more simple, particularly in two-dimensional and three-dimensional models, and is generally sufficient. This exploratory work opens new perspectives about the use of the extended finite elements method for computational fluid dynamics, but is not necessary to be applied to geophysical flows models.

Consequently, we relied on a parameterisation to capture the boundary layer of the residence time appearing at inflow open boundaries when the Peclet number is high. This parameterisation was developed upon an idealised one-dimensional stationary solution. Its use for the computation of the residence time in the Scheldt Estuary showed that it is applicable to two-dimensional realistic domains. A three-dimensional generalisation should be straightforward. In order to simulate the residence time in the Scheldt Estuary using a two-dimensional finite element model, some work was done to preserve spatial and temporal consistency for finite element backward simulations. Using the techniques developed in this work, it is now relatively easy to perform finite element computations of the residence time using the adjoint method of Delhez *et al.* (2004) which, to the best of our knowledge, was never done in the past. These developments can be of great use for physical studies as they combine the advantages of a full spatial and temporal description of the residence time field with the multiscale abilities of the finite element method.

The parameterisation of the horizontal density gradient in a one-dimensional model was investigated to prevent the model to generate unrealistic under- and over-shoots of density. When the one-dimensional approximation is valid, the use of simple column models is interesting to get a quick overview of the main aspects of the flow. One-dimensional models are however not able to represent some phenomena which are typically two- or three-dimensional and can have a strong influence on marine systems. Three dimensional models may be needed when the behaviour of the system can not be predicted by means of a lower dimension model, or to validate the one-dimensional approximation. Used to limit the stratification in a one-dimensional model, the mathematical method we had recourse to for establishing the properties of the new parameterisation of horizontal salinity gradient may be applied to a wide range of partial differential problems in order to derive a priori upper or lower bounds of their solution.

The last chapter of this work is dedicated to the effect of the turbulence closure scheme on the simulation of the flow in the wake of a shallow-water island. This study clearly shows that the turbulence closure scheme has a significant influence on the simulation of the flow, as the model using the Mellor and Yamada level 2.5 turbulence closure was able to explain physical observations (i.e. the transport of bed sediments to the sea surface) which were not in accordance with previous studies using simpler turbulence closures. This highlights the critical importance of the turbulence closures, and more generally parameterisations in geophysical models. Various configurations usually require different parameterisations and the choice of the latter must be made with care. Furthermore, the use of a multiscale model implies that the parameterisations may differ regarding the location in the computational domain, as the resolution and involved physics are different from an area to another. In a global scale model, several parameterisations are needed, related to the high number of unresolved phenomena from small scale turbulence to mesoscale eddies; and a consequent work must be done to use the appropriate parameterisation where it is required.

In the framework of a three-dimensional finite element baroclinic model, various numerical aspects related to geophysical flows in general were tackled in this thesis. The model developed in this work confirms that the Discontinuous Galerkin method can be efficiently applied to marine modelling. Even though global ocean applications need additional components, the dynamical core of the model is ready for such simulations. This thesis is a contribution to the development of the SLIM[2] model and a step towards Discontinuous Galerkin global multiscale simulations.

[2]Second-generation Louvain-la-Neuve Ice-ocean model (`http://www.climate.be/SLIM`)

Appendix A

Complementary material to Chapter 1

Depth-integrating three-dimensional equations

In section 1.2.1, depth-integration of the momentum equation is performed by summing the lines and columns of the three-dimensional discrete system matrix and vector whose corresponding nodes share the same vertical. This property is demonstrated in this section.

Any term of the hydrodynamic equations can be written, after a short development, in a generic form:

$$\left(1+\alpha\left(\frac{\partial^p u}{\partial a^p}-1\right)\right) f(x,z,u), \tag{A-1}$$

where $\frac{\partial^p u}{\partial a^p}$ represents the $p-th$ derivative of the unknown u regard to a, the latter being either the horizontal or vertical coordinate (i.e. x or z). The linear dependency of the term is expressed by α which is 1 when the term has a linear implicit dependence to u and 0 if it is not the case. The function $f(x,z,u)$ is related to any nonlinear/explicit dependency. As a simplification, u is a scalar and the horizontal direction y was dropped to work only in the $x-z$ plane.

The discrete formulation of this term reads

$$\sum_{e=1}^{N_e}\sum_{j=1}^{N} < \Phi_i \left(1+\alpha\left(\frac{\partial^p \Phi_j}{\partial a^p}u_j-1\right)\right) f(x,z,u) >_{\Omega_e} \quad \text{for } i=1\rightarrow N, \tag{A-2}$$

where N is the total number of nodes. In a finite-element code, the linear system of equations is usually written in a matrix form $A\cdot U = B$, where the unknown degrees of freedom u_j are located in the vector U. The terms with an implicit linear dependency are stored in the matrix A and their contribution

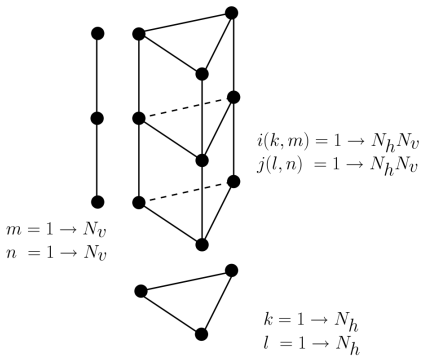

Figure A-1: Indices corresponding to the nodal discrete values. The global indices $i(k,m)$ and $j(k,m)$ are a function of the horizontal position and the vertical position.

at indices (i,j) is:

$$A(i,j) = \alpha \sum_{e=1}^{N_e} < \Phi_i \frac{\partial^p \Phi_j}{\partial a^p} f(x,z,u) >_{\Omega_e} \tag{A-3}$$

The terms without implicit linear dependency are stored in the vector B and their contribution at index (i) is:

$$B(i) = (\alpha - 1) \sum_{e=1}^{N_e} < \Phi_i f(x,z,u) >_{\Omega_e} \tag{A-4}$$

We can express the indices i and j in terms of horizontal indices k and l and vertical indices m and n (Figure A-1), leading to

$$A\big(i(k,m), j(l,n)\big) = \alpha \sum_{e=1}^{N_e} < \Phi_{i(k,m)} \frac{\partial^p \Phi_{j(l,n)}}{\partial a^p} f(x,z,u) >_{\Omega_e} \tag{A-5}$$

and

$$B\big(i(k,m)\big) = (\alpha - 1) \sum_{e=1}^{N_e} < \Phi_{i(k,m)} f(x,z,u) >_{\Omega_e} \tag{A-6}$$

As specified in Section 1.3.2, if the term contains any spatial derivative, it needs to be integrated by parts. The different possibilities will now be treated separately.

1 The term is not integrated by parts

The term can then be simplified, as it does not deal with spatial derivation. If the term has a linear dependency to u, its contribution to the matrix A at

indices (i, j) is:

$$A\big(i(k,m), j(l,n)\big) = \alpha \sum_{e=1}^{N_e} < \Phi_{i(k,m)} \Phi_{j(l,n)} f(x,z,u) >_{\Omega_e} . \qquad \text{(A-7)}$$

The depth-integrated term is obtained by summing the rows and columns which correspond to the same horizontal index (i.e. corresponding to degrees of freedom which are located on the same vertical) in the matrix of the linear system of equations, leading to a new matrix $\overline{A}$.

$$\begin{aligned} \overline{A}(k,l) = \alpha \sum_{e=1}^{N_e} \sum_{m=1}^{N_v} \sum_{n=1}^{N_v} & < \Phi_{i(k,m)} \Phi_{j(l,n)} f(x,z,u) >_{\Omega_e} \\ & = \alpha \sum_{e=1}^{N_e} < \sum_{m=1}^{N_v} \Phi_{i(k,m)} \sum_{n=1}^{N_v} \Phi_{j(l,n)} f(x,z,u) >_{\Omega_e} . \end{aligned} \qquad \text{(A-8)}$$

If we define

$$\begin{aligned} \overline{\Phi}_k &= \textstyle\sum_{m=1}^{N_v} \Phi_{i(k,m)}, \\ \overline{\Phi}_l &= \textstyle\sum_{n=1}^{N_v} \Phi_{l(l,n)}, \end{aligned}$$

which is supposed to be constant over the vertical, the contribution of the term in the matrix $\overline{A}$ reads

$$\begin{aligned} \overline{A}(k,l) = \alpha \sum_{e=1}^{N_e} & < \overline{\Phi}_k \, \overline{\Phi}_l f(x,z,u) >_{\Omega_e} \\ & = \alpha \sum_{c=1}^{N_c} \ll \overline{\Phi}_k \int_V \overline{\Phi}_l f(x,z,u) \, \mathrm{d}z \gg_{\Delta_c}, \end{aligned} \qquad \text{(A-9)}$$

where c is associated with the N_c two-dimensional elements (i.e . triangles) corresponding to a stacked column of three-dimensional elements. If the term has no implicit linear dependence, the same operations can be done by summing the rows of the vector B over the index m to obtain the contribution

$$\overline{B}(k) = (\alpha - 1) \sum_{c=1}^{N_c} \ll \overline{\Phi}_k \int_V f(x,z,u) \, \mathrm{d}z \gg_{\Delta_c} . \qquad \text{(A-10)}$$

By using the reverse development than the one leading from (A-1) to (A-4), we obtain the generic continuous term

$$\int_V \left(1 + \alpha \left(\overline{u} - 1\right)\right) f(x,z,u) \, \mathrm{d}z, \qquad \text{(A-11)}$$

where $\overline{u} \simeq \overline{u}^h = \sum_l \overline{\Phi}_l \overline{U}_l$. For a term without spatial derivatives, (A-11) correspond to the depth-integrated version of (A-1).

2 The term is integrated by part

We first consider that the integration by part is related to a spatial derivation of the linear implicit term. Then, the contribution of the term in the matrix A at indices (i, j) is

$$A\big(i(k,m), j(l,n)\big) = \alpha \sum_{e=1}^{N_e} \Bigg[- < \frac{\partial \Phi_{i(k,m)} f(x,z,u)}{\partial a} \frac{\partial^{(p-1)} \Phi_{j(l,n)}}{\partial a^{(p-1)}} >_{\Omega_e} + \ll \Phi_{i(k,m)} \frac{\partial^{(p-1)} \Phi_{j(l,n)}}{\partial a^{(p-1)}} f^*(x,z,u) n_a \gg_{\partial\Omega_e} \Bigg], \quad \text{(A-12)}$$

where $f^*(x, z, u)$ is a uniquely defined value at the interface between two elements. It is still possible to sum the rows and columns of A over the indices m and n to obtain

$$\overline{A}\big(k,l\big) = \alpha \sum_{e=1}^{N_e} \Bigg[- < \frac{\partial \overline{\Phi}_k f(x,z,u)}{\partial a} \frac{\partial^{(p-1)} \overline{\Phi}_l}{\partial a^{(p-1)}} >_{\Omega_e} + \ll \overline{\Phi}_k \frac{\partial^{(p-1)} \overline{\Phi}_l}{\partial a^{(p-1)}} f^*(x,z,u) n_a \gg_{\partial\Omega_e} \Bigg]. \quad \text{(A-13)}$$

Some integrals may vanish depending if the spatial derivation operator is horizontal or vertical. By reverting the integral by part, the contribution of the term reads

$$\overline{A}\big(k,l\big) = \alpha \sum_{e=1}^{N_e} < \overline{\Phi}_k \frac{\partial^p \overline{\Phi}_l}{\partial a^p} f(x,z,u) >_{\Omega_e} = \alpha \sum_{c=1}^{N_c} \ll \overline{\Phi}_k \int_V \frac{\partial^p \overline{\Phi}_l}{\partial a^p} f(x,z,u)\, \mathrm{d}z \gg_{\Delta_c} . \quad \text{(A-14)}$$

Relation (A-14) can be obtained by the same method if the integration by part is related to a spatial derivation of the nonlinear/explicit term $f(x, z, u)$. If there is no linear implicit dependency, the contribution to the right hand side vector at index (k) will be

$$\overline{B}(k) = (\alpha - 1) \sum_{c=1}^{N_c} \ll \overline{\Phi}_k \int_V f(x,z,u)\, \mathrm{d}z \gg_{\Delta_c} . \quad \text{(A-15)}$$

We can then come back to the generic continuous term

$$\int_V \left(1 + \alpha \left(\frac{\partial^p \overline{u}}{\partial a^p} - 1\right)\right) f(x,z,u)\, \mathrm{d}z, \quad \text{(A-16)}$$

which is the depth-integrated version of (A-1).

References

Adcroft, A., Hill, C., and Marshall, J. 1997. Representation of Topography by Shaved Cells in a Height Coordinate Ocean Model. Monthly Weather Review, 95:2293–2315.

Aizinger, V. and Dawson, C. 2002. A discontinuous Galerkin method for two-dimensional flow and transport in shallow water. Advances in Water Resources, 25:67–84.

Aizinger, V. and Dawson, C. 2007. The local discontinuous Galerkin method for three-dimensional shallow water flow. Computer Methods in Applied Mechanics and Engineering, 196:734–746.

Akin, J. E., Tezduyar, T., and Ungor, M. 2003. Stabilization Parameters and Smagorinsky turbulence model. Transactions of ASME, 70:2–9.

Arnold, D. N., Brezzi, F., Cockburn, B., and Marini, L. D. 2002a. Unified analysis of discontinuous Galerkin methods for elliptic problems. SIAM journal on numerical analysis, 39:1749–1779.

Ascher, U. M., Ruuth, S. J., and Spiteri, R. J. 1997. Implicit-explicit Runge-Kutta methods for time-dependent partial differential equations. Applied Numerical Mathematics, 25:151–167.

Asmus, R., Asmus, H., and van Duren, L. 2007. Introduction: Hydrodynamic control of aquatic ecosystem processes - How does water movement affect different levels of organisation? Estuarine, Coastal and Shelf Science, 75(3):279 – 280.

Avlesen, H., Berntsen, J., and Espelid, T. O. 2001. A convergence study of two ocean mode applied to a density driven flow. International Journal For Numerical Methods In Fluids, 36:639–657.

Bernard, P., Chevaugeon, N., Legat, V., Deleersnijder, E., and Remacle, J. 2005. High-order h-adaptive discontinuous Galerkin methods for ocean modeling. In Diez, P. and Wiberg, N.-E., editors, *Proc. of ADMOS 2005, International Conference on Adaptive Modeling and Simulation, Barcelona, Spain*. CIMNE.

Bernard, P.-E., Remacle, J.-F., and Legat, V. 2008b. Boundary discretization for high order discontinuous Galerkin computations of tidal flows around shallow water islands. International Journal for Numerical Methods in Fluids.

Black, K. P. and Gay, S. L. 1987. Eddy Formation in Unsteady Flows. Journal of Geophysical Research, 92(C9):9514–9522.

Blaise, S. and Deleersnijder, E. 2008. Improving the parameterisation of horizontal density gradient in one-dimensional water column models for estuarine circulation. Ocean Science, 4:239–246.

Blaise, S., Deleersnijder, E., White, L., and Remacle, J.-F. 2007. Influence of the turbulence closure scheme on the finite-element simulation of the upwelling in the wake of a shallow-water island. Continental Shelf Research, 27:2329–2345.

Blaise, S., Comblen, R., Lambrechts, J., Legat, V., Remacle, J.-F., and Deleersnijder, E. 2009a. A discontinuous finite element baroclinic model for marine modeling. Part I: model description. *In preparation*.

Blaise, S., de Brye, B., de Brauwere, A., Deleersnijder, E., Delhez, E. J., and Comblen, R. 2009b. Capturing the residence time boundary layer - Application to the Scheldt Estuary. Ocean Dynamics, *submitted*.

Blumberg, A. F. and Mellor, G. L. 1987. A description of three-dimensional coastal ocean circulation model. In Heaps, N. S., editor, *Three Dimensional Coastal Ocean Model*, pages 1–16. American Geophysical Union.

Burchard, H. 2002a. *Applied Turbulence Modelling in Marine Waters*. Number 100 in Lecture Notes in Earth Science. Springer.

Burchard, H. and Rennau, H. 2008. Comparative quantification of physically and numerically induced mixing in ocean models. Ocean Modelling, 20:293–311.

Camargo, J. A. and lvaro Alonso. 2006. Ecological and toxicological effects of inorganic nitrogen pollution in aquatic ecosystems: A global assessment. Environment International, 32(6):831 – 849.

Casulli, V. and Walters, R.A. 2000. An unstructured grid, three-dimensional model based on the shallow water equations. International Journal for Numerical Methods in Fluids, 32:331–348.

Chee, Y. E. 2004. An ecological perspective on the valuation of ecosystem services. Biological Conservation, 120(4):549 – 565.

Chen, C., Liu, H., and Beardsley, R. C. 2003a. An Unstructured Grid, Finite-Volume, Three-Dimensional, Primitive Equations Ocean Model: Applications to Coastal Ocean and Estuaries. Journal of Atmospheric and Oceanic Technology, 20:159–186.

Cockburn, B. and Shu, C. 1998a. The local discontinuous Galerkin finite element method for convection-diffusion systems. SIAM Journal on Numerical Analysis, 35:2440–2463.

Cockburn, B. and Shu, C.-W. 1998b. The Runge-Kutta Discontinuous Galerkin Method for Conservation Laws V - Multidimensional Systems. Journal of Computational Physics, 141:191–224.

Comblen, R., Legrand, S., Deleersnijder, E., and Legat, V. 2008. A finite element method for solving the shallow water equations on the sphere. Ocean Modelling.

Comblen, R., Blaise, S., Lambrechts, J., Legat, V., Remacle, J.-F., and Deleersnijder, E. 2009a. A discontinuous finite element baroclinic model for marine modeling. Part II: model validation. *In preparation*.

Comblen, R., Lambrechts, J., Remacle, J.-F., and Legat, V. 2009b. Practical evaluation of five part-discontinuous finite element pairs for the non-conservative shallow water equations. International Journal for Numerical Methods in Fluids (in press).

Cotter, C. J., Ham, D. A., and Pain, C. C. 2009. A mixed discontinuous/continuous finite element pair for shallow-water ocean modelling. Ocean Modelling, 26(1-2):86 – 90.

Cushman-Roisin, B. 1994. *Introduction to Geophysical Fluid Dynamics*. Prentice Hall.

Davies, P. A., Dkin, J. M., and Falconer, R. A. 1995b. Eddy Formation Behind a Coastal Headland. Journal of Coastal Research, 11:154–167.

Dawson, C. and Aizinger, V. 2005. A Discontinuous Galerkin Method for Three-Dimensional Shallow Water Equations. Journal of Scientific Computing, 22-23:245–267.

Debreu, L. and Blayo, E. 2008. Two-way embedding algorithms: a review. Ocean Dynamics, 58:415–428.

Deleersnijder, E. and Luyten, P. 1994. On the practical advantages of the quasi-equilibrium version of the Mellor and Yamada level 2.5 turbulence closure applied to marine modelling. Applied Mathematical Modelling, 18:281–287.

Deleersnijder, E., Norro, A., and Wolanski, E. 1992. A three-dimensional model of the water circulation around an island in shallow water. Continental Shelf Research, 12:891–906.

Delhez, E. J. M., Heemink, A. W., and Deleersnijder, E. 2004. Residence time in a semi-enclosed domain from the solution of an adjoint problem. Estuarine, Coastal and Shelf Science, 61:691–702.

Dickey, T. D. 2003. Emerging ocean observations for interdisciplinary data assimilation systems. Journal of Marine Systems, 40-41:5 – 48. The Use of Data Assimilation in Coupled Hydrodynamic, Ecological and Bio-geochemical Models of the Ocean. Selected papers from the 33rd International Liege Colloquium on Ocean Dynamics, held in Liege, Belgium on May 7-11th, 2001.

Dukowicz, J. K. and Smith, R. D. 1994. Implicit free-surface method for the Bryan-Cox-Semtner ocean model. Journal of Geophysical Research, 99:7991–8014.

Dupont, F., Straub, D. N., and Lin, C. A. 2003. Influence of a step-like coastline on the basin scale vorticity budget of mid-latitude gyre models. Tellus A, 55:255–272.

Egbert, G. D., Benett, A. F., and Foreman, M. G. G. 1994. TOPEX/POSEIDON tides estimated using a global inverse model. Journal of Geophysical Research, 99:24,821–24,852.

Ellis, J. B. 2000. Risk assessment approaches for ecosystem responses to transient pollution events in urban receiving waters. Chemosphere, 41(1-2):85 – 91.

Ezer, T. 2005. Entrainment, diapycnal mixing and transport in three-dimensional bottom gravity current simulations using the Mellor-Yamada turbulence closure. Ocean Modelling, 9:151–168.

Ezer, T. 2006. Topographic influence on overflow dynamics: Idealized numerical simulations of the Faroe Bank Channel overflow. Journal of Geophysical Research, 111.

Ezer, T. and Mellor, G. L. 2004. A generalized coordinate ocean model and a comparison of the bottom boundary layer dynamics in terrain-following and in z-level grids. Ocean Modelling, 6:379–403.

Fisher, H., List, J., Koh, C., Imberger, J., and Brooks, N. 1979. *Mixing in Inland and Coastal Waters*. *Academic Press, New York*.

Fletcher, C. 1988. *Computational Techniques for Fluid Dynamics, Vol. I: Fundamental and General Techniques*. Springer Series in Computational Physics. Springer-Verlag.

Fringer, O. B., Gerritsen, M., and Street, R. L. 2006. An unstructured-grid, finite-volume, nonhydrostatic, parallel coastal ocean simulator. Ocean Modelling, 14:139–173.

Gadd, A. J. 1978. A split-explicit integration scheme for numerical weather prediction. Quarterly Journal of the Royal Meteorological Society, 104:569–582.

Galperin, B., Kantha, L.H., Hassid, S., and Rosati, S. 1988. A quasi-equilibrium turbulent energy model for geophysical flows. Journal of Atmospheric Sciences, 45:55–62.

Giraldo, F. X., Perot, J. B., and Fischer, P. F. 2003. A spectral element semi-Lagrangian (SESL) method for the spherical shallow water equations. Journal of Computational Physics, 190:623–650.

Gong, W., Shen, J., and Jia, J. 2008. The impact of human activities on the flushing properties of a semi-enclosed lagoon: Xiaohai, Hainan, China. Marine Environmental Research, 65(1):62 – 76.

Goosse, H., Deleersnijder, E., Fichefet, T., and England, M.H. 1999. Sensitivity of a global coupled ocean-sea ice model to the parametrisation of vertical mixing. Journal of Geophysical Research, 104:13681–13695.

Griffies, S. 2004. *Fundamentals of ocean climate models*. Princeton University Press.

Griffiths, R. W. and Linden, P. F. 1981. The stability of vortices in a rotating, stratified fluid. Journal of Fluid Mechanics, 105:283–316. Version papier chez Richard.

Ham, D. A., Pietrzak, J., and Stelling, G. S. 2005. A scalable unstructured grid 3-dimensional finite volume mode for the shallow water equations. Ocean Modelling, 10:153–169.

Hanert, E., Roux, D. Y. L., Legat, V., and Deleersnijder, E. 2005. An efficient Eulerian finite element method for the shallow water equations. Ocean Modelling, 10:115–136.

Hanert, E., Deleersnijder, E., Blaise, S., and Remacle, J.-F. 2007. Capturing the bottom boundary layer in finite element ocean models. Ocean Modelling, 17:153–162.

Haney, R. L. 1991. On the Pressure Gradient Force over Steep Topography in Sigma Coordinate Ocean Models. Journal of Physical Oceanography, 21:610–619.

Harig, S. 2004. *Aspects of Ocean Circulation with Finite Element Modelling*. Ph.D. thesis, Universität Bremen.

Huang, W. and Spaulding, M. 1996. Modeling Horizontal Diffusion with Sigma Coordinate System. Journal of Hydraulic Engineering, 122(6):349–352.

Hughes, S. A. 1993. *Physical models and laboratory techniques in coastal engineering*, volume 7. *Advanced Series on Ocean Engineering*.

Iskandarani, M., Haidvogel, D.B., and Boyd, J.B. 1995. A staggered spectral element model with application to the oceanic shallow water equations. International Journal for Numerical Methods in Fluids, 20:393–414.

James, I. D. 1996. Advection schemes for shelf sea models. Journal of Marine Systems, 8:237–254.

Jiang, L. and Garwood, R. 1996. Three-Dimensional Simulations of Overflows on Continental Slopes. Journal of Physical Oceanography, 26:1214–1233.

Kim, T., Choi, B., and Lee, S. 2006. Hydrodynamics and sedimentation induced by large-scale coastal developments in the Keum River Estuary, Korea. Estuarine, Coastal and Shelf Science, 68(3-4):515 – 528.

Kubatko, E. J., Westerink, J. J., and Dawson, C. 2006. *hp* Discontinuous Galerkin methods for advection dominated problems in shallow water flows. Computational Methods in Applied Mechanics and Engineering, 196:437–451.

Kuzmin, D., Shashkiw, M., and Svyatskiy, D. 2009. A constrained finite element method satisfying the discrete maximum principle for anisotropic diffusion problems. Journal of Computational Physics, 228:3448–3463.

Lambrechts, J., Comblen, R., Legat, V., Geuzaine, C., and Remacle, J.-F. 2008a. Multiscale mesh generation on the sphere. Ocean Dynamics, 58(5):461–473.

Lambrechts, J., Hanert, E., Deleersnijder, E., Bernard, P.-E., Legat, V., Remacle, J.-F., and Wolanski, E. 2008b. A multiscale model of the whole Great Barrier Reef Hydrodynamics. Estuarine, Coastal and Shelf Science, 79:143–151.

Ledwell, J. R., Watson, A. J., and Law, C. S. 1993. Evidence for slow mixing across the pycnocline from an open-ocean tracer-release experiment. Nature, 364:701–103.

Legg, S., Hallberg, R. W., and Girton, J. B. 2006. Comparison of entrainment in overflows simulated by z-coordinate, isopycnal and non-hydrostatic models. Ocean Modelling, 11:69–97.

LeVeque, R. J. 2002. *Finite Volume Methods for Hyperbolic Problems*. Cambridge Texts in Applied Mathematics. Cambridge University Press.

Lewsey, C., Cid, G., and Kruse, E. 2004. Assessing climate change impacts on coastal infrastructure in the Eastern Caribbean. Marine Policy, 28(5):393 – 409.

Li, X., Chao, Y., McWilliams, J. C., and Fu, L.-L. 2001. A Comparison of Two Vertical Mixing Schemes in a Pacific Ocean General Circulation Model. 14(7):1377–1398.

Liria, P., Garel, E., and Uriarte, A. 2009. The effects of dredging operations on the hydrodynamics of an ebb tidal delta: Oka Estuary, northern Spain. Continental Shelf Research, In Press, Corrected Proof.

lun Yang, S., ying Zhao, Q., and Belkin, I. M. 2002. Temporal variation in the sediment load of the Yangtze river and the influences of human activities. Journal of Hydrology, 263(1-4):56 – 71.

Lynch, D.R., Ip, J.T.C., Naimie, C.E., and Werner, F.E. 1996. Comprehensive coastal circulation model with application to the Gulf of Maine. Continental Shelf Research, 16:875–906.

Marshall, J.C., Adcroft, A.J., Hill, C.N., Perelman, L., and Heisey, C. 1997. A finite-volume, incompressible Navier Stokes model for studies of the ocean on parallel computers. Journal of Geophysical Research, 102:5753–5766.

Mellor, G. L. and Blumberg, A. F. 1985. Modeling Vertical and Horizontal Diffusivities with the Sigma Coordinate System. Monthly Weather Review, 8:1379–1383.

Mellor, G.L. and Yamada, T. 1974. A hierarchy of turbulence closure models for planetary boundary layers. Journal of the Atmospheric Sciences, 31:1791–1806.

Mellor, G.L. and Yamada, T. 1982. Development of a turbulence closure model for geophysical fluids problems. Review of Geophysics and Space Physics, 20:851–875.

Miglio, E., Quarteroni, A., and Saleri, F. 1999. Finite Element Approximation of Quasi-3D Shallow Water Equations. Computer Methods in Applied Mechanics and Engineering, 174:355–369.

Munday, P., Leis, J., Lough, J., Paris, C., Kingsford, M., Berumen, M., and Lambrechts, J. 2009. Climate change and coral reef connectivity. Coral Reefs, 28:379–395.

Oliger, J. and Sundstrm, A. 1978. Theoretical and Practical Aspects of Some Initial Boundary Value Problems in Fluid Dynamics. SIAM Journal on Applied Mathematics, 35(3):419–446.

Pacanowski, R. C. and Philander, S. G. H. 1981a. Parametrization of Vertical Mixing in Numerical Models of Tropical Oceans. Journal of Physical Oceanography, 11:1443–1451.

Piggott, M. D., Gorman, G. J., Pain, C. C., Allison, P. A., Candy, A. S., Martin, B. T., and Wells, M. R. 2008. A new computational framework for multi-scale ocean modelling basid on adapting unstructured meshes. International Journal For Numerical Methods In Fluids, 56:1003–1015.

Rajaram, T. and Das, A. 2008. Water pollution by industrial effluents in India: Discharge scenarios and case for participatory ecosystem specific local regulation. Futures, 40(1):56 – 69.

Riisgård, H., Lassen, J., Kortegaard, M., Møller, L., Friedrichs, M., Jensen, M., and Larsen, P. 2007. Interplay between filter-feeding zoobenthos and hydrodynamics in the shallow Odense Fjord (Denmark) - Earlier and recent studies, perspectives and modelling. Estuarine, Coastal and Shelf Science, 75(3):281 – 295.

Riviere, B. 2008. *Discontinuous Galerkin Methods for Solving Elliptic and Parabolic Equations: Theory and Implementation*, volume 35 of *Frontiers in Mathematics*. SIAM.

Rousseau, A. 2005. *Etudes théoriques et numériques des équations primitives de l'océan sans viscosité*. Ph.D. thesis, Université de Paris XI Orsay.

Rousseau, A., Temam, R., and Tribbia, J. 2004. Boundary Layers in an Ocean Related System. Journal of Scientific Computing, 21:405–432.

Sahni, O., Jansen, K. E., Shephard, M. S., Taylor, C. A., and Beall, M. W. 2008. Adaptive boundary layer meshing for viscous flow simulations. Engineering with Computers, 24(3):267–285.

Shahbazi, K. 2005. An explicit expression for the penalty parameter of the interior penalty method. Journal of Computational Physics, 205:401–407.

Slingo, J., Bates, K., Nikiforakis, N., Piggott, M., Roberts, M., Shaffrey, L., Stevens, I., Vidale, P. L., and Weller, H. 2009. Developing the next-generation climate system models: challenges and achievements. Philosophical Transactions of the Royal Society A: Mathematical, Physical and Engineering Sciences, 367(1890):815–831.

Smagorinsky, J. 1963a. General Circulation Experiments with the Primitive Equations. Monthly Weather Review, 91:99–164.

Stuhne, G. R. and Peltier, W. R. 2006. A robust unstructured grid discretization for 3-dimensional hydrostatic flows in spherical geometry: A new numerical structure for ocean general circulation modeling. Journal of Computational Physics, 213:704–729.

Tartinville, B., Deleersnijder, E., Lazure, P., Proctor, R., Ruddick, K. G., and Uittenbogaard, R. E. 1998. A coastal ocean mode intercomparison study for a three-dimensional idealised test case. Applied Mathematical Modelling, 22:165–182.

Timmermann, R., Danilov, S., Schrter, J., Bning, C., Sidorenko, D., and Rollenhagen, K. 2009. Ocean circulation and sea ice distribution in a finite element global sea ice-ocean model. Ocean Modelling, 27(3-4):114 – 129.

Toro, E. 1997. *Riemann Solvers and Numerical Methods for Fluid Dynamics, a Practical Introduction*. Springer, Berlin.

Tseng, Y.-H. and Dietrich, D. E. 2006. Entrainment and transport in idealized three-dimensional gravity current simulation. Journal Of Atmospheric and Oceanic Technology, 23:1249–1269.

Tuncer, G., Karakas, T., Balkas, T. I., Gkay, C. F., Aygnn, S., Yurteri, C., and Tuncel, G. 1998. Land-based sources of pollution along the black sea coast of Turkey: Concentrations and annual loads to the black sea. Marine Pollution Bulletin, 36(6):409 – 423.

Walters, R.A. and Casulli, V. 1998. A Robust, Finite Element Model for Hydrostatic Surface Water Flows. Communications in Numerical Methods in Engineering, 14:931–940.

Wang, Q. 2007. *The Finite Element Ocean Model and its aspect of vertical discretization*. Ph.D. thesis, Bremen University.

Wang, Q., Danilov, S., and Schröter, J. 2008a. Comparison of overflow simulations on different vertical grids using the Finite Element Ocean circulation Model. Ocean Modelling, 20:313–335.

Wang, Q., Danilov, S., and Schröter, J. 2008b. Finite element ocean circulation model based on triangular prismatic elements, with application in studying the effect of topography representation. Journal of Geophysical Research, 113.

White, L. and Deleersnijder, E. 2007. Diagnoses of vertical transport in a three-dimensional finite element model of the tidal circulation around an island. Estuarine Coastal and Shelf Science, 74:735–749.

White, L., Deleersnijder, E., and Legat, V. 2008a. A three-dimensional unstructured mesh finite element shallow-water model, with application to the flows around an island and in a wind-driven elongated basin. Ocean Modelling, in press.

White, L., Legat, V., and Deleersnijder, E. 2008b. Tracer Conservation for Three-Dimensional, Finite-Element, Free-Surface, Ocean Modeling on Moving Prismatic Meshes. Monthly Weather Review, 136:420–442.

Williams, D. M. B., Wolanski, E., and Andrews, J. C. 1984. Transport Mechanisms and the Potential Movement of Planktonic Larvae in the Central Region of the Great Barrier Reef. Coral Reefs, 3:229 – 236.

Wolanski, E. 1994. *Physical Oceanographic Processes of the Great Barrier Reef*. Boca Raton, FL: CRC Press.

Wolanski, E., Asaeda, T., Tanaka, T., and Deleersnijder, E. 1996. Three-dimensional island wakes in the field, laboratory and numerical codes. Continental Shelf Research, 16:1437–1452.

Université catholique de Louvain
École polytechnique de Louvain
Département de mécanique
Unité de mécanique appliquée

Bâtiment Euler
Avenue Georges Lemaître 4, 1348 Louvain-la-Neuve, Belgique
Tél. : + 32 (0) 10 47 23 60 – fax : + 32 (0) 10 47 21 80
E mail : seb.belese@laposte.net
http://www.climate.be/SLIM

Numerical models are very helpful to understand the behaviour of the marine system. Ocean models have been developed for more than forty years, and their design is an area of active research. If the representation of the physics has been highly improved, the fundamental numerical technique has not evolved: they still use the finite difference method on structured grids. Recent efforts focus on developing the new generation of ocean models, taking advantage of the potential of modern numerical methods. Based on unstructured grids, such models allow to faithfully represent complex topographic features such as the coastlines, narrow straits and islands. The mesh resolution can be refined locally in regions of interest or where the dynamics is more demanding.

This PhD dissertation focuses on the development of a three-dimensional baroclinic marine model using the Discontinuous Galerkin finite element method. The model is described, with some results of baroclinic simulations. The rest of the thesis is devoted to different types of unresolved physics. Two different boundary layers are introduced: the bottom velocity boundary layer and the boundary layer of the residence time. Both parameterisation and representation using the extended finite element method are discussed. A chapter is dedicated to the treatment of the horizontal density gradient in baroclinic column models. Attention is paid to the stability of the method under different configurations. Then, the turbulence modelling in three-dimensional models is studied by comparing the effect of different turbulence closure models on a simulation of the flow around a shallow-water island.

Sébastien Blaise was born on August 21, 1982 in Messancy, Belgium. In 2000, he joined the Université catholique de Louvain in Louvain-la-Neuve, where he completed a Master Degree in Civil Engineering in 2005. He started a Ph.D. at the same university with focus on finite element marine modelling, that he completed in 2009.